Studies on pulsed laser deposited Mo, W and Rh thin films for First Mirror application

by

ABU TALAT TAHIR MOSTAKO

DEPARTMENT OF PHYSICS

INDIAN INSTITUTE OF TECHNOLOGY GUWAHATI

GUWAHATI-781039, INDIA

AUGUST 2013

Studies on pulsed laser deposited Mo, W and Rh thin films for First Mirror application

A Thesis submitted in partial fulfillment of the requirements for the award of the degree of

DOCTOR OF PHILOSOPHY

by

ABU TALAT TAHIR MOSTAKO

DEPARTMENT OF PHYSICS

INDIAN INSTITUTE OF TECHNOLOGY GUWAHATI

GUWAHATI-781039, INDIA

AUGUST 2013

Dedicated to my Parents

Abu Talat Tahir Mostako
Roll No. 08612105
Department of Physics
Indian Institute of Technology Guwahati
Guwahati-781039, Assam, India

STATEMENT

I hereby declare that the matter embodied in this thesis is the result of investigations carried out by me at the Department of Physics, Indian Institute of Technology Guwahati, Guwahati, India, under the supervision of **Prof. Alika Khare**. This thesis has not been submitted to any university/institute or elsewhere for the award of any degree, diploma or associateship.

Date: August, 2013 **Abu Talat Tahir Mostako**

भारतीय प्रौद्योगिकी संस्थान गुवाहाटी
Indian Institute of Technology Guwahati
Department of Physics
Guwahati-781039, Assam State, INDIA
Phone: +91 361 2582705, 2690321 to 328 (extn. 2705),
Fax: +91 361 2582749
Dr. Alika Khare
Professor
E-mail: alika@iitg.ernet.in, k_alika@yahoo.com

Date: August, 2013

Certificate

This is to certify that work contained in the thesis entitled '**Studies on pulsed laser deposited Mo, W and Rh thin films for First Mirror application**', by **Mr Abu Talat Tahir Mostako** (Roll no. 08612105), a student of Department of Physics, Indian Institute of Technology Guwahati, for the award of degree of Doctor of Philosophy, has been carried out under my supervision and that the same has not been submitted elsewhere for a degree.

(Alika Khare)

ACKNOWLEDGEMENT

First of all, I would like to express my sincere appreciation to my thesis supervisor, Prof. Alika Khare for her constant inspiration, precious advice, guidance and supervision of the research. I appreciate all her contributions of time, ideas and funding to make my Ph.D. experience productive and stimulating. The joy and enthusiasm she has for her research was contagious and motivational for me, even during tough times in the Ph.D. pursuit. I feel tremendously lucky to be her Ph.D. student.

I am also grateful to my doctoral committee members, Dr. Malay Kumar Nandy, Prof. Mohammad Jawed and Dr. Ashwini Kumar Sharma for their valuable suggestions and motivation which helped me to improve the research work. I owe my sincere thanks to the present and former Head of Department of Physics as well as CIF, IIT Guwahati. Dr. C. V. S. Rao, IPR, Gandhinagar (Gujarat) is also acknowledged for providing me the ion beam irradiation facility. In particular, I would like to extend my sincere thanks to Mr C. Borgohain, Mr K. K. Senapati, Mr M. Borah, Dr. S. Sarma, Mr A. C. Deka, Dr. B. K. Sarma and Mr Aditya for their kind help with various instruments.

I would like to thank BRFST, NFP (India), Projects No. NFP/DIAG/A10/01, NFP/DIAG/01 and IIT Guwahati for providing financial assistance during my Ph.D. tenure.

It was pleasure to work with my research lab members Dr. Archana, Dr. Gaurav, Dr. Arpita, Mrs Satchi, Indrajeet, Poulami, Partha, Shanta, Gyan, Prahlad and Rahul. Thanks to them for their suggestions, time, constant help in experiments and kindness throughout my Ph.D.

I am deeply indebted to all my friends Hanif, Anil, Arijit, Tausif, Siraj, Faizi, Romen, Malakar, Sangkha, Abhijeet, my Ph.D. batch mates and juniors for providing a welcome diversion from the critical situations during my Ph.D., whenever I needed. I must acknowledge all my friends for their love, encouragement and support.

Last, but by no means least, my special thanks and appreciation goes to my parents as well as my family members for their unconditional love, blessings, patience, support and understanding throughout my studies and most of all to the Almighty God who made everything possible.

Date: August, 2013 **Abu Talat Tahir Mostako**

ABSTRACT

The focus of the present research work was to develop mirror-like thin films of Mo, W and Rh by pulsed laser deposition (PLD) technique, for First Mirror (FM) application in fusion reactor.

Thin films of Mo, W and Rh were deposited on polished stainless steel (SS) substrate by PLD technique. The optimum deposition parameters obtained from the present study for mirror-like Mo, W and Rh thin films were 500 °C substrate temperature, ~ 2 J/cm^2 laser fluence, ~ 3 cm target-substrate distance and ~ 1.0 mbar Helium ambient gas pressure. The W thin films of thickness ~ 326 nm showed ~ 2 % reduction in FIR specular reflectivity after irradiation of 8 keV H ion beam. In case of 10-30 keV D ion beam irradiation, the specular reflectivity was reduced by ~ 1-9 % and ~ 28-38 % in FIR and UV-visible range, respectively. The Rh thin films of thickness ~ 246 nm, showed ~ 1-7 % and 5-32 % reduction in FIR and UV-visible specular reflectivity after irradiation of 10-30 keV D ions beam. The post exposure degradation in reflectivity of W and Rh mirror-like thin films was explained in terms of damage parameters calculated numerically by using Transport of Ions in Matter (TRIM) Monte Carlo simulation code.

The quality and sustainability of single element W and Rh thin film FMs, in the long term exposure of fusion plasma can be enhanced by making multilayer thin film of more than one element. Based on the damage parameters of D ions and the properties of Rh, W, Cu and SS, a three layer composite thin film, Rh/W/Cu on SS, was designed and fabricated for FM application. The performance of the Rh/W/Cu multilayer thin film FM was tested by exposing to 20 and 30 keV D ion beam of particle flux ~ 1.2×10^{14} ions/cm^2/s. The multilayer Rh/W/Cu thin film showed ~ 1-4 % and ~ 3-20 % reduction in FIR and UV-visible specualr reflectivity, respectively.

In order to collect large amount of plasma radiation for better reliability of spectroscopic signals, the size of Rh and Rh/W/Cu PLD thin film FMs were increased to 50 mm diameter by modifying conventional PLD technique with substrate rastering stage. The uniformity of deposition was confirmed by distinct, straight and parallel interference fringes from Rh single layer and Rh/W/Cu multilayer thin films.

CONTENTS

LIST OF FIGURES

LIST OF TABLES

ABBREVIATIONS

AFM	Atomic Force Microscope	ITER	International Thermonuclear Experimental Reactor
Ar	Argon	kV	kilo volt
Arb. U.	Arbitrary Unit	keV	kilo electron volt
BNC	Bayonet Neill Concelman	LIBS	Laser Induced Breakdown Spectroscopy
BPM	Beam Profile Monitor	LIP	Laser Induced Plasma
CCD	Charge Coupled Device	LTE	Local Thermodynamic Equilibrium
cps	cycle per second	MBE	Molecular Beam Expitaxy
CVD	Chemical Vapor Deposition	mm	millimeter
CIS	Copper Indium Selenide	Nd:YAG	Neodymium Yttrium Aluminum Garnet
CIGS	$Cu(In_{1-x}Ga_x)Se_2$	PLD	Pulsed Laser Deposition
DSO	Digital Storage Oscilloscope	pm	pico meter
EBE	Electron Beam Evaporation	PMT	Photo Multiplier Tube
ECR	Electron Cyclotron Resonance	SL. No.	Serial Number
EDS	Energy Dispersive Spectrometer	SEM	Scanning Electron Microscope
EDX	Energy Dispersive X-ray	SS	Stainless Steel
e.g.	for example	RF	Radio Frequency
EM	Electromagnetic	RMS	Root Mean Square
FIR	Far Infrared	RT	Room Temperature
FS	Fused Silica	SRIM	Stopping Range of Ions in Matter
FM	First Mirror	TRIM	Transport of Ions in Matter
FTIR	Fourier Transform of Infrared	UHV	Ultra-high Vacuum
FWHM	Full Width at Half Maximum	UV	Ultra Violet
GHz	giga hertz	XRD	X-ray Diffraction
He	Helium		
He:Ne	Helium Neon		
HF	Hydro flouric Acid		

SYMBOLS

~	approximately	λ	wavelength
a	fringe shift	Δm	supersaturation
b	fringe width	µm	micro meter
c	speed of light	Mo	molybdenum
cm	centimeter	nm	nano meter
B_p	background pressure	ns	nano second
Cr	chromium	r	radius of curvature
Cu	copper	R	actual deposition rate
D	deuterium	R_o	reflectivity of a perfectly smooth surface
D_{ts}	target-substrate distance	% R	reflectivity
e^-	electron	R_e	equilibrium deposition rate
E	ion energy	R_P	ion range
f	focal length	Rh	rhodium
Fe	iron	S_P	ion straggle
H	hydrogen	σ	RMS surface roughness
h	Planck's constant	t	thickness
Hz	hertz	T_s	substrate temperature
I_{max}	maximum intensity	T_d	duration of deposition
I_{min}	minimum intensity	V	fringe visibility
kJ	kilo joule	V_i	vacancies/ion
K	Boltzmann constant	W	tungsten
lb	pound	Y	sputtering yield
lit/s	liter per second		

Chapter 1

1. Introduction

First Mirror (FM) is the plasma facing component of optical diagnostics system in a fusion reactor.[1-7] The FM reflects optical radiation emitted from the fusion plasma towards the optical detection system. The use of FMs in optical diagnostics system is one of the conventional diagnostic techniques to characterize plasma.[1-3,5-11] The plasma of a fusion reactor emits characteristic radiations in a wide spectral range from X-ray to Far Infrared (FIR)[1-3,5,6] which carries the information about the plasma parameters. The self-sustained fusion reactions in a reactor are governed by the fusion plasma parameters.[9-13] Therefore, detailed information about the plasma parameters: temperature, density, energy confinement time and ion dynamics, etc. are very important for the effective control of self-sustained fusion reactions.[8-14] The plasma parameters can be measured by monitoring the characteristic radiation emitted from the plasma.[15,16] The line spectra carry the information about the ions and neutrals present in the plasma.[15] The ratio of line intensity of two species reveals electron temperature.[17-23] The splitting of spectroscopic lines due to stark effect determines local electric field.[15,16] The Stark broadening of a spectral line is used to measure the electron density of the plasma.[15,16,20,21] Motional stark effect is used to determine the magnetic field of plasma.[15,16] The dependence of Doppler broadening of an emitted line of an ion onto the ion velocity in the plasma, is used to determine the ion

temperature.[15,16]

In order to diagnose the fusion plasma using emitted Electromagnetic (EM) radiation in Ultraviolet (UV)-FIR range, it is being planned to introduce several FMs at various locations inside a fusion reactor.[10,24,25] The FMs as well as the first wall of the fusion reactors are exposed to the harsh environment due to high particle density (charge exchange neutrals, ions and neutrons), heat flux up to several MW/m^2 and EM radiation.[1-7,14,24,26-37] In the main chamber of a fusion reactor, the particle flux is expected to be ~ 10^{17} particles/cm^2/s having energy ~ 200 eV whereas that of in the diverter region it is ~ 10^{20} particles/cm^2/s having energy ~ 15 eV.[25] The FMs placed in the poloidal location of a fusion reactor are expected to be exposed with particles of energy of few tens of keV to hundreds of keV having particle flux ~ 10^{14} particles/cm^2/s.[38] One of the sources of these highly energetic particles is the neutral beam injection in the core of the plasma of fusion reactor.[39-42] Some of these particles escape out from the core of the plasma via various interactions.[43-45]

The energetic particles and heat flux can cause significant lattice damage to the FMs. Under such harsh environment, the main degradation processes of FMs are, (a) volumetric swelling due to neutron bombardment, (b) erosion by charge exchange neutrals and re-deposition of the eroded material onto FM surface and (c) mirror surface heating due to X-Ray and UV radiation.[3] It was reported that even a 10-20 nm thick contaminated impurities onto the mirrors can drastically change the optical property of metal mirrors.[1] The degradation of the optical quality of FMs in such a harsh environment is a serious concern for the reliability of spectroscopy based optical diagnostics.[10,28]

There are several reports on the search of appropriate material for plasma

facing components in a fusion reactor.[1,3,24,28,31] It has been realized that the heavy metals: molybdenum (Mo), tungsten (W), rhodium (Rh), copper (Cu) and stainless steel (SS) alloy are preferred material for the fabrication of plasma-facing component and for FMs.[4,9,24,46-55] All these heavy metals have high reflectivity, high electrical conductivity, high melting temperature and mechanical strength, good metal barrier performance and fine patternability, etc.[27,30,56-59] The damage properties of the heavy metals, Mo, W, Cu and SS due to fusion-like hostile environment exposure by ion beam irradiation experiment has been reported in literature.[25,28,60-65]

The formation of blisters on the surface of bulk W crystal due to irradiation of Deuterium (D) ions of energy ~ 38 eV having particle flux ~ 10^{16}-10^{18} particles/cm^2/s has been reported.[64,65] The lattice damage due to irradiation of ~ 200 eV D ions having particle flux ~ 10^{14} particles/cm^2/s has also been reported.[66] A reduction of ~ 5-15 % UV-visible reflectivity of Mo FMs was observed due to irradiation of ~ 200 eV D ions having particle flux ~ 10^{15} particles/cm^2/s.[30] The Rh FMs exposed to ~ 300 eV D ions having particle flux ~ 10^{15} particles/cm^2/s showed a reduction of UV-visible reflectivity ~ 1-15 %.[26] The deuterium retention and lattice damage due to exposure of 6 keV D ions having particle flux ~ 10^{15} particles/cm^2/s on bulk W has been reported by Alimov et al.[60] Averback et al. has reported the lattice defect production similar to that of fusion reactor in Cu thin films due to irradiation of Hydrogen (H), D, Helium (^{3}He) and ^{4}He ions in the energy range of 15-40 keV.[51] The lattice damage and formation of blisters on the surface of bulk W sample due to 300 keV and 700 keV H^- ion beam irradiation has been reported by Fukumoto et al.[46] The fabrication of bulk single crystalline Mo FM and degradation of its optical reflectivity by ~ 40-60 % in the wavelength range of 400-1000 nm and ~ 5-20 % in the

wavelength range of 400-2500 nm, due to the exposure in the harsh environment of fusion reactor, has been reported by Litnosvky et al.[28] and Lipa et al.[31], respectively. The optical reflectivity degradation by ~ 20-30 % in the wavelength range of 200-800 nm due to irradiation of He^+ ions onto SS FM is reported by Urabe et al.[9]

The mirrors of mono-crystalline refractory heavy metals (W, Mo, Rh) can have sufficiently long lifetime in fusion reactor[1] as they have very low sputtering yield and high thermal stability. Due to these unique properties, heavy metal mirrors are able to maintain its optical quality for longer duration of exposure. Thus, mirrors of heavy metals are foreseen as a part of diagnostics system in a fusion reactor for detection of EM radiation in FIR to UV-visible range. There are several reports on the use of bulk as well as thin film FMs of heavy metals.[1-7,9-11,24,26-33,46,67-71] The growth of bulk crystal of heavy elements: W, Mo, Rh with good polished surface is expensive[4,26,27] and a difficult task. A simple alternative is to use the thin films of heavy metals on suitable substrates.[26-30] The SS substrate is used[4,26] due to its better mechanical strength against harsh environment. The fabrication of Mo thin film FMs and the investigation on the effect of deuterium plasma exposure to the FMs has been reported by Eren et al.[30] and Voitsenya et al.[2] The optical reflectivity of W thin film ~ 40-58 % and that of Cu thin film ~ 60-90 %, having thickness from few hundreds of nanometers to few microns, are reported by Voitsenya et al.[1,2] and Orlinski et al.[4] The optical reflectivity of Rh thin film ~ 65-90 % in the wavelength range of 400-2000 nm and 300-1700 nm has been reported by Marot et al.[26,27,72] and Passoni et al.[73], respectively. The thin film mirrors can be easily scaled to larger dimensions, one of the requirements of FMs, compared to the bulk.[1] The reflectivity of the heavy metal thin films is quite close to that of the mirrors made out of bulk crystal.[1,4,74] Apart from

this, the grain size in metal thin films is smaller compared to that of bulk crystals.[1] The micro-relief due to ion bombardment in small grains is low compared to large grains.[1] The lower micro-relief in case of thin film helps in maintaining its optical reflectivity for long-term exposure of harsh environment in fusion reactor.[1]

Apart from application as FM, there are various other potential applications of heavy metal thin films. The thin films of Mo, W and Cu are being used as a back contact electrode for semiconductor based thin film solar cells[75-81] and in microelectronic industries.[82-90] Micro-nano metal grating fabricated by these metal thin films can be used for highly sensitive molecular sensor in the micro-fluidic technology.[91-93] The heavy metal thin films are also used as X-ray mirrors as well as X-ray masks[58,94-97], spintronics[98-100], film thermometer[101], catalysts[102-107], etc. The heavy metal thin films has also potential application in memory devices.[108]

1.1 Fabrication techniques for heavy metal thin film

Metallic thin films can be fabricated by thermal evaporation, Electron Beam Evaporation[109,110], Molecular Beam Epitaxy[111], Sputtering[56,112-118], Chemical Vapor Deposition[111,119-127], and Pulsed Laser Deposition technique[73,85,111,128-132].

Thermal evaporation is one of the most common and simple deposition techniques. In this, the target material is heated to its evaporation temperature inside a vacuum chamber.[111,119] An electron beam or electrical resistive heating can be used to evaporate the target material. When electron beam is used, the technique is known as Electron Beam Evaporation (EBE) and when electrical resistive heating is used, the technique is simply termed as thermal evaporation. The target source material is usually kept at the bottom of the vacuum chamber and the substrate is placed few cm apart on top of the target. Inside vacuum chamber, even a relatively low vapor

pressure is sufficient to raise the vapor cloud of target material. The vapor cloud traveling upward direction, strikes the substrate and deposits on it. Thin films of target material having lower evaporation temperature can be easily grown by this technique using resistive heating. For target material having high melting point, electron beam evaporation technique can be implemented. The evaporation technique has rather poor control on the quality of the thin films.

The limitation of evaporation technique can be overcome by, Molecular Beam Epitaxy (MBE) technique. MBE is more advanced than that of vacuum evaporation technique.[133,134] MBE is an epitaxial thin film growth process involving the generation of one or more thermal beams of atoms or molecules and their reactions at the substrate to form a crystalline thin film under ultra-high vacuum conditions.[133,134] It offers much more precise control over the deposition parameters. This technique is particularly used to fabricate III-V semiconducting materials.[119] To maintain the high purity and integrity of the deposit, stringent vacuum conditions are needed.[133] The requirement of ultra-high vacuum and complex hardware to control stringent processes of MBE, made this technique to be expensive to operate.[119]

The sputtering technique can be employed for fabrication of large variety of thin films.[119] In this technique, solid target surface is bombarded with energetic ions to sputter atoms or molecules from its surface.[119] The sputtered species from the target get deposited on a suitably placed substrate, a few cm apart from the target. The energetic ions in sputtering technique can be generated by DC discharge, RF discharge and magnetron discharge.[135] DC sputtering system consists of a pair of planar electrodes. The cold cathode's front surface is covered with the metal target and the substrate is placed on anode. The sputtering chamber is filled with sputtering

gas, usually Argon (Ar). The glow discharge is maintained in the chamber by applying DC voltage between the electrodes.[135] The Argon ions (Ar^+) generated in glow discharge is accelerated towards cathode for sputtering the target material. DC sputtering technique is suitable for conducting material as the glow discharge (i.e. current flow) is to be maintained between the metallic electrodes.[135] In case of target of insulating material, sputtering discharge cannot be sustained due to the immediate buildup of positive charge on the front surface of the target.[135] To sustain glow discharge, RF electric field is applied. The deposition rates for DC or RF sputtering technique is lower than that of the other vacuum deposition techniques.[135] The deposition rate for this technique can be controlled by Ar gas pressure. To maintain the sufficient Ar^+ ions, magnetron discharge is used.[135] In sputtering technique, it is difficult to preserve the stoichiometry of the target.

Chemical Vapor Deposition (CVD) technique is mainly applicable to non-metallic hard coatings, dielectric thin films, single crystal semiconductor thin films, etc.[111,136] There are reports on the fabrication of heavy metal thin films also by CVD technique.[121-127] In this, a volatile compound is decomposed inside the coating chamber. For this, a relatively high temperature (> 700 °C) is required.[121,123] The decomposed species chemically reacts with other gases to produce nonvolatile species which deposits on a suitably placed substrate. The deposited material is chemisorbed on the surface of the substrate. The remaining decomposition fragments are pumped away from the vacuum chamber.

Pulsed Laser Deposition (PLD) technique is the most versatile technique.[131,137-142] The complex compounds of superconductors, oxides, ferroelectrics, semiconductors, metals and dielectrics are easily grown by PLD

technique.[131,137-141,143] This technique can be used with equal ease to fabricate heavy metal thin films among its other competitive techniques.[70,71,73,144,145] The thin film quality can be easily tuned by varying the deposition parameters. In the present work, PLD technique is used to fabricate the thin films of Mo, W and Rh. A brief discussion on PLD technique is presented in the next section.

1.2 Pulsed Laser Deposition (PLD) technique

PLD technique was first proposed in the early 1960s[138], just after the invention of high power ruby laser. The PLD technique was first demonstrated by Smith and Turner in 1965.[146] In this technique, the target material is ablated by focusing a high power pulsed laser beam onto the target. Normally, nano-second pulsed lasers are used for thin film fabrication using PLD technique.[131,137-141,143-156] The schematic diagram of PLD technique is shown in the figure 1.1. The focusing of the laser beam onto the target leads to the formation of Laser Induced Plasma (LIP) of the target material. The LIP expands in vacuum or in presence of ambient environment. The ambient gas pressure of the ablation chamber may vary from ~ 10^{-6} mbar to several mbar. The expanding plasma cools down and deposits on the substrate placed parallel to and few cm apart from the target. Usually, the substrate holder has the provision to

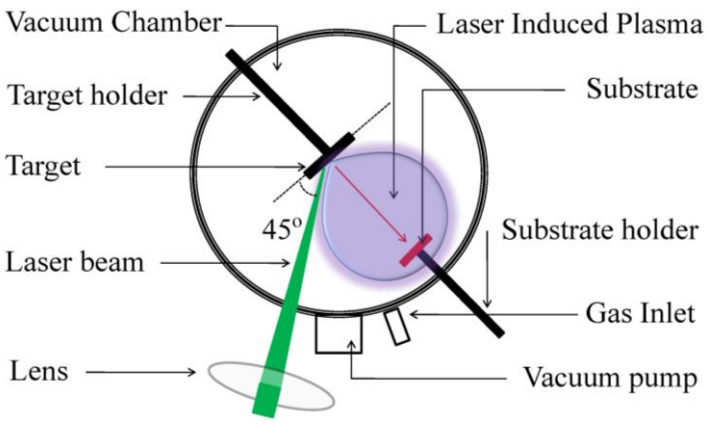

Figure 1.1. Schematic diagram of PLD technique.

control the temperature of the substrate as high as 800 °C or more. Initially, the ablation chamber is evacuated to a base pressure of ~ 10^{-6} mbar. After that, as per requirements of the particular film, different types of ambient gas can be filled inside the ablation chamber through appropriate gas inlet ports. The physical processes of material ablation and thin film deposition via PLD technique are extremely complicated.[131,139-141,143,146-158] The quality of PLD thin films are governed by the laser fluence, laser wavelength, ambient gas pressure, substrate temperature, target-substrate distance, etc. Normally, the deposition is performed at a laser intensity > 10^8 W/cm^2. In this intensity regime, the initial absorption of laser radiation is governed by multi-photon absorption process. This results into the formation of LIP plume of target material in the focal regime of the laser beam. The LIP expands in presence of ambient gas.[131,139] The expansion of the plasma depends on the laser focal spot onto the target, plasma parameters, ambient gas pressure, etc.[131] The expanding plasma absorbs further energy from the laser beam through inverse Bremsstrahlung process. The temperature and density of the LIP in the neighborhood of the target are very large, but falls down very rapidly as the plasma moves away from the target with high expansion velocity, ~ 10^6 m/s, because of the pressure gradients.[156,159] During the laser ablation of the target material, the ambient gas atoms/molecules may also undergo ionization/plasma formation through multi-photon absorption. Both the target and ambient gas plasma undergo adiabatic cooling and forms molecular species under suitable dynamics. The molecular species within adiabatically cooled plasma condensates and then nucleates onto the substrate surface, initiating the formation of thin film. The nucleation and growth of the film depend on the kinetic energies of the species impinging on the substrate and thermo-physical properties of the substrate.[131]

The two main thermodynamic parameters which govern the thin film growth are the substrate temperature (T_s) and the plasma flux supersaturation (Δm).[160] The plasma flux supersaturation is expressed as, $\Delta m = kT_s [\ln(R/R_e)]$, where the parameters "k", "T_s", "R" and "R_e" are Boltzmann constant, substrate temperature, actual deposition rate and equilibrium deposition rate, respectively.[160] In typical PLD process, kT_s is ~ 2.5×10^3 J/mol, $R/R_e \sim 10^7$ and hence, Δm is ~ 10^5 J/mol.[160] This high degree of supersaturation or high deposition rate generates two-dimensional nucleation with monoatomic height which is suitable for layer by layer thin film growth.[160,161] Higher substrate temperature is suitable for defect free crystalline thin film growth. At lower substrate temperature, crystal growth may be overwhelmed by energetic particle bombardment which may result in disorder or even amorphous structures of the thin film.

The PLD technique has many advantages.[131,137-141] It possesses high degree of flexibility in the geometrical arrangements. It is applicable to any material: oxides, nitrides, carbides, polymers, pure metals, dielectrics etc. Since, the target material is selectively ablated just in the area of small focal spot of the laser beam therefore, the consumption of target material is extremely low. The stoichiometric transfer from target to the substrate is extremely high in this technique. It is possible due to the fast and strong heating of the target surface by intense laser beam and near simultaneous evaporation of target components irrespective of their partial binding energies. The kinetic energy of the ablated species can be tuned easily to control the surface morphology and the crystal orientation of the film.

The PLD technique has some technical limitations.[141,157] The formation of macroscopic liquid droplets is very common in metallic thin films. Crystallographic

defects in the film are produced by the bombardment of high energetic laser ablated species. Inhomogenous density and angular energy distribution within the plasma plume leads to the non uniform deposition of the film. Large area coating is difficult due to non uniform deposition. However, some of these limitations can be overcome by careful tuning of the laser fluence and other deposition parameters.

1.3 The present work

In the present work, detail studies on the fabrication and characterization of Mo, W and Rh mirror-like thin films by PLD technique was undertaken which can find its application as FM in fusion reactors. As the FMs has to withstand the hostile environment of a fusion reactor due to the high particle flux of fusion fuel material (H, D, etc.), the effect of H and D ion beam irradiation onto the optical reflectivity of thin FMs is also studied. The scope to enhance the quality and sustainability of single layer thin film FMs by multilayer coating of heavy metals in appropriate sequence and thickness is also undertaken. The design of multilayer thin film FMs requires a study on the damage parameters due to the bombardment of ion beams. Therefore, systematic numerical and experimental studies have also been proposed to design and fabricate multilayer thin films. Finally, PLD setup was modified by incorporating the rastering stage for substrate so as to scale the size of the thin films for uniform deposition up to a diameter of 50 mm.

1.4 Organization of the present thesis

The entire thesis is divided into the following eight chapters:

The second chapter, Chapter 2, "*Experimental details*", describes the basic design and assembles of PLD system, Michelson interferometer setup and ion beam irradiation setup. The techniques used to characterize the PLD thin films are also

listed in this chapter. The Chapter 3, "*Pulsed laser deposition and characterization of thin films of Mo, W and Rh*", discusses the effect of various deposition parameters on the quality of mirror-like thin films of Mo, W and Rh. The optimized deposition parameters for best quality thin films are documented towards the end of this chapter. The effect of ion beam irradiation onto the quality of W and Rh thin films is discussed in Chapter 4, "*Effect of ion beam irradiation on W and Rh thin films*". The design and fabrication of multilayer thin films as well as the effect of ion beam irradiation onto the quality of the multilayer thin film is presented in Chapter 5, "*Design, fabrication and D ion irradiation on Rh/W/Cu multilayer thin film*". The deposition of single layer Rh and multilayer Rh/W/Cu thin films on 50 mm diameter highly polished SS substrate by modified PLD technique is presented in Chapter 6, "*Rh and Rh/W/Cu thin films on 50 mm diameter SS substrate*". Finally, the concluding Chapter 7, "*Conclusions*", of thesis summarizes the salient features of the present research work along with the possibilities of future explorations.

Chapter 2

2. Experimental details

First mirrors made up of thin films of Mo, W, Rh, etc. offer a cost effective alternative to their bulk crystal.[26] There are various techniques documented in literature for the deposition of such thin films.[112-117,119,121-125] Among them, the Pulsed Laser Deposition (PLD) technique is quite flexible for fabrication of thin film of heavy metal having very high melting point. In the present work, a detail parametric characterization was undertaken by PLD technique to fabricate the thin films of single elements of Mo, W, Rh and multi-component Rh/W/Cu. To test the sustainability of these thin films in the harsh environments similar to that of fusion reactor, the films prepared at optimum deposition parameters were subjected to H and D ion beam irradiation. The pre and post ion beam irradiated reflectivity of the thin films in FIR-visible-UV range were compared.

In this chapter, various experimental setups developed for the fabrication of thin films, its characterizations and ion beam irradiation are described.

2.1 Substrate preparation

In order to obtain the mirror-like thin films, the surface of substrates should be cleaned and well polished. All the thin films reported in the present work were deposited on well polished Stainless Steel (SS) substrates. The substrates of sizes (a) 10 mm × 10 mm × 2 mm, (b) 10 mm diameter, 2 mm thick, (c) 25 mm diameter, 5

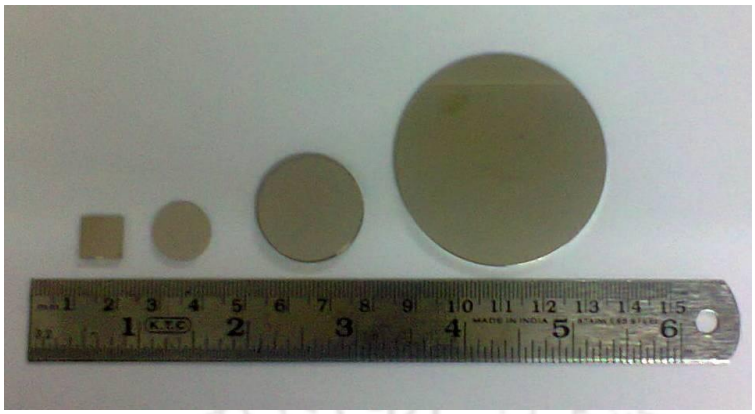

Figure 2.1. Photograph of SS substrates.

Table 2.1. Polishing stages

Stage	Duration of polishing	Abrasive Paper	Force (1 lb = 0.453 kg)
1	~ 60 minute	400 dpi	120 lb
2	~ 30 minute	600 dpi	120 lb
3	~ 10 minute	Diamond paste	100 lb
4	~ 03 minute	Alumina paste	100 lb

mm thick and (d) 50 mm diameter, 5 mm thick were used to deposit the thin film via PLD technique. The photographs of mirror polished SS substrates are shown in figure 2.1. Apart from the 50 mm diameter well polished substrate, which was procured commercially, all other kind of substrates were polished in-house by Variable Speed Grinder-Polisher machine (model EcoMet 3000, BUEHLER) in four stages as detailed in table 2.1. The SS substrates were initially coarse polished by 400 dpi abrasive paper of SiC for ~ 60 minute duration using water as coolant. This initial polishing removed the deep scratches on the substrate surface. In the second stage, the substrates were polished with 600 dpi paper till the visible scratches on the surface disappeared. The downward load on the substrates for both these stages was

maintained at ~ 120 lb. In the third stage, the substrates were polished with diamond pastes of different grain sizes using diamond polishing cloth. Meta-DI fluid was used as coolant for polishing with diamond paste. The polishing was performed by using diamond grains of size 6, 3, 1 μm and finally by 0.25 μm in succession. The mirror finish was finally obtained by polishing with 0.05 μm alumina paste with water as coolant and the diamond polishing cloth was replaced with another soft cloth. The downward load applied to the substrates during polishing with diamond and alumina paste was maintained at ~ 100 lb. The typical grinding speed was ~ 200-250 rpm. After polishing, the substrates were cleaned by usual cleaning protocols (a) sonication in acetone solvent for ~ 60 minute, (b) dipped in ~ 4 % HF solution for ~ 10 second, (c) rinsed thoroughly with acetone and then (d) dried with hot air.

2.2 Pulsed Laser Deposition setup

The schematic diagram of experimental PLD setup used for deposition of single and multilayer heavy metal thin films is shown in figure 2.2. The second harmonic of a high power *Q*-switched Nd:YAG laser (Model No: Quanta system HYL101, ~ 8 ns pulsed duration, 10 Hz repetition rate) was steered into the multiport ablation chamber with a high damage threshold right angled prism through a view port. The laser beam was focused by a plano convex lens onto the metal target. Focusing of laser beam onto the target leads to the plasma formation. The plasma expands in ambient environment, cools down and deposits onto the substrate placed parallel to and few cm apart from the target.

In the initial phase of the thesis work, single layer thin films of Mo and W were deposited in a cylindrical shaped multiport ablation chamber made up of SS, which was evacuated with diffusion pump backed by rotary pump. The photograph of

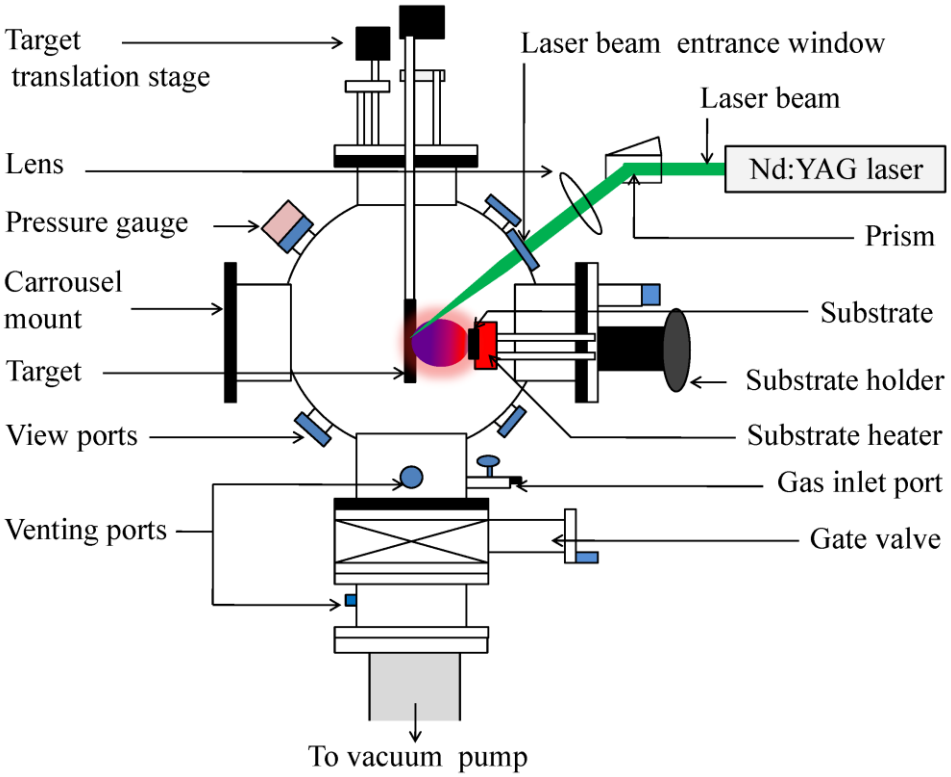

Figure 2.2. Schematic diagram of PLD setup.

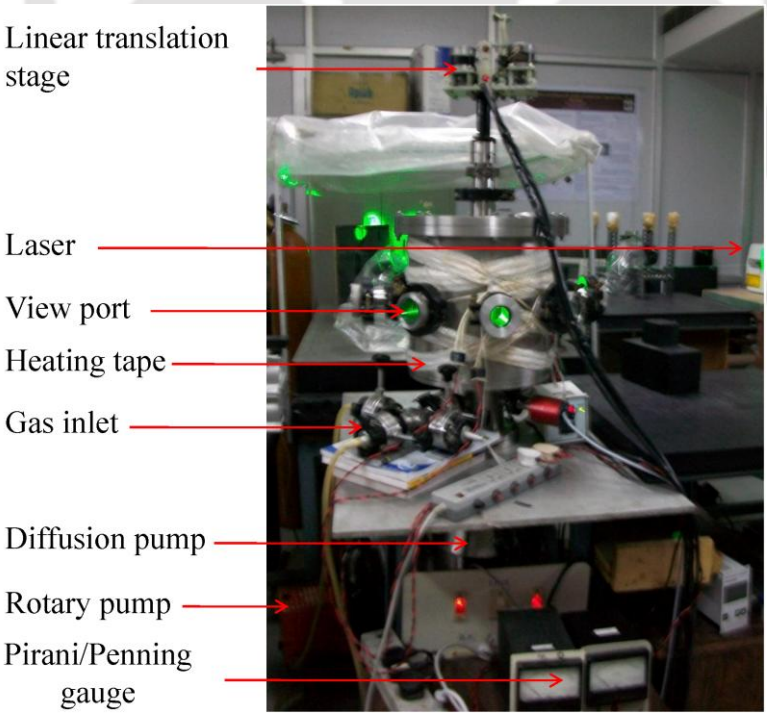

Figure 2.3. Photograph of PLD setup (evacuated with diffusion pump).

ablation chamber is shown in figure 2.3. A plano convex lens of focal length 35 cm was used to focus the laser beam onto the target through one of 50 KF ports. The Mo and W (99.965 % pure) targets were in the form of strips of size 25 mm × 18 mm × 2 mm. In order to avoid drilling of the target due to repeated shots of the laser beam, it was mounted on a vertical linear motorized translation stage from the top port of the chamber. The translation stage was continuously translated during deposition via motorized feedthrough interfaced with a microprocessor. The translation speed was maintained at ~ 2.5 mm/minute. This provides the fresh target surface on shot to shot basis of the laser beam during deposition process. The SS substrate was mounted onto the substrate holder having provision of resistive heating to raise the temperature up to 800 °C. The target-substrate distance can be adjusted from outside the chamber by moving the feedthrough substrate holder.

Later on, in order to avoid the possibility of oil contamination, the diffusion pump was replaced by turbo molecular pump. Another spherical shaped multiport ablation chamber was designed and installed. The photograph of the spherical SS ablation chamber is shown in the figure 2.4(a). The oil free turbo molecular drag pump (Model No: Pfeiffer HiPace 700, pumping speed 685 lit/s) used, was capable of achieving base pressure below 10^{-6} mbar. The Rh, W and the multilayer PLD thin films of Rh/W/Cu were fabricated in this ablation chamber. The Rh thin films were deposited by mounting a Rh rod (99.98 % pure) of length 5 mm and diameter 1 mm on the vertical linear translation stage, shown in photograph 2.4(b). The vertical linear translation stage was mounted from the top 160 CF port of ablation chamber. For deposition of W thin film using a flat target, a multi-target carrousel was installed at 160 CF side port. In case of multilayer thin film deposition, the Rh target was

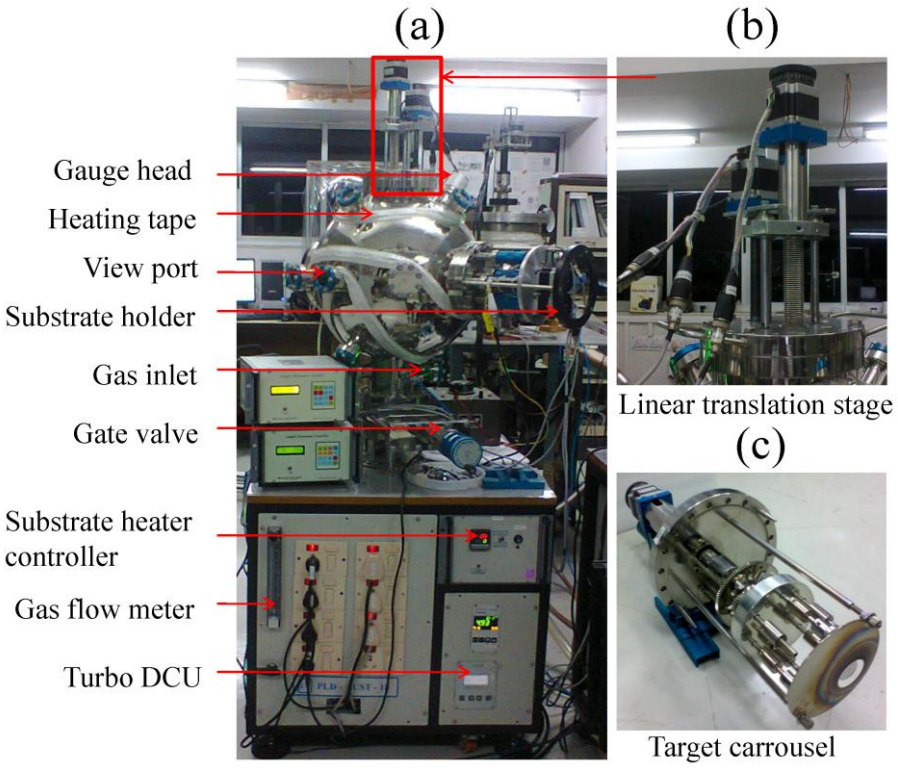

Figure 2.4. (a) Photograph of PLD setup (evacuated with turbo molecular pump), (b) linear translation stage and (c) target carrousel.

mounted on the vertical linear translation stage and the W and Cu targets were mounted on the multi-target carrousel. The W (99.965 % pure) and Cu (99.965 % pure) in the form of plates of sizes 25 mm × 18 mm × 2 mm and 25 mm × 25 mm × 0.5 mm, respectively were glued with silver paste onto the two separate target slots of the carrousel. Photograph of the multi-target carrousel is shown in figure 2.4(c). The multilayer thin films were fabricated without breaking vacuum of the ablation chamber. First, Cu was deposited onto the substrate, followed by W deposition by changing the target with the rotation of carrousel stage. During deposition of W and Cu thin films, the vertical translation stage was moved to its extreme top position so as to avoid the Rh target coming on the path of laser beam. The rastering frequency was maintained at 10 Hz for deposition of W and Cu thin films. The rastering angle

was set to ~ 2°. The substrate holder was installed from another side 160 CF port, opposite to the carrousel port. The substrate temperature can be controlled by programmable heater from Room Temperature (RT) to 800 °C.

Both the ablation chambers were baked to ~ 70-80 °C for ~ 14-15 hour while evacuating prior to deposition. For this, the chamber was wrapped with heating tapes which is shown in both the figures 2.3 and 2.4(a). The baking helped in degassing the residual oxygen molecules and water vapor from the inner wall of ablation chamber and pumped out. The films were fabricated under high vacuum ~ 10^{-5}-10^{-6} mbar to few mbar of Argon (Ar) and Helium (He) inert gas. The pressure inside the ablation chambers was measured by using pirani, penning and capacitance gauges mounted at suitable port as shown in figure 2.3 and 2.4.

2.3 Michelson interferometer setup

The fringe visibility, curvature present in the mirror-like thin films and thickness of the film were measured by recording interference pattern.[71,145,162] For this, a Michelson interferometer was assembled as shown in figure 2.5(a). A well collimated He:Ne laser (Model No: Melles Griot 05-LHP-827, 75 mW power) beam was obtained by passing the laser beam through a spatial filter and a collimating lens. The collimated He:Ne laser beam was divided by a cube beam splitter. The transmitted beam from the beam splitter was allowed to fall onto the commercial flat mirror and the reflected beam was directed to the PLD mirror-like thin film. The reflected beams from both the mirrors were recombined at the beam splitter to produce interference pattern which was recorded by a CCD (Model No: PCO PixelFly) interfaced with a computer. The pixel to pixel distance in CCD sensor was 5.7 µm. The interference pattern obtained by using commercial flat mirror in both the

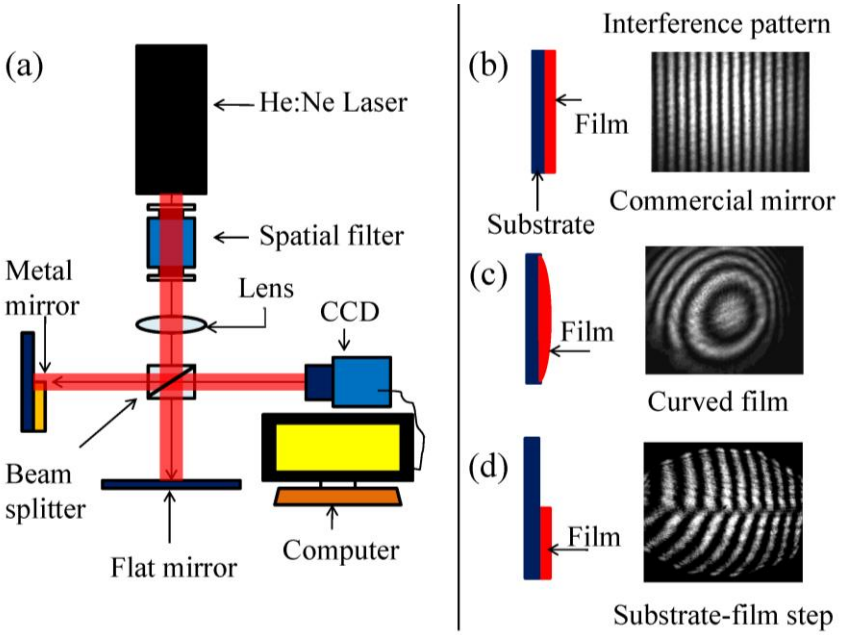

Figure 2.5. (a) Schematic of Michelson interferometer setup, interference pattern, (b) commercial mirror, (c) curved mirror and (d) substrate-film step.

arms of the Michelson interferometer produced the straight and distinct interference pattern as shown in figure 2.5(b). When one of the mirrors is replaced with the thin films having some curvature, a curved interference pattern is obtained as shown in figure 2.5(c). The radius of curvatures of PLD mirror was calculated by measuring the radius of curvature of the circular fringes, given by equation (2.1)

$$r = \frac{r_{n+1}^{\ 2} - r_n^{\ 2}}{\lambda} \quad \text{----------} \quad (2.1)$$

where "r" is the radius of curvature of the PLD mirror, "r_{n+1}" and "r_n" are the radius of $(n+1)^{th}$ and n^{th} circular fringes and "λ" is the wavelength of He:Ne laser beam, 632.8 nm.

To measure thickness, the film was partially deposited by placing a mask onto the substrate to form a substrate-film step. The reflected laser beam from this step showed fringe shift in the interference pattern, figure 2.5(d). By measuring the fringe

shift "*a*" and fringe width "*b*", the thickness "t" of the film was calculated by using equation (2.2).[162]

$$t = \frac{a.\lambda}{2b} \quad \text{----------} \quad (2.2)$$

To test the optical quality of PLD mirrors, fringe visibility was measured from the intensity distribution of interference pattern. One such interference pattern recorded onto the CCD using experimental setup of figure 2.5(a), is shown in figure 2.6. The intensity distribution along the vertical line marked in the interference pattern is shown in figure 2.6(a). From this, fringe visibility can be calculated using equation (2.3) below.

$$V = \frac{I_{max} - I_{min}}{I_{max} + I_{min}} \quad \text{----------} \quad (2.3)$$

where I_{max} and I_{min} are the maximum and minimum intensity obtained from intensity distribution of interference pattern, figure 2.6(b). The measured fringe visibility of commercial standard mirror was ~ 0.9.

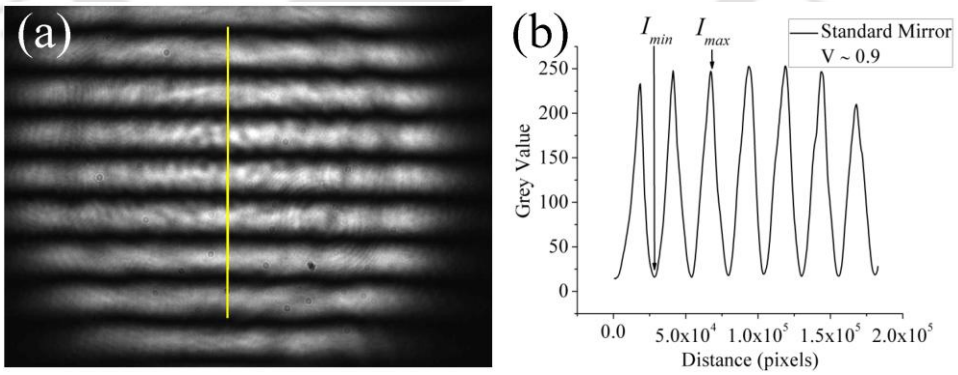

Figure 2.6. (a) CCD image of interference pattern of PLD thin film, (b) intensity distribution along the line drawn on the image of figure 2.6(a).

2.4 Ion beam irradiation setup

To study the effect of harsh environment similar to that of the fusion reactor, PLD mirrors were irradiated by H and D ions beams having energy in range of 8-30 keV and ion flux ~ 1.2×10^{14}-8.9×10^{14} ions/cm^2/s. The schematic diagram and photograph of experimental ion beam irradiation setup are shown in figures 2.7 and 2.8, respectively. The ion beam irradiation setup consists of evacuation pumping system, Electron Cyclotron Resonance (ECR) ion source, ion extraction system, ion

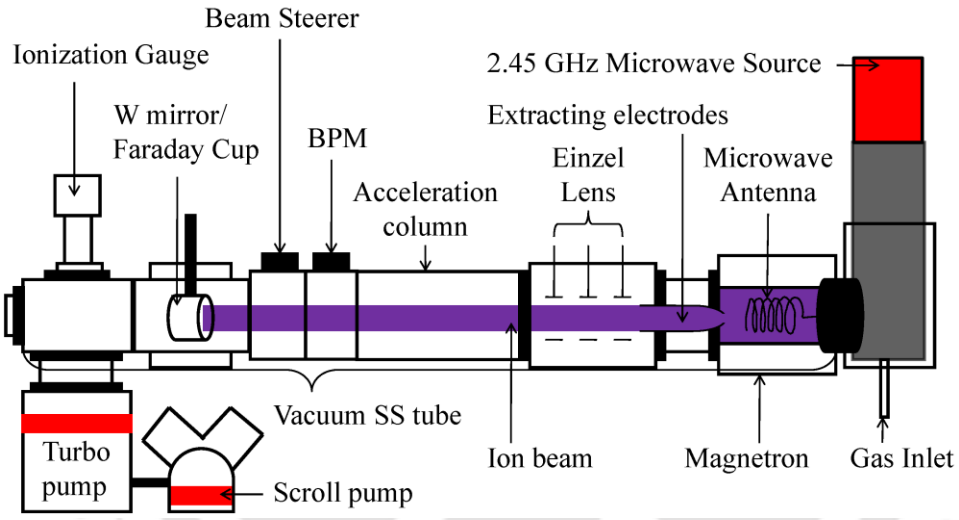

Figure 2.7. Experimental setup for H and D ion beam irradiation.

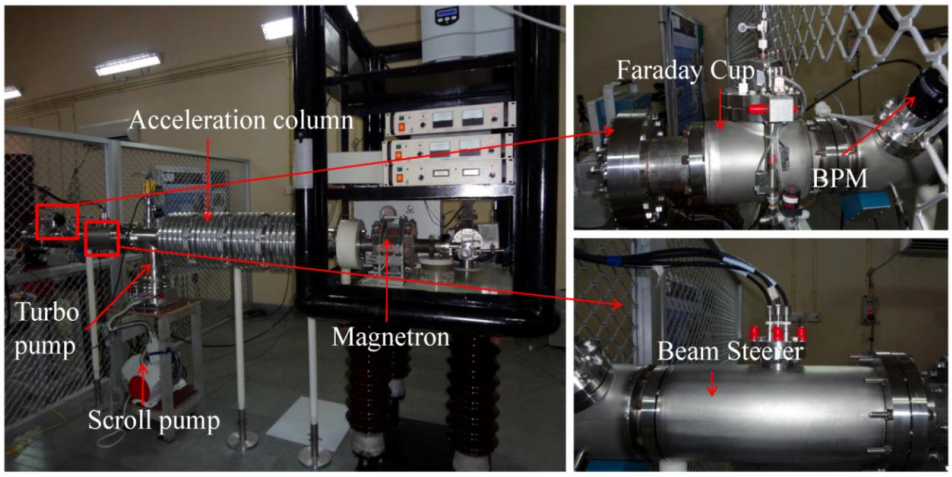

Figure 2.8. Photograph of experimental ion beam irradiation setup.

acceleration column, beam steerer, Beam Profile Monitor (BPM), Faraday cup, high voltage power supply and isolation transformer. The ion beam was generated inside a SS tube, shown in the figure 2.7. The SS tube was evacuated to a base pressure ~ 10^{-6} mbar by a turbo molecular pump (Model No: Pfeiffer HiPace 700, pumping speed 550 lit/s) backed with roughing oil free scroll pump. After achieving a base pressure ~ 10^{-6} mbar, the tube was filled with H (99.96 % pure) or D (99.9999 % pure) gas. The pressure inside SS tube was monitored by ionization gauge. The H/D plasma was generated by 2.45 GHz microwave operated ECR source. This plasma was confined by superimposed axial and radial fields of ECR magnetron. The ion beam from plasma was extracted with the help of extracting electrodes. The extracting electrodes consisted of plasma electrode having 8 mm aperture and puller electrode having 10 mm diameter hole and 150 mm in length. The plasma electrode was kept at + 8 kV and puller electrode was grounded. The extracted beam was shaped by einzel lens consisting of three symmetric cylindrical electrodes each having 45 mm diameter and 35 mm in length. The separation between each electrodes of einzel lens was 10 mm. Both the outer electrodes of einzel lens were grounded. The focusing voltage of central electrode was adjusted from - 5 to - 7 kV with respect to ground. Finally, the ion beam was accelerated in the accelerating column to the required energy for irradiation. The acceleration column consisted of four sections of electrodes. Each section of the accelerating column was rated for 75 kV in air and 200 kV in SF_6. A series of shielding electrodes were mounted inside the column to prevent the inner ceramics surface from ion bombardment and contamination. The maximum holding voltage of accelerating column was 300 kV in air. The high voltages to the electrodes were given through isolation transformer. The diameter of ion beam and particle flux

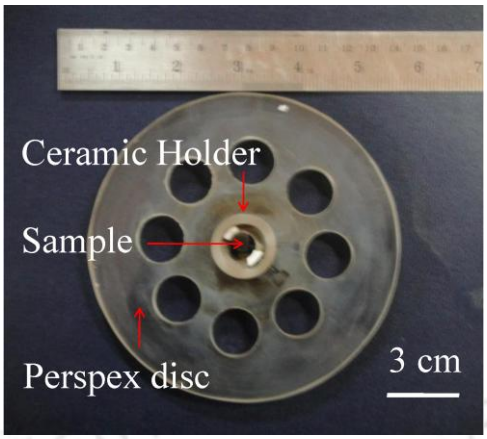

Figure 2.9. Sample holder for ion beam irradiation.

was measured by BPM and Faraday cup, respectively. The Faraday cup was replaced by PLD samples during ion beam irradiation of thin films. The sample to be irradiated was mounted in a ceramic holder as shown in figure 2.9. The ceramic was preferred to metal to avoid the secondary electron produced due to ion bombardment. The ceramic holder was mounted on a perspex circular disc. Eight holes of 25 mm diameters were drilled in the perspex disc for vacuum compatibility. Minor beam alignment was performed by beam steerer, such that the beam exactly fall on Faraday cup or PLD samples. The beam steerer consists of four rectangular plate electrodes assembly which was placed just after the accelerating column. Two electrodes steered the ion beam in X-direction and the other two in Y-direction.

2.5 Characterization of pulsed laser deposited thin films

Single and multilayer PLD thin films were subjected to various characterizations. The thickness of PLD thin films was estimated by Stylus surface profilometer and interference technique (Section 2.2). The substrate-film step was formed by placing a mask on the substrate while film deposition. In the profilometer (Model No: Veco Dektak 150), the substrate-film step was scanned linearly at three

different locations by a 12.5 μm diamond-tipped stylus and their average was taken.

The cracks on film surface, eruption of the film from substrate, formation of the liquid droplet were investigated by recording topological images using commercial Scanning Electron Microscope (Model No; Leo 1430VP) equipped with Energy Dispersive Spectrometer (EDS). The elemental composition was identified by analyzing Energy Dispersive X-ray (EDX) spectra.

The Root Mean Square (RMS) surface roughness of PLD thin films were measured by subjecting the samples to Atomic Force Microscope (AFM). The 3D image of surface was recorded by commercial AFM (Model No: NT-MDT) at six different location of the same sample. The RMS surface roughness was calculated by taking the average over six different scans of 2 μm × 2 μm areas on each film. The AFM images were recorded in non-contact mode.

X-ray Diffraction pattern was recorded to identify the crystal structures of PLD thin films. The XRD patterns of thin film were recorded by commercial X-ray Diffractometer (Model No: Seifert 3003TT) employing Cu K_α (1.54 Å) radiation. In the present investigation, the grazing angle of incidence was set to ~ 2°.

The specular reflectivity in FIR range of the PLD thin films before and after ion beam irradiation was recorded by FIR spectrometer (Model No: Perkin Elmer FTIR spectrum BX). The spectra were recorded at 17.5° angle of incidence. The UV-visible reflectivity of PLD thin films were recorded at 45° angle of incidence by UV-visible spectrometer (Model No: Varian Cary 50). The base line correction for both of the spectrometers was made by using commercial standard aluminum mirror. The reflectivity is measured with reference to aluminum standard mirror.

Chapter 3

3. Pulsed laser deposition and characterization of thin films of Mo, W and Rh

Mirror-like thin film of heavy metals Mo, W and Rh are being viewed as simple alternative to First Mirror (FM) made up of the bulk crystals. The heavy metal thin film can be deposited by Pulsed Laser Deposition (PLD) technique. In the present chapter, the characterization of Mo, W and Rh thin films deposited by PLD technique over a wide range of deposition parameters is presented. The pulsed deposition setup used to fabricate Mo, W and Rh thin films has already been described in section 2.2, chapter 2.

3.1 Characterization of pulsed laser deposited thin films of Mo

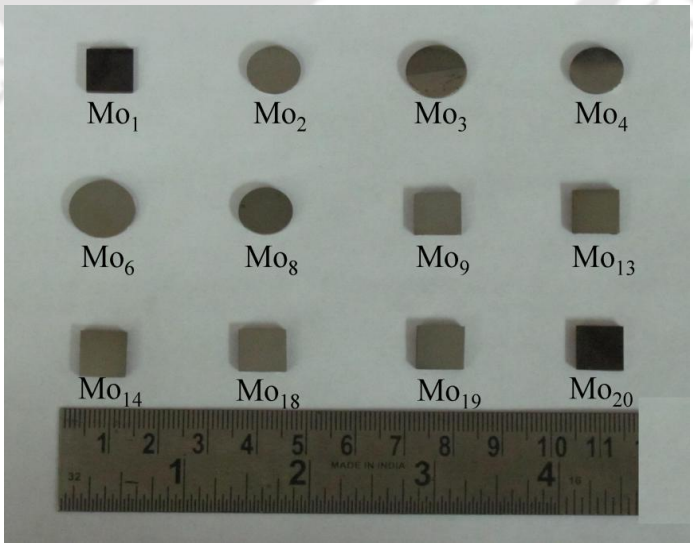

Figure 3.1. Photographs of Mo thin film samples.

Photographs of some of the Mo thin films deposited by PLD technique at various deposition parameters are shown in figure 3.1. In totality, there were twenty

Table 3.1. Sample codes and detail deposition parameters of Mo thin film samples.

SL. No.	Sample Code	Focusing condition (laser fluence)	Ablation chamber condition	T_s (^oC)	D_{ts} (cm)	B_p (mbar)	T_d (minute)
1	Mo_1	Tight (~ 57 J/cm^2)	Not baked	RT	2	0.05 (Argon)	30
2	Mo_2		Baked	RT	2	0.05 (Argon)	30
3	Mo_3		Baked	RT	3	10^{-5}	60
4	Mo_4	Loose (~ 2 J/cm^2)	Baked	RT	3	10^{-5}	60
5	Mo_5		Baked	RT	3	10^{-5}	120
6	Mo_6		Baked	500	3	10^{-5}	120
7	Mo_7		Baked	500	2	10^{-5}	180
8	Mo_8		Baked	500	3	10^{-5}	180
9	Mo_9		Baked	500	4	10^{-5}	180
10	Mo_{10}		Baked	500	5	10^{-5}	180
11	Mo_{11}		Baked	500	3	0.05 (Helium)	60
12	Mo_{12}		Baked	500	3	0.10 (Helium)	60
13	Mo_{13}		Baked	500	3	0.50 (Helium)	60
14	Mo_{14}		Baked	500	3	1.00 (Helium)	60
15	Mo_{15}		Baked	500	3	2.00 (Helium)	60
16	Mo_{16}		Baked	500	4	0.05 (Helium)	60
17	Mo_{17}		Baked	500	4	0.10 (Helium)	60
18	Mo_{18}		Baked	500	4	0.50 (Helium)	60
19	Mo_{19}		Baked	500	4	1.00 (Helium)	60
20	Mo_{20}		Baked	500	4	2.00 (Helium)	60

Mo thin films fabricated at various deposition parameters as listed in table 3.1. These films were deposited in the cylindrical ablation chamber evacuated with diffusion pump, section 2.2, chapter 2.

3.1.1 Effect of oxygen contamination on Mo thin films

In order to study the effect of oxygen contamination onto the quality of thin films, two samples Mo_1 and Mo_2 were prepared at room temperature at a target-substrate distance (D_{ts}) of 2 cm. Both the samples were prepared in presence of Ar gas at a pressure of ~ 0.05 mbar and deposited for 30 minute. Mo_1 thin film was deposited without proper conditioning of the chamber. The SEM image of Mo_1 sample, figure 3.2(a), shows cracks on the surface and the corresponding EDX spectrum, as shown in figure 3.2(b), confirmed the presence of oxygen as an impurity. The cracks in the film

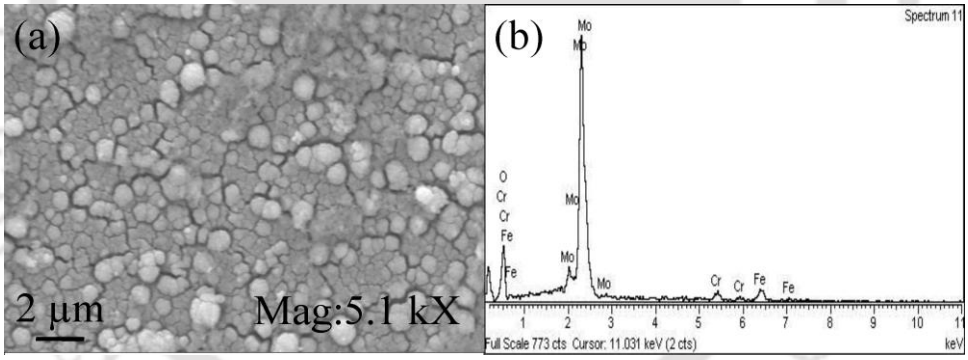

Figure 3.2. (a) SEM image and (b) EDX spectrum of Mo_1 sample (chamber not baked).

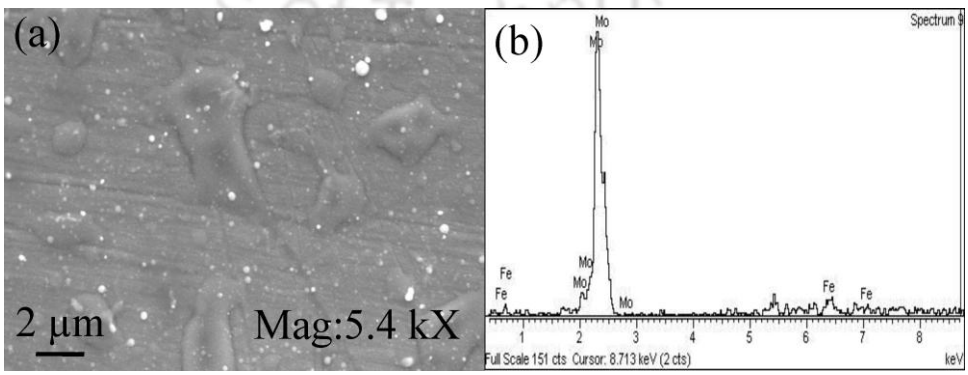

Figure 3.3. (a) SEM image and (b) EDX spectrum of Mo_2 sample (chamber baked).

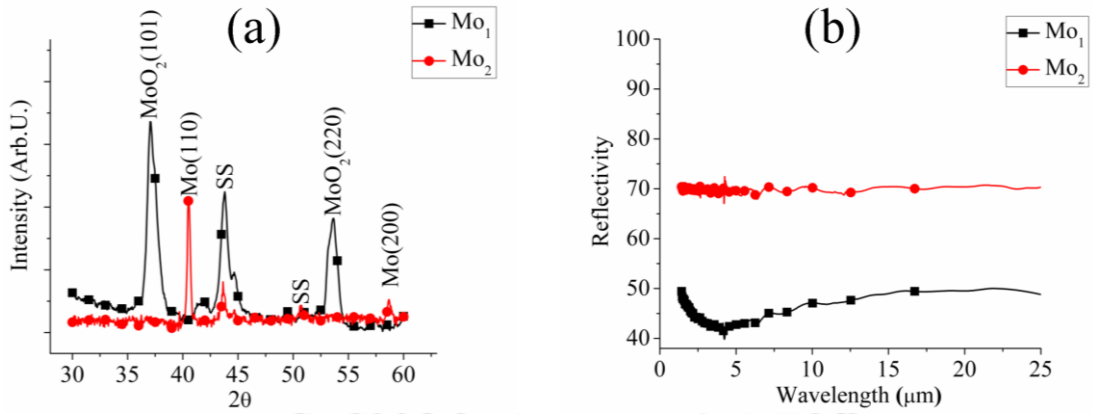

Figure 3.4. (a) XRD pattern and (b) diffuse FIR reflectivity with reference to aluminum standard mirror of Mo_1 and Mo_2 samples.

were developed due to the oxygen contamination. The adhesion of the film on substrate was poor and the film got detached from the substrate within a couple of weeks after deposition. To reduce oxygen contamination, the ablation chamber was conditioned by baking at 70-80 °C for ~ 14-15 hour while evacuation, prior to deposition. The second sample Mo_2 was deposited after conditioning of the chamber while keeping all other parameters same as that of Mo_1 sample. The SEM image and EDX spectrum of Mo_2 sample are shown in figure 3.3(a) and 3.3(b), respectively. In the SEM image of Mo_2 sample, the signature of any cracks was missing. The corresponding EDX spectrum confirmed the absence of oxygen impurity.

The XRD pattern of Mo_1 sample as shown in figure 3.4(a), clearly shows MoO_2(101) and MoO_2(220) peaks of molybdenum oxide. The XRD pattern of Mo_2 sample showed Mo(110) and Mo(200) peaks of pure Mo along with weak peaks of SS substrate. It was devoid of any molybdenum oxide peak.

The diffused FIR reflectivity of Mo_1 and Mo_2 samples with reference to aluminum standard mirror are shown in figure 3.4(b). The reflectivity of Mo_1 sample was ~ 40-48 % in the range of 2-20 μm which was less than that of the Mo_2 sample ~

70 %. The poor reflectivity of the Mo_1 sample was due to the oxygen contamination. Therefore, prior conditioning of the ablation chamber was required to suppress oxygen impurity contamination in the thin films during deposition. Henceforth, all the samples were prepared after this pre-conditioning of the ablation chamber.

3.1.2 Effect of laser fluence on the PLD thin films of Mo

One of the limitations of PLD technique for fabrication of metallic thin films is the formation of liquid droplets at high laser fluence. The laser fluence can be controlled by controlling focusing spot of the laser beam onto the target. In order to study the effect of laser fluence two samples, Mo_3 and Mo_4 were deposited under tight and loose focused condition of the laser beam, under vacuum (~ 10^{-5} mbar) for deposition time of ~ 60 minute. These samples were deposited after sufficient baking of the chamber in order to avoid the oxygen contamination. The focal spot onto the target for both samples are shown in figures 3.5(a) and 3.5(b), respectively. For Mo_3 sample the average diameter of ~ 396 µm corresponding to the laser fluence ~ 57 J/cm^2. The SEM image of Mo_3 sample, shown in figure 3.6(a), confirmed the formation of liquid droplets. The EDX spectrum of these droplets as shown in 3.6(b),

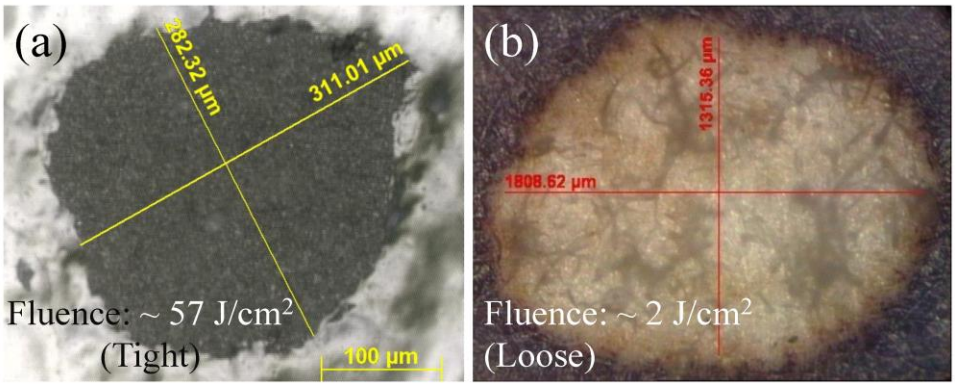

Figure 3.5. Single shot laser burn spot sizes (a) tightly focus condition and (b) loosely focused condition.

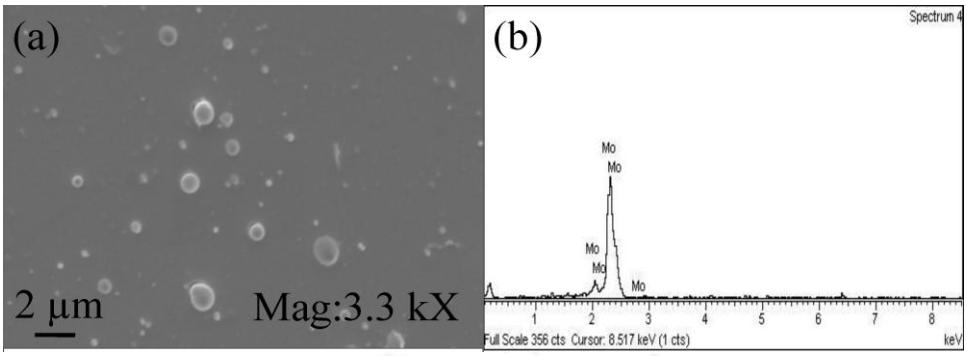

Figure 3.6. (a) SEM image and (b) EDX spectrum of Mo_3 sample (tightly focused).

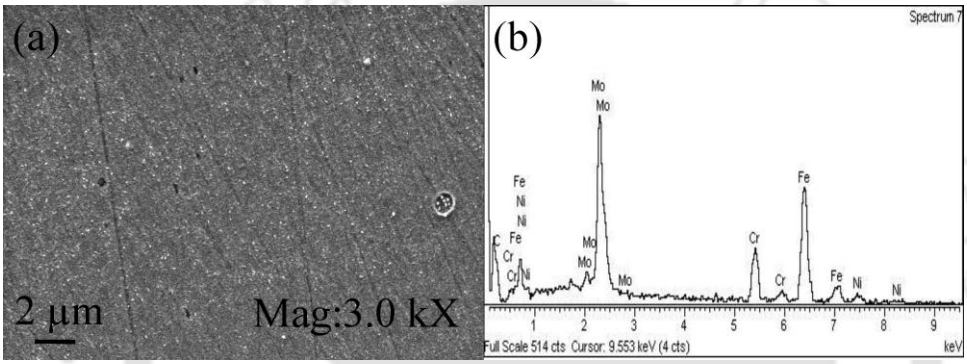

Figure 3.7. (a) SEM image and (b) EDX spectrum of Mo_4 sample (loosely focused).

confirmed that its constituent element was Mo only. The formation of liquid droplet on the film surface was due to very high laser fluence because of the tight focusing of laser beam onto the metal target. Such high laser fluence resulted into the ejection of target material in the form of flakes or droplets. These flakes or droplets propagated and deposited onto the film surface. If the ejected material from the target is of high energy it may get scattered from the film surface by creating craters on the surface. The formation of liquid droplets and hence, micro-structure on the film surface was avoided by reducing the laser fluence onto the Mo target. This was achieved by loosely focusing the laser beam onto the target for deposition of the sample Mo_4. The focal spot on the target for this sample is shown in figure 3.5(b), having major and minor axis diameters ~ 1808 µm and 1315 µm. This corresponded to laser fluence of

~ 2 J/cm^2. The SEM image of Mo_4 sample deposited under loosely focused condition of the laser beam is shown figure 3.7(a). It showed smooth surface morphology free from deposition of any liquid droplets. The EDX spectrum of Mo_4, shown in figure 3.7(b) exhibit Mo as major elements along with the appearance of Fe, Cr and Ni, the constituent elements of SS substrate. This was due to its lower thickness at lower laser fluence.

The diffuse FIR reflectivity of the Mo_3 and Mo_4 samples with reference to aluminum standard mirror are shown in figure 3.8. It was observed that the film deposited under tightly focused condition of laser beam, sample Mo_3 showed less reflectivity, ~ 15-45 % in the range of 2-20 μm than that of the film deposited under loosely focused condition of the laser beam, ~ 60-70 % in which the surface was devoid of micro structures. This showed that in order to obtain highly reflecting surface, the laser fluence should be kept low (by loosely focusing the laser beam onto the target). The rest of the Mo samples were prepared at this low fluence of ~ 2 J/cm^2 by keeping the focal spot of that of figure 3.5(b).

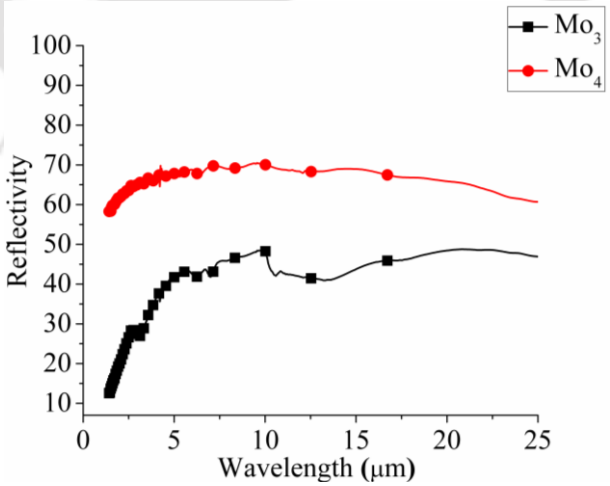

Figure 3.8. Diffuse FIR reflectivity with reference to aluminum standard mirror of Mo_3 and Mo_4 samples.

3.1.3 Effect of substrate temperature on Mo thin films

Irrespective of deposition technique used, the quality of thin films depends on the temperature of the substrate. To study the effect of substrate temperature on the quality of thin films, two samples Mo_5 and Mo_6 were deposited at room temperature and 500 °C of the substrate, respectively again under vacuum (~ 10^{-5} mbar). Both the samples were deposited for ~ 120 minute. The XRD patterns of these samples are shown in figure 3.9(a). The sample Mo_5 showed a broad XRD peak with Full Width at Half Maximum (FWHM) ~ 1.2° while that of Mo_6 sample showed prominent XRD peak of Mo(110) plane with FWHM ~ 0.7°. This confirmed that the crystallinity of Mo_6 sample was better than that of Mo_5 sample.[163] A rough estimation of the crystalline phase purity was calculated by taking the ratio of Mo(110) XRD peak intensity to the SS substrate XRD peak intensity of the same XRD spectrum. It was found to be ~ 0.9 for Mo_5 and 1.7 for Mo_6 sample.

The diffuse FIR reflectivity of both these samples with reference to aluminum standard mirror is shown in the figure 3.9(b). It was observed Mo_5 sample showed the reflectivity ~ 40-50 % in FIR spectral region, whereas the Mo_6 sample deposited at

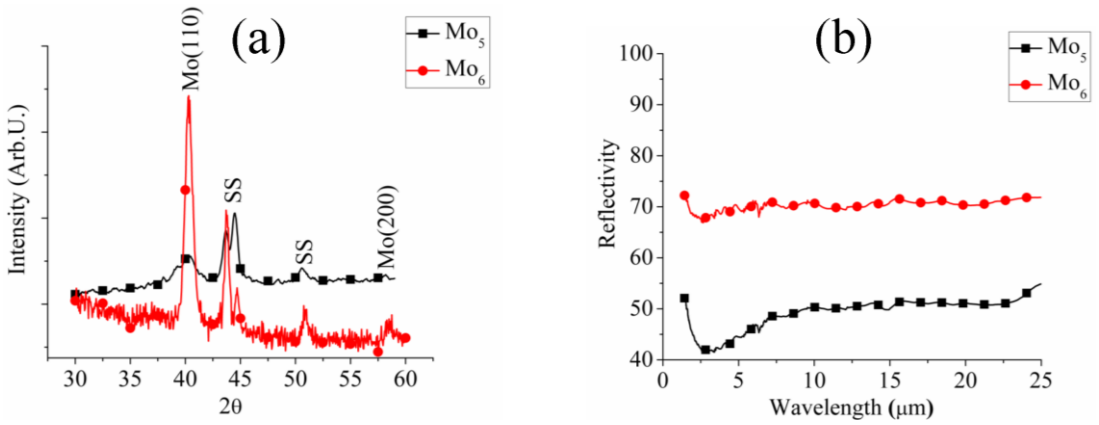

Figure 3.9. (a) XRD pattern and (b) diffuse FIR reflectivity with reference to aluminum standard mirror of Mo_5 and Mo_6 samples.

500 °C, showed improved reflectivity ~ 70 %.

3.1.4 Effect of target-substrate distance on Mo thin films

In order to study the effect of target-substrate distance (D_{ts}) on the quality of Mo thin film, the samples Mo_7-Mo_{10} were deposited at D_{ts}: 2 to 5 cm, as listed in table 3.1. All the samples were deposited at ~ 500 °C substrate temperature in a base pressure of ~ 10^{-5} mbar. The samples were deposited for a duration of ~ 180 minute.

The XRD pattern of Mo_7-Mo_{10} samples and polished bulk Mo target is shown in figure 3.10. All the samples showed the SS substrate peaks. The Mo_7 sample did not show any prominent crystal orientation of Mo XRD peak. The Mo_8, Mo_9, and Mo_{10} samples showed prominent XRD peak of Mo(110) plane along with weak XRD peak of Mo(200) plane. The enlarge view of the Mo(110) XRD peak is shown in figure 3.10(b). The FWHM of these samples are listed in table 3.2. The FWHM decreased with the increase of target-substrate distance. It was ~ 1.4° for Mo_8 and 0.7° for that of Mo_{10} sample. Measured FWHM of polished bulk Mo target was ~ 0.2°. The broadening of XRD peak in the thin film samples was due to the cumulative

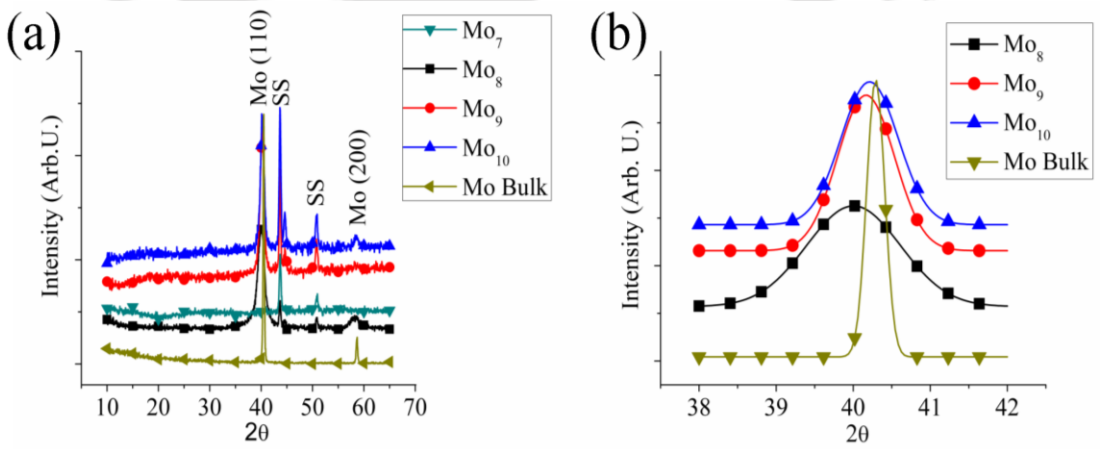

Figure 3.10. XRD pattern of (a) Mo_7-Mo_{10} samples and bulk Mo target and (b) enlarge view of Mo(110) peak corresponding to figure 3.10(a).

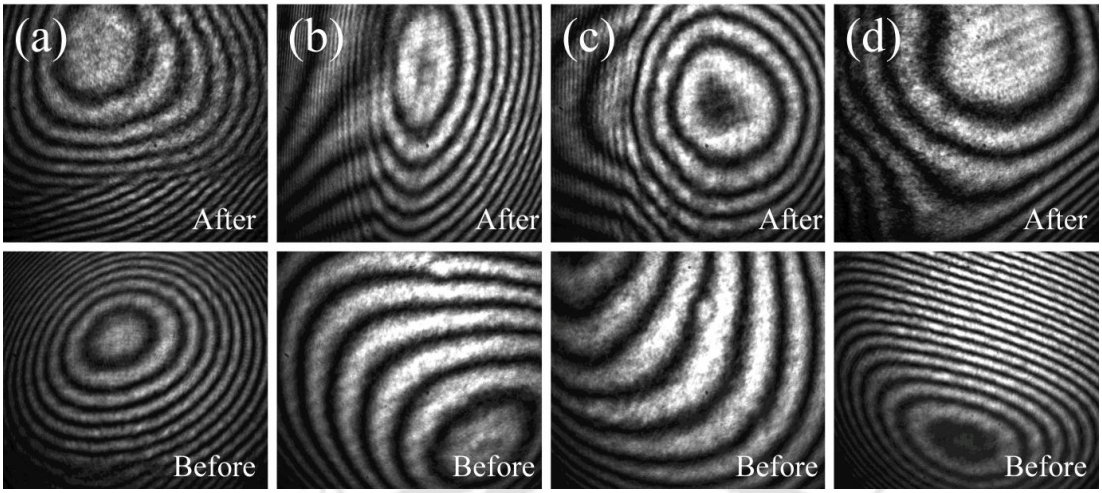

Figure 3.11. Interference pattern of (a) Mo_7, (b) Mo_8, (c) Mo_9 and (d) Mo_{10} substrate (Before) and films (After).

effect of stress present in the film, formation of nano/micro structures and partial amorphous nature of the film.[163] The decrease in FWHM with increase of target-substrate distance was due to cumulative effect of the lowering of stress present in the film and the decrease in grain size of the films with the increase of target-substrate distance. The kinetic energy of the laser ablated species in the plasma plume decreased with the increase of target-substrate distance. Therefore, laser ablated species arrived at the substrate with low kinetic energy at large target-substrate distance and hence, reduced the stress in the film.

The interference patterns of Mo_7-Mo_{10} samples (after deposition) recorded with Michelson interferometer, figure 2.5(a) and corresponding SS substrates (before deposition) are shown in figures 3.11(a)-(d), respectively. The radius of curvature (equation 2.1) and fringe visibility (equation 2.3) of these samples were measured from interference patterns and listed in table 3.2. The curved fringes were due to the curvature present in the substrate. The marginal changes in radius of curvature of the

Mo thin films compared to corresponding substrate confirmed that curvature was due to the built-in curvature present in the substrate. The curved interference pattern confirmed the presence of stress in the Mo_7-Mo_{10} thin film samples which resulted in the broadening of Mo(110) XRD peak compared to that of bulk target. The distinct interference pattern of the thin films confirmed that Mo thin films possessed mirror-like quality. The fringe visibility of all these films, listed in table 3.2, showed that the fringe visibility of the thin films increased with the target-substrate distance. It was due to the improvement of surface uniformity of the films with the increase of target-substrate distance. The fringe visibility of Mo_{10} sample was maximum, ~ 0.8.

The SEM image of Mo_7-Mo_{10} thin films samples deposited at D_{ts}: 2, 3, 4 and 5 cm on polished SS substrate are shown in figure 3.12(a)-(d), respectively. The corresponding EDX spectrum of these samples is shown in figure 3.13(a)-(d), respectively. Apart from Mo_7, the SEM images of all the samples confirmed the

Table 3.2. Sample codes, target-substrate distance (D_{ts}), FWHM of Mo (110) peak, radius of curvature (r), average grain size, average RMS surface roughness (σ), reflectivity (% R) with reference to aluminum standard mirror and fringe visibility (V).

Sample Code	FWHM of Mo(110)	r (m)		Grain size (μm)	σ (nm)	% R		V
		before	after			at λ = 20 μm	at λ = 800 nm	
Mo_7	No peak	4.6	4.7	1.8	49	91	54	0.6
Mo_8	1.4°	3.5	3.0	1.3	21	93	67	0.7
Mo_9	0.8°	5.2	5.1	0.7	17	94	67	0.7
Mo_{10}	0.7°	5.4	5.6	0.5	9	95	69	0.8
Mo Bulk	0.2°	---			---	95	73	---
SS substrate	---	---			---	93	79	0.8

smooth surface morphology of Mo_8-Mo_{10} samples. The average grain size was calculated from the SEM images and listed in table 3.2. Mo_7 sample showed large grains and microstructure formation on its surface, figure 3.12(a). The average grain size for Mo_7 sample was ~ 1.8 µm. This particular film was deposited at D_{ts}: 2 cm. The average grain size of Mo_{10} sample, deposited at D_{ts}: 5 cm was ~ 0.5 µm. It was observed that with the increase of target-substrate distance, the grain size decreased. It was due to the fragmentation of larger liquid droplet, ejected from the target, into smaller droplets before deposition onto the substrate at larger target-substrate distances. The EDX spectrum of Mo_7-Mo_{10} samples confirmed the presence of Mo and absence of any constituent elements (Fe, Cr) of the substrate as well as all contaminated impurities: carbon, oxygen, etc. The EDX spectrum of Mo thin film deposited at D_{ts}: 6 cm showed constituent elements of the substrate along with Mo.

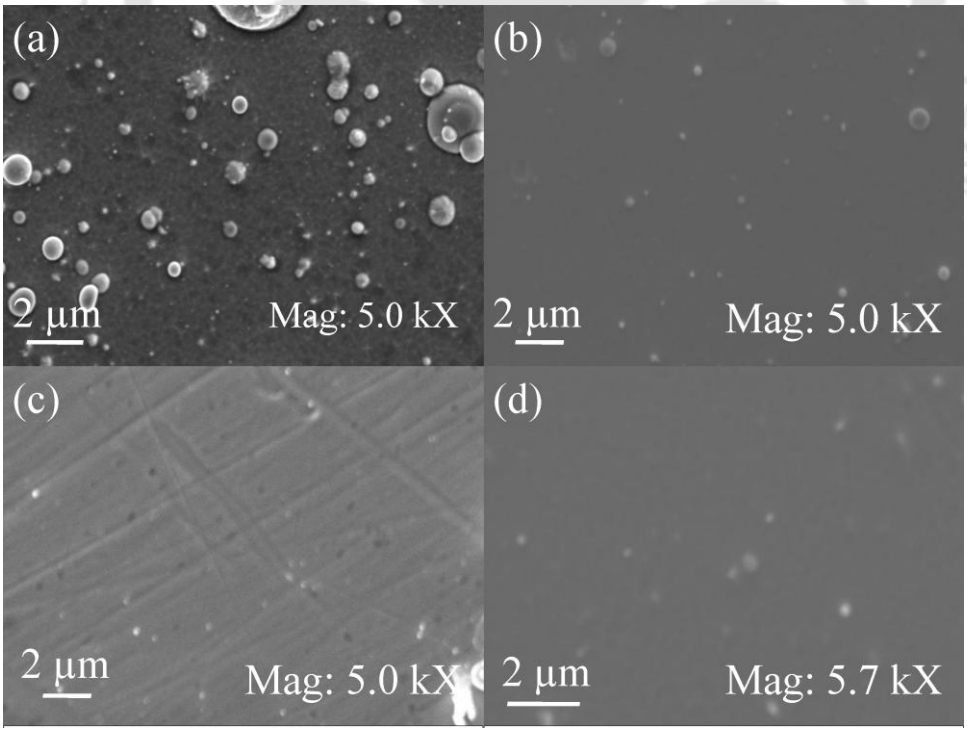

Figure 3.12. SEM image of (a) Mo_7, (b) Mo_8, (c) Mo_9 and (d) Mo_{10} samples.

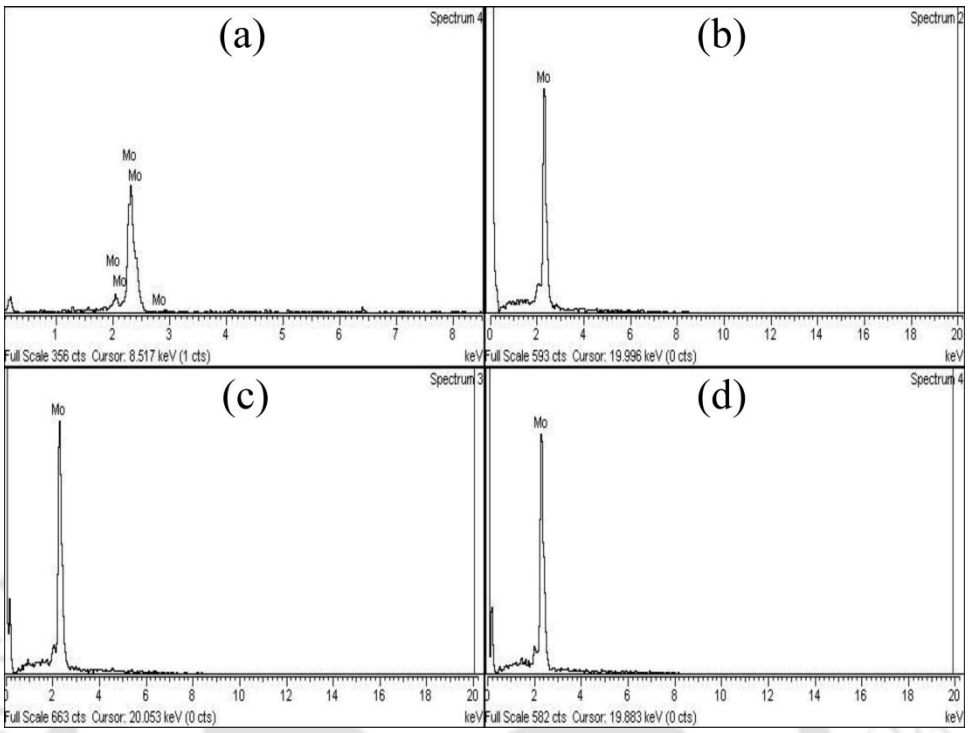

Figure 3.13. EDX spectrum of (a) Mo_7, (b) Mo_8, (c) Mo_9 and (d) Mo_{10} samples.

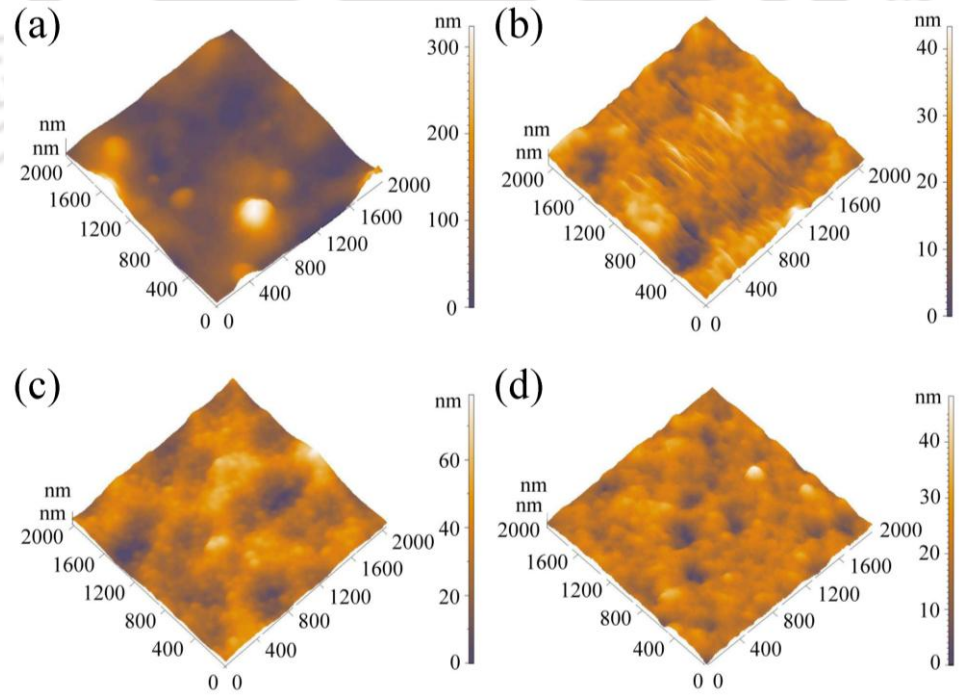

Figure 3.14. AFM image of (a) Mo_7, (b) Mo_8, (c) Mo_9 and (d) Mo_{10} samples.

Beyond this target-substrate distance, Mo could not be detected, as the plasma density falls down near exponentially with the increase of target-substrate distance.[131] Therefore, the thickness of Mo thin film was too low at $D_{ts} \geq 6$ cm and beyond the detection limit of the probing electron of EDX.

The AFM images of Mo_7-Mo_{10} samples are shown in figure 3.14(a)-(d). The RMS surface roughness (σ) of the corresponding films, averaged over three different scan areas of size 2 μm × 2 μm, are listed in table 3.2. The Mo_7 sample showed maximum RMS surface roughness, ~ 49 nm while that of Mo_{10} showed minimum RMS surface roughness ~ 9 nm. The Mo plasma plume arriving to the substrate was more uniformly distributed at larger target-substrate distance and hence, the RMS surface roughness was reduced.

The specular FIR reflectivity with reference to aluminum standard mirror of Mo_7-Mo_{10} samples, polished bulk Mo target and SS substrate are shown in figure 3.15(a), and that of UV-visible reflectivity of these samples are shown in figure 3.15(b). The reflectivity with reference to aluminum standard mirror at wavelength of 20 μm and 800 nm are listed in the table 3.2. The reflectivity of Mo_8 and Mo_9 samples

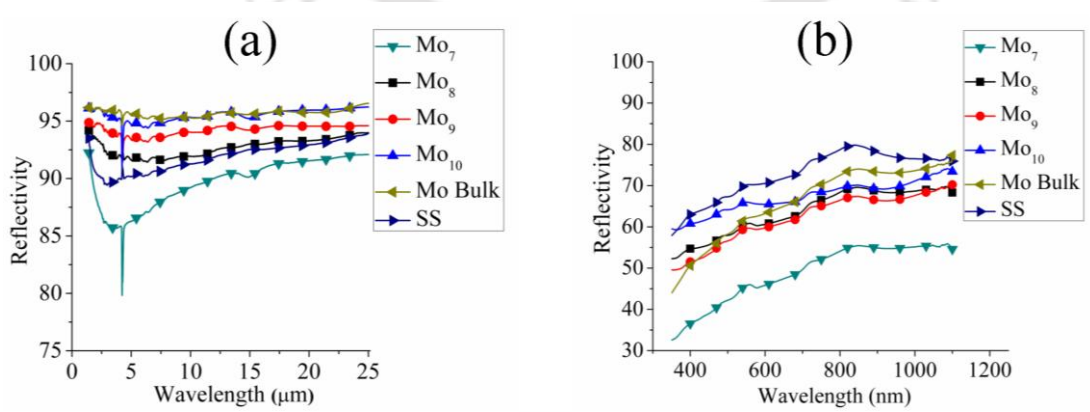

Figure 3.15. Specular reflectivity with reference to aluminum standard mirror of Mo_7-Mo_{10} samples (a) FIR range and (b) UV-visible range.

approached to that of the polished SS substrate and polished bulk Mo target. The Mo_{10} sample showed maximum reflectivity, ~ 95 % at wavelength of 20 µm and ~ 69 % at 800 nm while that of polished bulk Mo target showed ~ 95 % and 73 %, respectively. The Mo_7 sample showed minimum reflectivity ~ 91 % at wavelength of 20 µm and ~ 54 % at 800 nm. The relatively low reflectivity of Mo_7 can be attributed to its poor surface quality. The reflectivity of the samples increased with the increase of target-substrate distance. It was due to reduction into the RMS surface roughness with the increase of target-substrate distance, confirmed from SEM and AFM image analysis. Smooth surface devoid of micro structures with low RMS surface roughness is the key factor for high mirror reflectivity.[164,165] The sharp dip in specular reflectivity at wavelength of 4.258 µm was due to the substrate only as SS substrate has strong absorption around this wavelength.

3.1.5 Effect of He ambient gas pressure on Mo thin films

In order to increase the deposition rate and hence, thickness of the film, the laser induced Mo plasma was confined by using ambient He inert gas. To study the effect of ambient gas pressure onto the quality of thin film, two sets of samples were prepared by varying He gas pressure from ~ 0.05 mbar to 2.00 mbar. The detail deposition parameters of these samples are listed in the table 3.1. The first set of sample Mo_{11}-Mo_{15} was prepared at D_{ts}: 3 cm and the second set of sample Mo_{16}-Mo_{20} was prepared at D_{ts}: 4 cm.

All the samples were prepared by placing a mask to cover a part of the substrate. This gave a film-substrate step for the measurement of thickness. The thickness of these partially deposited samples was measured by Stylus surface profilometer and listed in the table 3.3. The variation of thickness with He ambient

gas pressure for samples Mo_{11}-Mo_{15} and Mo_{16}-Mo_{20} are shown in the figure 3.16(a) and 3.16(b), respectively. It was observed that the thickness of the Mo thin films was

Table 3.3. Sample codes, target-substrate distance (D_{ts}), He ambient pressure (B_p), thickness (t), FWHM of Mo (110) peak, reflectivity (% R) with reference to aluminum standard mirror.

Sample Code	D_{ts} (cm)	B_p (mbar)	t (nm)	FWHM of Mo(110)	% R	
					at λ = 20 μm	at λ = 800 nm
Mo_{11}	3	0.05	296	0.6º	96	41
Mo_{12}	3	0.10	308	0.6º	98	49
Mo_{13}	3	0.50	386	0.6º	98	82
Mo_{14}	3	1.00	252	0.7º	97	85
Mo_{15}	3	2.00	242	No peak	95	71
Mo_{16}	4	0.05	229	0.7º	93	60
Mo_{17}	4	0.10	231	0.7º	95	68
Mo_{18}	4	0.50	322	0.5º	98	87
Mo_{19}	4	1.00	265	1.2º	98	80
Mo_{20}	4	2.00	240	No peak	88	67

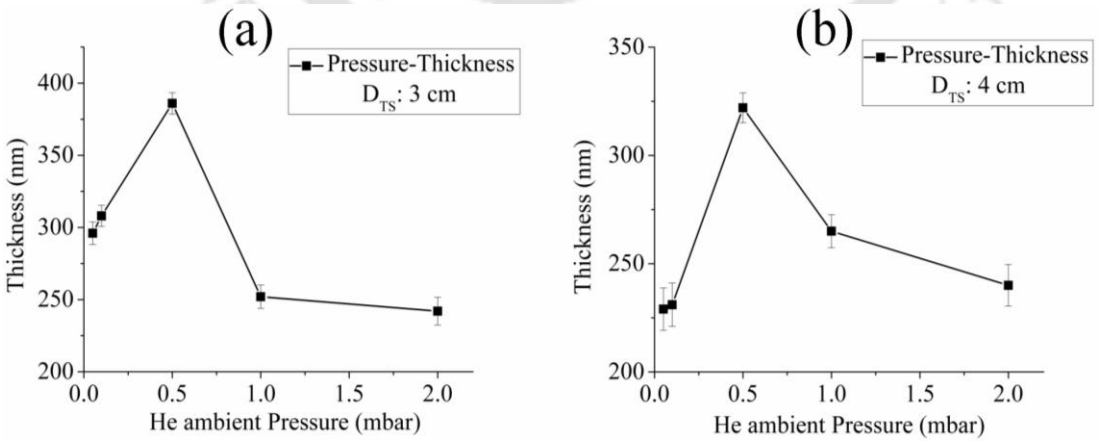

Figure 3.16. Thickness variation with ambient He gas pressure (a) at D_{ts}: 3 cm for samples Mo_{11}-Mo_{15} and (b) at D_{ts}: 4 cm Mo_{16}-Mo_{20} samples.

increased initially up to ~ 0.50 mbar He gas pressure and then gradually fell down with further increase of gas pressure up to ~ 2.00 mbar. It was due to the confinement of the laser induced plasma with the increase of ambient gas pressure. Initially, when the ambient gas pressure was low, the plasma confinement was taking place within a hemispherical sphere of radius comparable to that of the target-substrate distance. Therefore, the plasma density increased within the confined region which increased the deposition rate and hence, thickness of the film. With the further increase of ambient gas pressure, beyond 0.50 mbar, the plasma was confined to a smaller region, than that of the target-substrate distance. Thus, there was a significant decrease in the laser ablated species reaching towards substrate which decreased the deposition rate and hence, thickness of the film. The maximum thickness, ~ 386 nm was observed for Mo_{13} sample which was deposited at D_{ts}: 3 cm under ~ 0.50 mbar ambient He gas pressure. The deposition rate of this sample was ~ 6.4 nm/minute. The thickness of Mo_{18} sample under same ambient gas pressure at D_{ts}: 4 cm was ~ 322 nm, which was slightly lower than that of Mo_{13} sample. The deposition rate for Mo_{18} sample was ~ 5.3 nm/minute.

The XRD pattern of Mo_{11}-Mo_{15} and Mo_{16}-Mo_{20} samples are shown in figures 3.17 and 3.18, respectively. The prominent XRD peak of Mo(110) plane along with weak peak of Mo(200) plane and two SS substrate peaks were observed in the XRD pattern of Mo_{11}-Mo_{14} and Mo_{16}-Mo_{19} samples. The FWHM of Mo(110) XRD peak for Mo_{11}-Mo_{14} and Mo_{16}-Mo_{19} samples are listed in the table 3.3. The FWHM of Mo(110) XRD peaks of the samples Mo_{13}, deposited under ~ 0.50 mbar He ambient gas pressure was ~ 0.7° which is comparable to that of the Mo thin film deposited by sputtering technique.[166] The XRD pattern of Mo_{15} and Mo_{20} samples showed the XRD

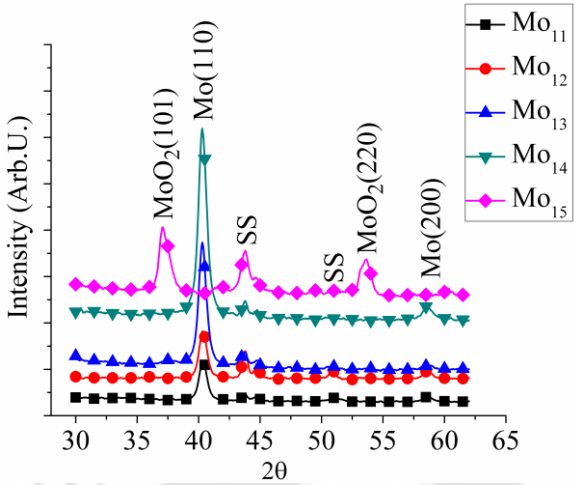

Figure 3.17. XRD pattern of Mo_{11}-Mo_{15} samples

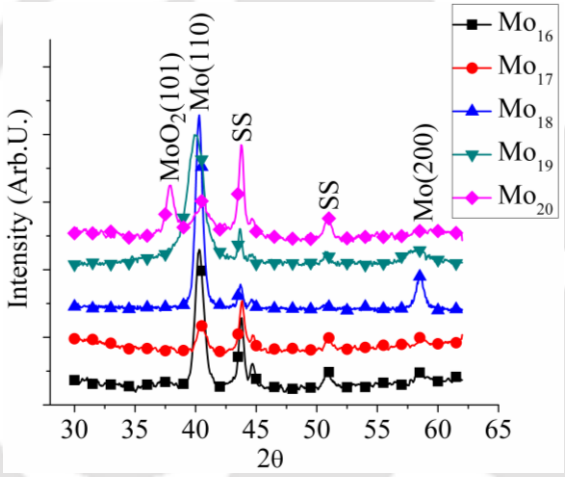

Figure 3.18. XRD pattern of Mo_{16}-Mo_{20} samples.

peaks of MoO_2(101) and MoO_2(220) plane and Mo peaks were absent in both these patterns. This was due to the oxygen impurity contamination during deposition which became prominent at relatively higher pressure of ~ 2.00 mbar.

The specular FIR reflectivity with reference to aluminum standard mirror for both the two sets of PLD Mo thin film samples, Mo_{11}-Mo_{15} and Mo_{16}-Mo_{20} are shown in the figures 3.19(a) and 3.19(b), respectively. The reflectivity at wavelength of 20 μm for all these ten samples is listed in the table 3.3. The film deposited at ~ 0.50

mbar ambient gas pressure, showed maximum reflectivity ~ 98 % at 20 µm, for both D_{ts}: 3 cm and 4 cm. It was observed that the film deposited at ~ 0.05 mbar ambient gas pressure, Mo_{11} and Mo_{16} samples, had poor reflectivity. The UV-visible reflectivity of all the samples deposited in presence of He ambient gas is shown in the figures 3.20(a) and 3.20(b), respectively. The maximum recorded specular reflectivity at wavelength of 800 nm, was ~ 84 % for Mo_{13}-Mo_{14} samples and ~ 87 % for Mo_{18} sample. Due to oxygen contamination, the reflectivity of samples Mo_{15} and Mo_{20} was poor.

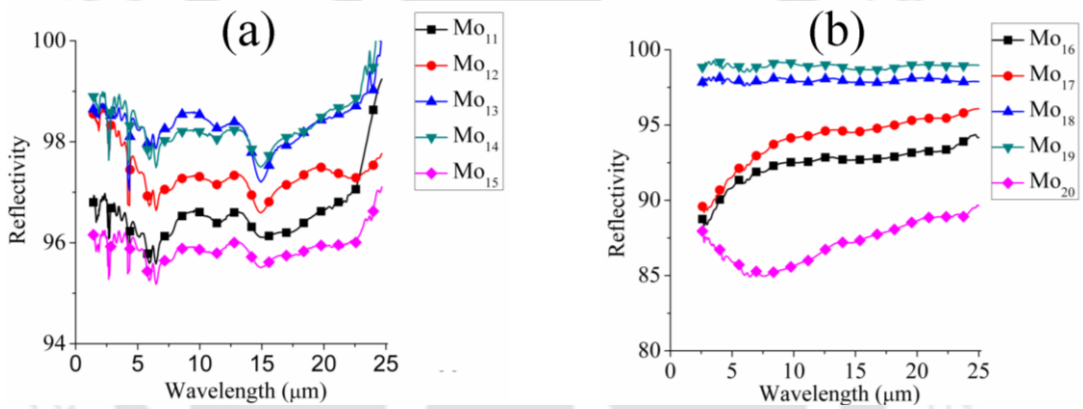

Figure 3.19. Specular FIR reflectivity with reference to aluminum standard mirror of (a) Mo_{11}-Mo_{15} and (b) Mo_{16}-Mo_{20} samples.

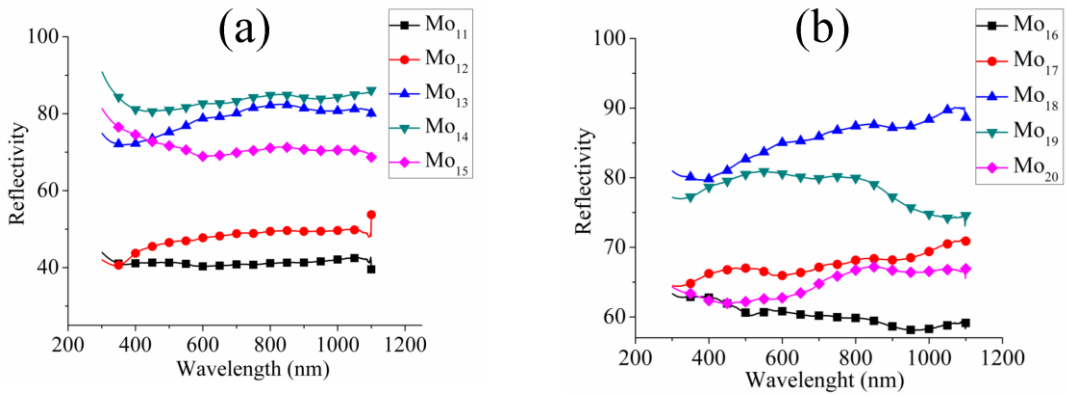

Figure 3.20. Specular UV-visible reflectivity with reference to aluminum standard mirror of (a) Mo_{11}-Mo_{15} and (b) Mo_{16}-Mo_{20} samples.

3.2 Characterization of pulsed laser deposited thin films of W

Tungsten (W) is preferred choice of material for fabrication of FM over Mo. Mirror-like thin films of W were deposited via PLD technique at various deposition parameters. These films were deposited in the cylindrical ablation chamber, figure 2.3, evacuated with diffusion pump. Details of various deposition parameters along with sample codes are listed in table 3.4. In totality, thirteen W thin film samples were deposited. The photographs of some of the W thin films are shown in figure 3.21. The effects of oxygen contamination, laser fluence, target-substrate distance, ambient gas

Table 3.4. Details of samples codes and deposition parameters of W thin film samples.

SL. No.	Sample Code	Focusing condition (laser fluence)	Ablation chamber condition	T_s (^oC)	D_{ts} (cm)	B_p (mbar)	T_d (minute)
1	W_1	Loose (~ 2 J/cm^2)	Not Baked	RT	3	10^{-5}	30
2	W_2		Baked	RT	3	10^{-5}	30
3	W_3	Tight (~ 57 J/cm^2)	Baked	RT	3	10^{-5}	120
4	W_4	Loose (~ 2 J/cm^2)	Baked	RT	3	10^{-5}	120
5	W_5		Baked	RT	3	10^{-5}	180
6	W_6		Baked	500	3	10^{-5}	180
7	W_7		Baked	RT	2	10^{-5}	180
8	W_8		Baked	RT	3	10^{-5}	180
9	W_9		Baked	RT	4	10^{-5}	180
10	W_{10}	Loose (~ 3.8 J/cm^2)	Baked	500	3	0.05 (He)	60
11	W_{11}		Baked	500	3	0.10 (He)	60
12	W_{12}		Baked	500	3	0.50 (He)	60
13	W_{13}		Baked	500	3	1.00 (He)	60

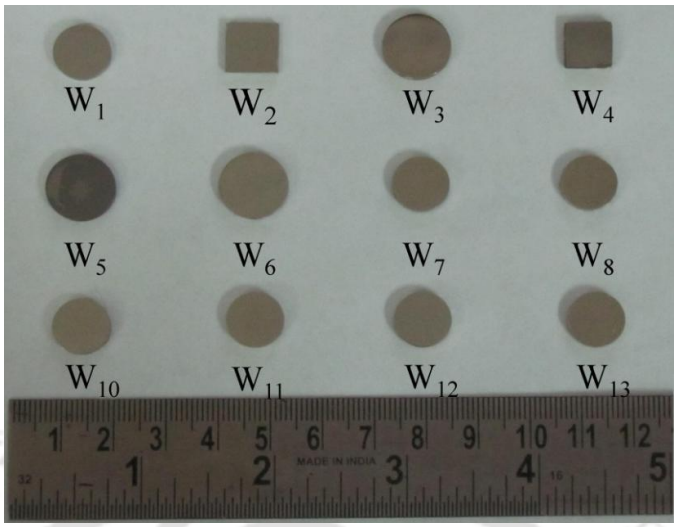

Figure 3.21. Photographs of W thin film samples.

pressure onto the quality of W thin film are presented in the following subsections.

3.2.1 Effect of oxygen contamination on W thin films

Similar to Mo thin films, PLD thin film of W, deposited without prior conditioning of the ablation chamber was contaminated with oxygen. For the comparison, SEM image and EDX spectrum of W_1 sample deposited without prior baking of the chamber and that of W_2 sample after conditioning of the chamber (baking at temperature ~ 70-80 °C for 14-15 hour while evacuation), are shown in figure 3.22(a)-(b) and figure 3.23(a)-(b), respectively. Both these samples were deposited at room temperature in a base pressure ~ 10^{-5} mbar keeping the target-substrate distance ~ 3 cm and deposition times of ~ 30 minute. The cracks in W_1 sample were clearly observed in its SEM image. It was due to the oxygen contamination of the film which was confirmed by its EDX spectrum as shown in figure 3.23(a), whereas the SEM image of W_2 sample, figure 3.22(b), showed smooth surface free from any cracks in the film. The EDX of W_2 sample, figure 3.23(b), was free from any traces of oxygen.

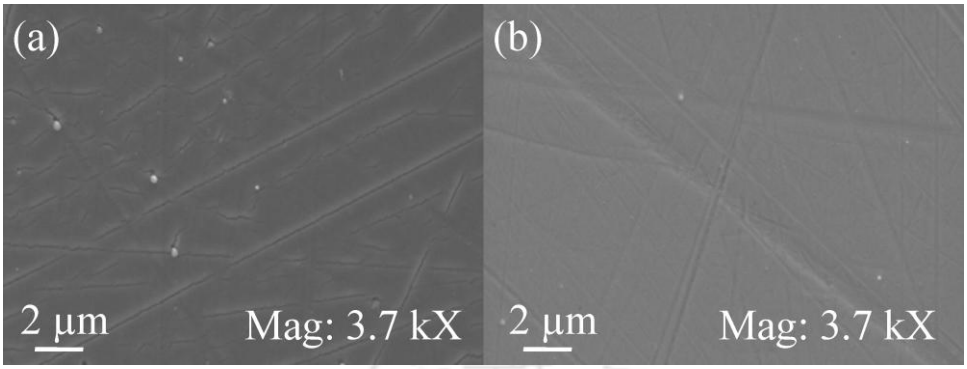

Figure 3.22. SEM image of (a) W_1 (Not baked) and (b) W_2 (baked) thin films.

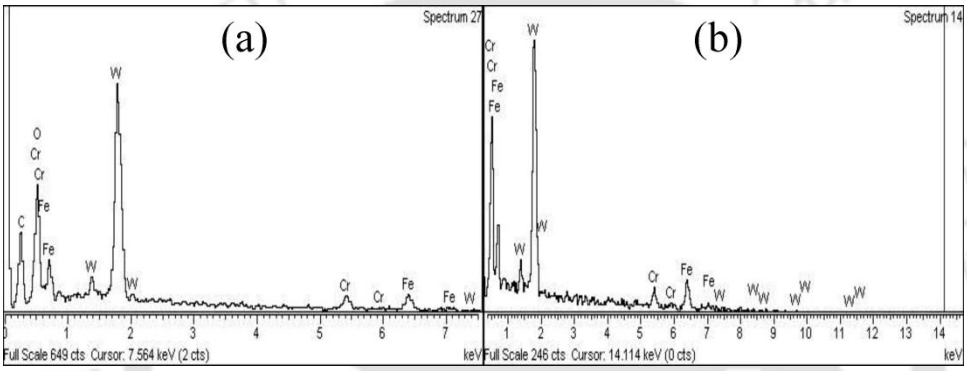

Figure 3.23. EDX spectrum of (a) W_1 (Not baked) and (b) W_2 (baked) samples.

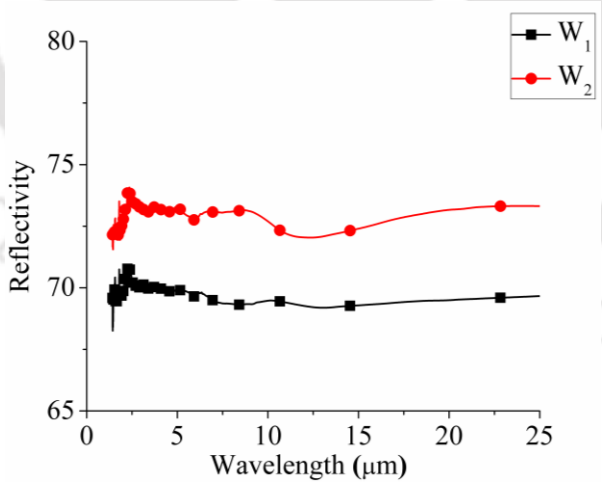

Figure 3.24. Diffuse FIR reflectivity with reference to aluminum standard mirror of W_1 and W_2 samples.

The diffuse FIR reflectivity with reference to aluminum standard mirror of W_1 and W_2 samples are shown in figure 3.24. It was observed that the reflectivity of W_1

sample (~ 69 % in the range of 2-20 μm) was less than that of W_2 sample (~ 72-74 % in the range of 2-20 μm). The low reflectivity of W_1 sample was due to oxygen contamination.

3.2.2 Effect of laser fluence on the PLD thin films of W

To study the effect of laser beam focusing condition and hence laser fluence, W_3 and W_4 samples were deposited by focusing the laser beam tightly and loosely onto the W target, respectively. The corresponding laser fluence was ~ 57 J/cm^2 and ~ 2 J/cm^2, respectively under base pressure of 10^{-5} mbar, deposited for 120 minute. The SEM image of W_3 sample, figure 3.25(a) clearly showed the deposition of liquid droplets on the substrate similar to that of Mo thin film, figure 3.6(a). The constituent element of these droplets was W only as confirmed in EDX spectrum, figure 3.26(a).

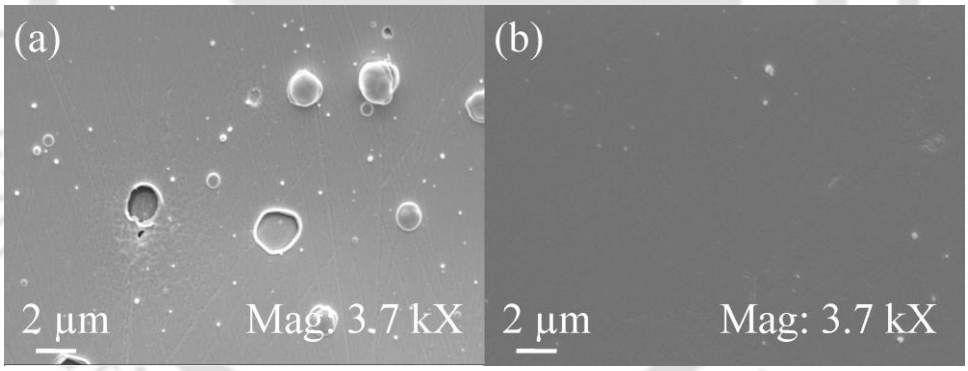

Figure 3.25. SEM image of (a) W_3 tightly and (b) W_4 loosely focused samples.

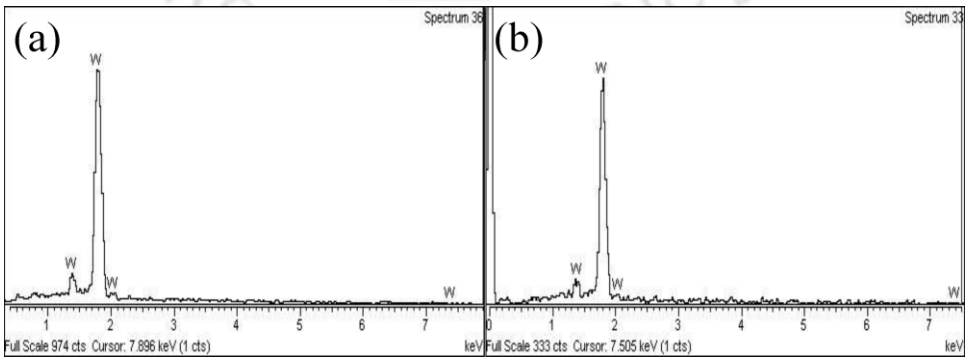

Figure 3.26. EDX spectrum of (a) W_3 and (b) W_4 samples.

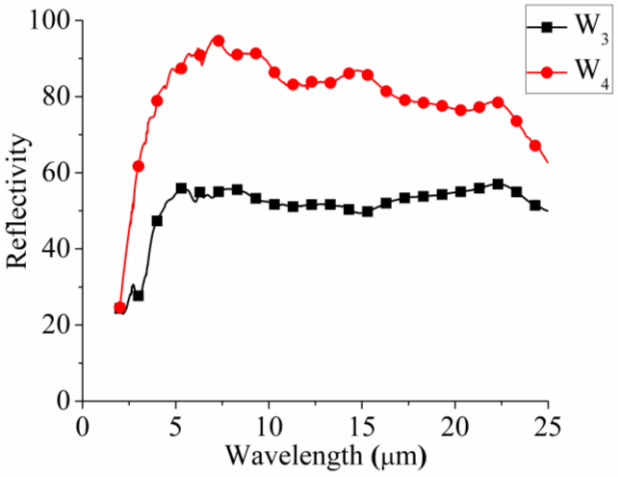

Figure 3.27. Diffuse FIR reflectivity of W_3 and W_4 samples with reference to aluminum standard mirror.

The surface of the sample W_4, deposited at a laser fluence ~ 2 J/cm^2 by loosely focusing the laser beam to a spot size having major and minor axis diameters ~ 1808 μm and 1315 μm, was very uniform and almost free from any microstructure, SEM image figure 3.25(b). The EDX spectra of both the samples, W_3 and W_4 shown in figure 3.26(a) and 3.26(b), respectively were free from oxygen.

The diffuse FIR reflectivity with reference to aluminum standard mirror of W_3 and W_4 samples is shown in figure 3.27. It was observed that the film deposited under tightly focused condition of the laser beam showed less reflectivity (~ 50 % in the range of 5-20 μm) than that of the film deposited under loosely focused condition (> 80 % in the range of 5-20 μm). This was due to the improved surface uniformity of the sample deposited under loosely focused condition of the laser beam.

3.2.3 Effect of substrate temperature on W thin films

To study the effect of substrate temperature on the quality of W thin film, W_5 and W_6 samples were deposited for a duration of ~ 180 minute at room temperature as well as 500 °C of the substrate under vacuum ~ 10^{-5} mbar. The SEM images of these

samples recorded after couple of weeks are shown in the figures 3.28(a) and 3.28(b), respectively. The SEM image of W_5 sample showed the signature of the film eruption from the substrate, whereas W_6 film remained intact even after couple of months as confirmed by the smooth surface of the later, figure 3.28(b). This confirmed that elevated substrate temperature helps in improving the film-substrate adhesivity. Substrate elements Fe, Cr, etc. were clearly observed in the EDX spectrum of W_5 sample, figure 3.29(a). It was due to the peeling of the film from substrate which allowed the EDX probing electron to reach the substrate and detected the constituent elements of SS substrate. The EDX spectrum of W_6 sample, figure 3.29(b) was observed to contain only W due to the smooth film surface, devoid of any eruption of the film from substrate.

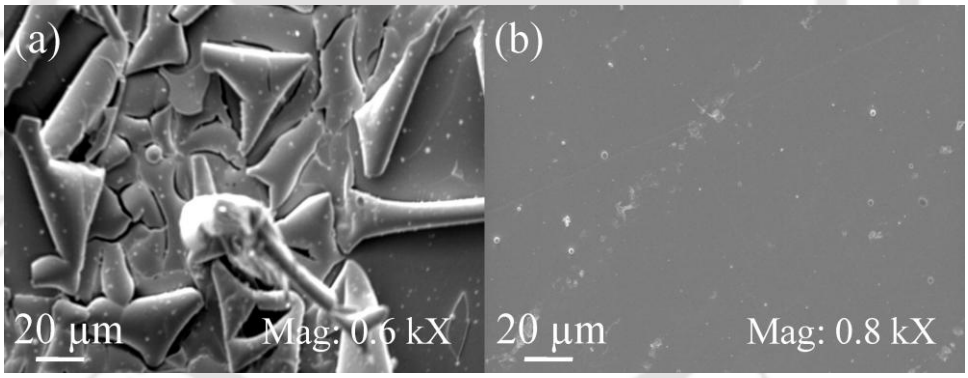

Figure 3.28. SEM image of (a) W_5 (room temperature) and (b) W_6 (500 °C) samples.

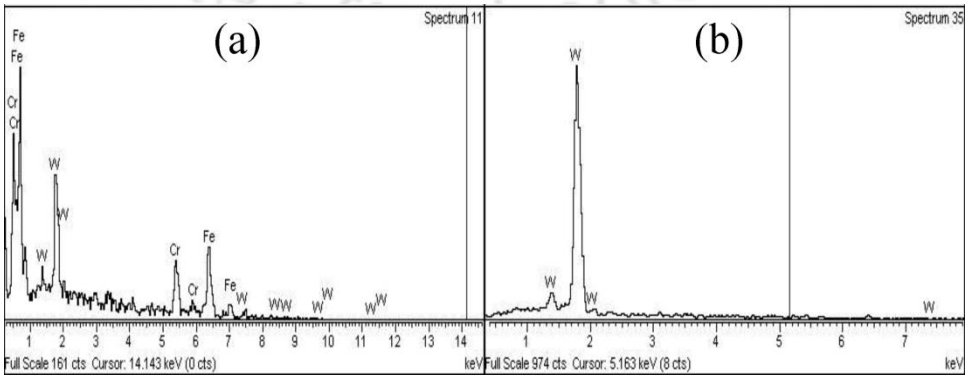

Figure 3.29. EDX spectrum of (a) W_5 and (b) W_6 samples.

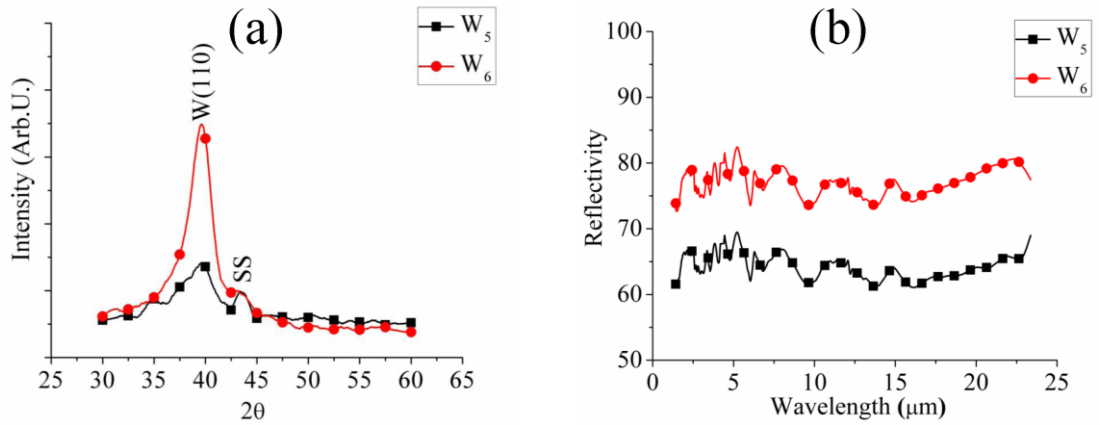

Figure 3.30. (a) XRD pattern and (b) diffuse FIR reflectivity with reference to aluminum standard mirror of W_5 and W_6 samples.

The XRD pattern of W_5 and W_6 samples is shown in figure 3.30(a). The XRD peak of W(110) plane observed in both W_5 and W_6 samples, with FWHM ~ 2.8° and 1.4°, respectively. Absence of any tungsten oxide peaks further confirmed in the XRD patterns of these samples. The phase purity of the W_5 and W_6 samples were ~ 1.4 and 3.4, respectively. The lower value of FWHM of W_6 sample reflects the improved crystallinity at elevated substrate temperature 500 °C.

The diffuse FIR reflectivity with reference to standard aluminum mirror of these films is shown in figure 3.30(b). It was observed that the overall reflectivity of W_6 sample was more than that of W_5 sample. The better FIR reflectivity of W_6 sample than that of W_5 sample was due to its uniform surface morphology as shown in figure 3.28(b) which was free from any smudging of the film from the substrate.

3.2.4 Effect of target-substrate distance on W thin films

To study the effect of target-substrate distance onto the quality of W thin films, W_7, W_8 and W_9 samples were deposited at D_{ts}: 2 cm, 3 cm and 4 cm, respectively under vacuum ~ 10^{-5} mbar. The detail deposition parameters of these

samples are listed in table 3.4.

The SEM image of W_7-W_9 samples are shown in figure 3.31(a)-(c), respectively. All these images are free from the developments of any cracks. Few large particulates were observed in the SEM image of the W_7 sample deposited at D_{ts}: 2 cm. This was due to the deposition of liquid droplets onto the substrate in the close proximity of the target. The average size of the particulates was around 1.5 μm for W_7 sample. The size of the particulates was reduced to few hundreds of nm with the increase of target-substrate distance. The EDX spectrum of W_7-W_9 samples are shown in figures 3.32(a)-(c), respectively. EDX spectrum of W_7 sample was free from any signature of substrate elements, but EDX spectrum of W_8 and W_9 sample clearly showed Fe peaks. This could be due to the higher thickness of W_7 sample which was

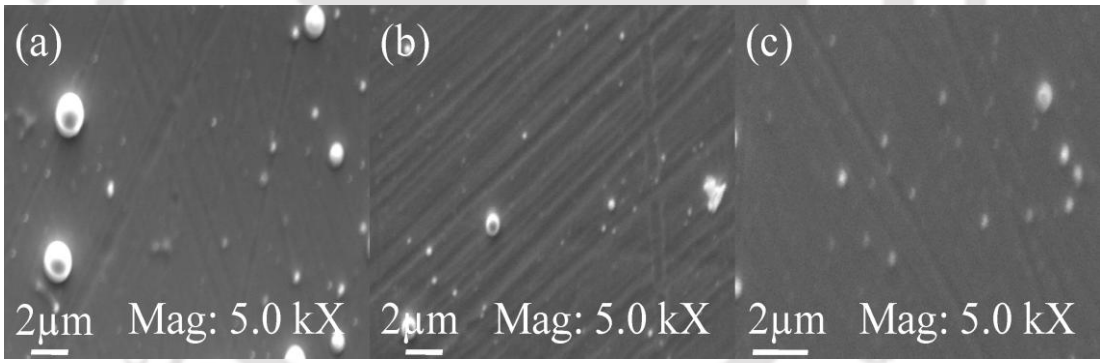

Figure 3.31. SEM image of (a) W_7, (b) W_8 and (c) W_9 samples.

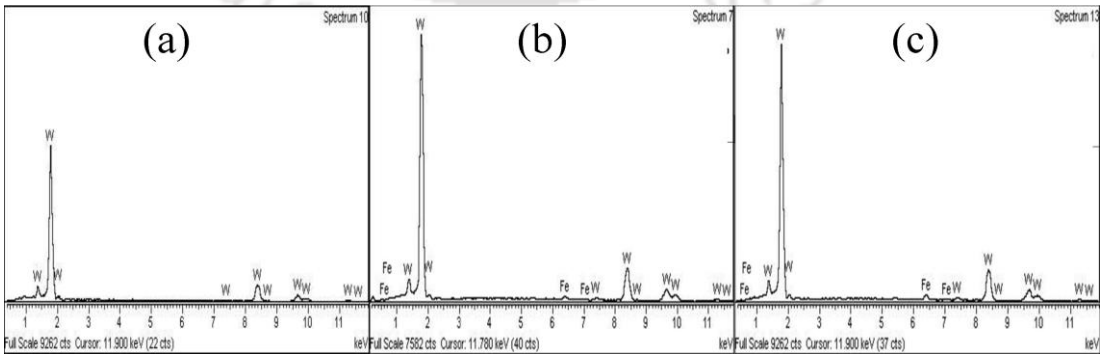

Figure 3.32. EDX spectrum of (a) W_7, (b) W_8 and (c) W_9 samples.

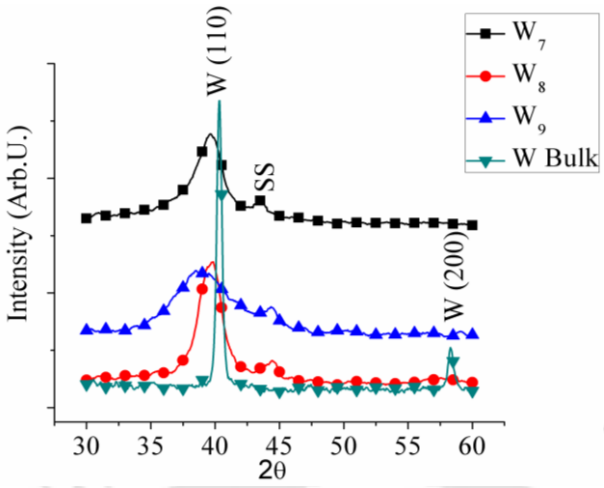

Figure 3.33. XRD pattern of W_7-W_9 films.

deposited at very low separation between target and substrate, whereas due to the plasma expansion, density of laser ablated species decreased as the distance from the target was increased and hence, the thickness of the W_8 and W_9 sample decreased.

The XRD pattern of W_7-W_9 samples are shown in figure 3.33. Prominent XRD peak W(110) plane of W_7-W_9 samples was confirmed in their XRD patterns. The XRD peak of W(200) plane which appeared in the XRD pattern of polished W target, was suppressed in the XRD patterns of W_7-W_9 thin film samples. Absence of tungsten oxide XRD peaks from the sample was in confirmation with EDX spectrum, figure 3.32, where oxygen peaks was missing for all the samples. The FWHM of W(110) XRD peak was ~ 2.7°, 1.9° and 5.7° for W_7, W_8 and W_9 samples, respectively as listed in table 3.5. This confirmed that W_8 sample was of better crystallinity than that of W_7 and W_9 samples.[163] The FWHM of this set of samples W_7-W_9, was larger than that of FWHM of bulk W target (~ 0.3°). This could be due to the stress present in W film.

The interference pattern recorded from the Michelson interferometer, figure

Table 3.5. FWHM of W(110) XRD peak, radius of curvature (r) and reflectivity (% R) with reference to aluminum standard mirror of W_7-W_9 samples.

Sample Code	FWHM of W(110)	r (m)	% R at λ = 20 μm
W_7	2.8°	5.1	68
W_8	1.9°	large	90
W_9	5.7°	2.2	87
SS	--	5.6 for W_7, 3.5 for W_9	91

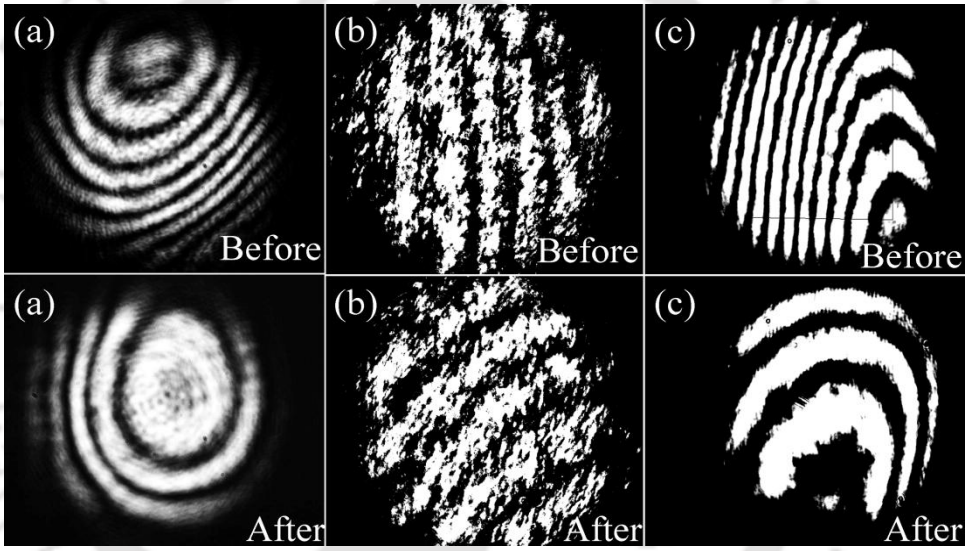

Figure 3.34. Interference patterns before and after deposition of (a) W_7, (b) W_8 and (c) W_9 samples.

2.5(a), for the bare polished substrate before and after deposition of W thin film, W_7-W_9 is shown in figure 3.34. The interference pattern of W_7 and W_9 samples showed circular fringes, whereas that of W_8 sample showed nearly straight fringe. Distinct and clear interference pattern confirmed the mirror-like quality of W thin film samples. The radius of curvature of the substrate and films measured from the radius of the circular interference patterns are listed in table 3.5. The marginal change in the radius

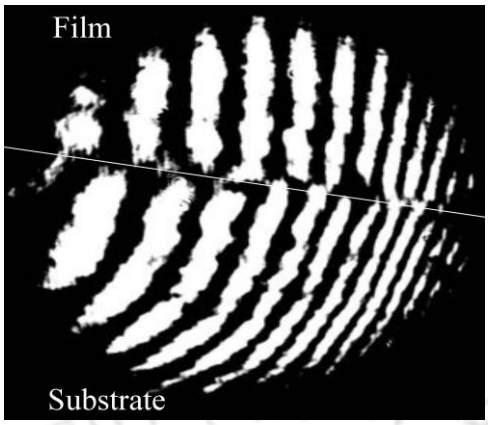

Figure 3.35. Interference pattern of W_9 sample (straight line represents substrate-film step).

of curvature of W_7 and W_9 substrate (before deposition) and corresponding films (after deposition) confirmed that the curvature in the films was due to the built-in curvature present in the corresponding substrate only. It was observed that with the increase of radius of curvature of the films, FWHM of W(110) XRD peak decreased. It was due to the lowering of stress present in the film with the increase of radius of curvature.[163]

The W_9 sample was deposited partially by placing a mask on substrate prior to deposition so as to form the substrate-film step. The interference fringe formed at substrate-film step is, shown in figure 3.35. The shift in interference fringe at the step was clearly visible. The thickness estimated from the fringe shift and fringe width was ~ 782 nm. The corresponding deposition rate of this sample was ~ 4.4 nm/minute.

The specular FIR reflectivity of W_7-W_9 samples is shown in figure 3.36. The reflectivity of the samples at wavelength of 20 μm with reference to standard aluminum mirror is listed in table 3.5. It was observed that the film deposited at D_{ts}: 2 cm, W_7, had lower reflectivity (~ 68 % at 20 μm) than the film deposited at D_{ts}: 3, W_8 sample (~ 90 % at 20 μm). The low reflectivity of W_7 was to due to its poor surface

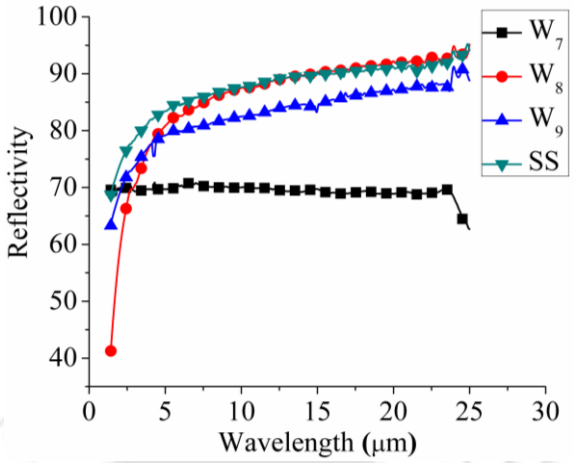

Figure 3.36. Specular FIR reflectivity with reference to aluminum standard mirror of W_7-W_9 samples.

quality having large micro structures, confirmed from its SEM image, figure 3.31(a).

3.2.5 Effect of He ambient gas pressure on W thin films

Finally, four more W thin film samples were deposited to investigate the effect of ambient He gas pressure onto the quality of W thin film. Thin film samples of W were deposited at He pressures ~ 0.05, 0.10, 0.50 and 1.00 mbar. The other parameters D_{ts}: 3 cm, laser fluence ~ 3.8 J/cm^2, substrate temperature of 500 °C, duration of deposition 60 minute, listed in table 3.4, were kept fixed.

The SEM image and EDX spectrum of W_{10}-W_{13} samples are shown in figures 3.37(a)-(d), respectively. The surface of all the samples W_{10}-W_{13} was uniform and free from cracks or any crater formation. The EDX spectrum of these samples showed the corresponding peaks of W only. The AFM image of W_{10}-W_{13} samples is shown in figures 3.38(a)-(d), respectively. The average RMS surface roughness of the samples is listed in table 3.6. The listed values were the average over three different scan areas of 2 μm × 2 μm of each sample. The maximum and minimum RMS surface roughness was ~ 20 nm and 8 nm for W_{10} and W_{13} sample, respectively. The number of collision

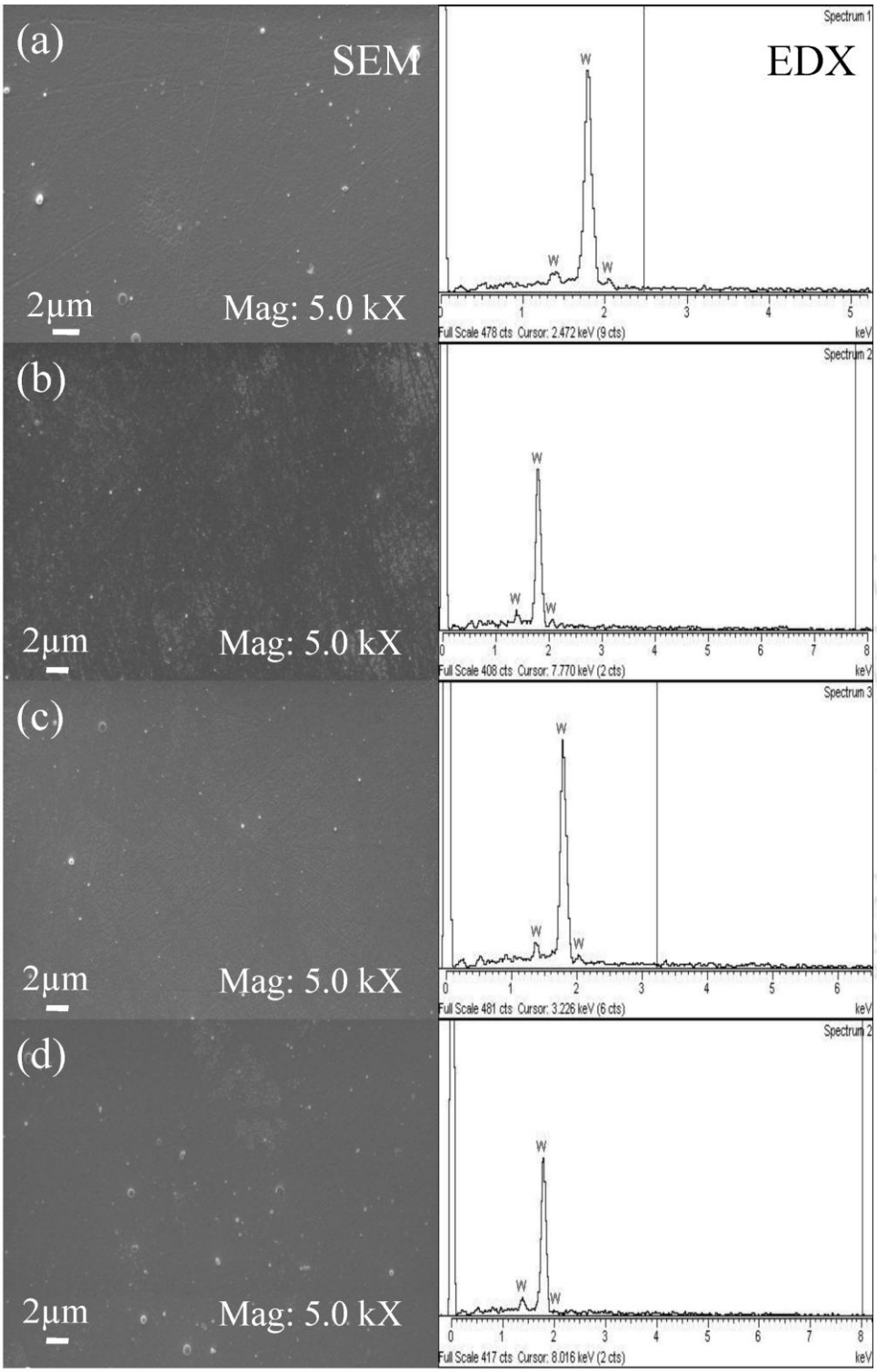

Figure 3.37. SEM image and EDX spectrum of (a) W_{10}, (b) W_{11}, (c) W_{12} and (d) W_{13} samples.

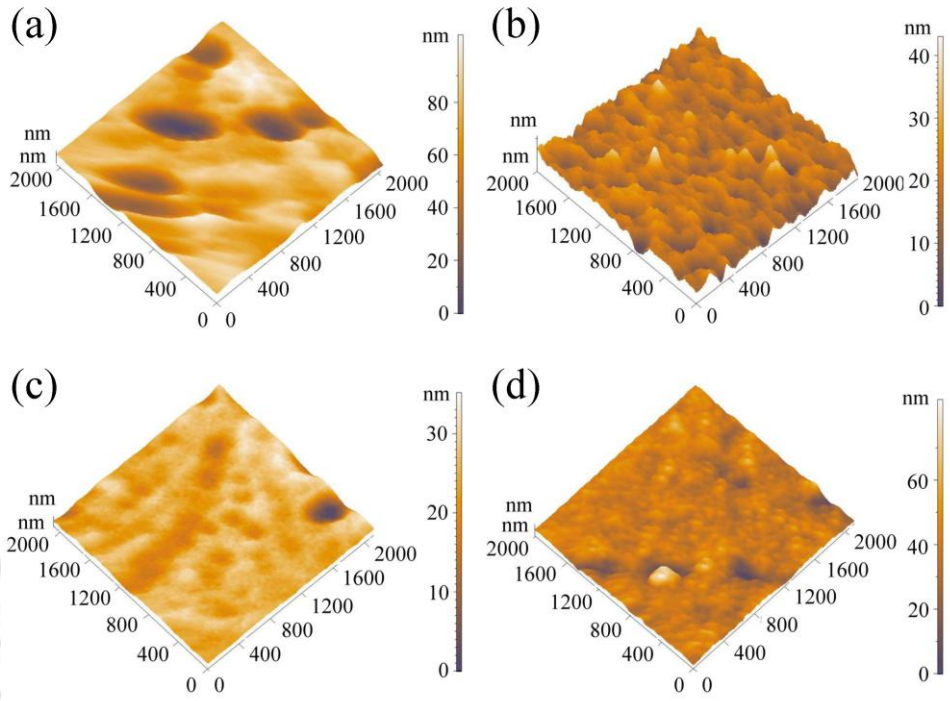

Figure 3.38. AFM image of (a) W_{10}, (b) W_{11}, (c) W_{12} and (d) W_{13} samples.

Table 3.6. Thickness (t), FWHM of W(110) plane, radius of curvature, RMS surface roughness (σ), reflectivity (% R) with reference to aluminum standard mirror and fringe visibility (V).

Sample Code	t (nm)	FWHM of W(110)	r (m)		σ (nm)	% R	V
			before	after		λ = 20 μm	
W_{10}	32	0.9 ^{o}	2.9	2.7	20	82	0.5
W_{11}	101	1.2 ^{o}	4.8	4.1	16	93	0.7
W_{12}	216	0.8^{o}	5.2	5.8	9	96	0.7
W_{13}	326	0.7 ^{o}	5.3	5.0	8	97	0.7

between the laser ablated W cluster/liquid droplet and the atoms of background gas increases with the increase of He ambient gas pressure. This results into the fragmentations of the laser ablated clusters and microstructures, to smaller size particles before deposition, resulting in uniform deposition of the films.

To measure the thickness of the PLD thin films of W as a function of ambient He gas pressure, all the samples were partially deposited on the substrate by placing a mask so as to form the substrate-film step. The interference patterns recorded by Michelson interferometer, figure 2.5(a), of these samples are shown in figures 3.39(a)-(d). The fringe shift due to substrate-film step was clearly observed in CCD images. The left portion of substrate-film step in the interference pattern of each sample represents the masked SS substrate (uncoated) and the right portion represents the coated W films. Measured thickness of W_{10}-W_{13} samples are listed in table 3.6. The thickness of W thin films increased with He ambient gas pressure. The thickness of the W_{10} sample was ~ 32 nm at B_p: ~ 0.05 mbar and that of W_{13} sample was ~ 326 nm at B_p: ~ 1.00 mbar. The deposition rate of W_{10} and W_{I3} samples was 0.5 nm/minute and 5.4 nm/minute, respectively. During deposition, high pressure of He

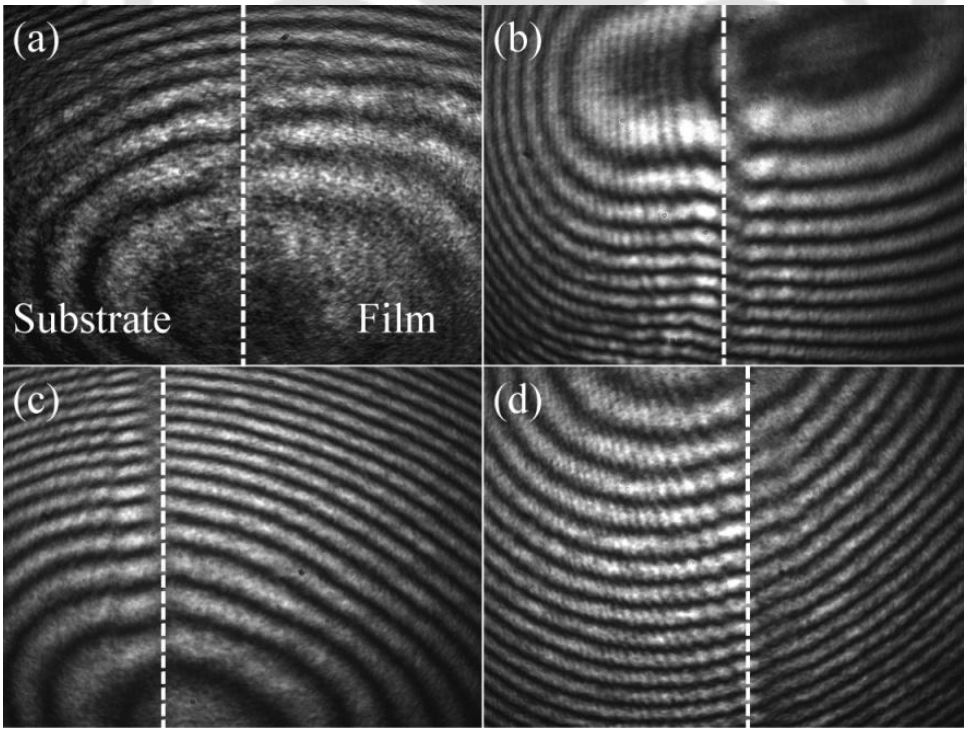

Figure 3.39. Interference pattern of (a) W_{10}, (b) W_{11}, (c) W_{12} and (d) W_{13} samples (vertical line represents substrate-film step).

gas helped in the plasma confinement and increased the density of W plasma which leads to higher deposition rate. The distinct and regular interference fringes confirmed the mirror-like quality of W thin film samples. The radius of curvature of W_{10}-W_{13} samples (after deposition) and corresponding SS substrate (before deposition) are also listed in table 3.6. The marginal difference in the radius of curvature of the deposited samples and corresponding uncoated substrate confirmed that the curved fringes were due to the in-built curvature of the substrate only. The fringe visibility of the samples was also calculated from interference pattern as discussed in section 2.3, equation (2.3) and listed in table 3.6. The minimum and maximum fringe visibility was shown by W_{10} and W_{13} samples. The fringe visibility of W_{13} sample (~ 0.7) which was close to that of the SS substrate (~ 0.8).

The XRD patterns of the W_{10}-W_{13} samples are shown in figure 3.40. Prominent XRD peak of W(110) plane along with two weak XRD peaks of SS substrate were observed. The FWHM of W(110) peak of these samples is listed in table 3.6. The FWHM of W(110) XRD peak decreased with the increase in He ambient gas pressure. This improvement in the crystallinity of W film at higher

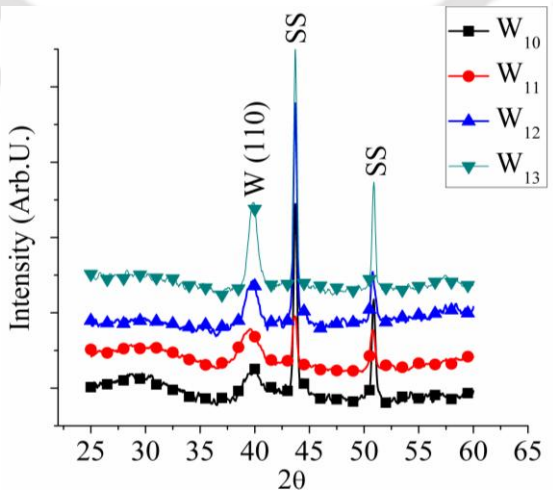

Figure 3.40. XRD pattern of W_{10}-W_{13} samples.

pressure was due to reduction in the kinetic energy of laser ablated W atoms via collisions with He ambient gas atoms. These low kinetic energy laser ablated species uniformly deposited on the substrate, without causing any significant sputtering. Also, the high thickness gave better crystallinity. The FWHM of W(110) XRD peak for W_{13} sample deposited at He pressure of ~ 1.00 mbar was ~ 0.7° which was comparable to that of the film deposited by sputtering technique[95] and slightly more compared to that of bulk W, ~ 0.3°. The elevated temperature as well as presence of background He gas helped in improving the crystallinity of the film.

The specular FIR reflectivity with reference to aluminum standard mirror of W_{10}-W_{13} samples along with polished bulk W target and SS substrate are shown in figure 3.41. The specular FIR reflectivity with reference to aluminum standard mirror at wavelength of 20 μm of the W_{10}-W_{13} samples is listed in table 3.6. It increased with ambient He gas pressure. It was due to improved surface morphology, low RMS surface roughness and crystalline structure approaching to that of bulk. The specular FIR reflectivity was close to that of polished W target for the samples W_{12} and W_{13}

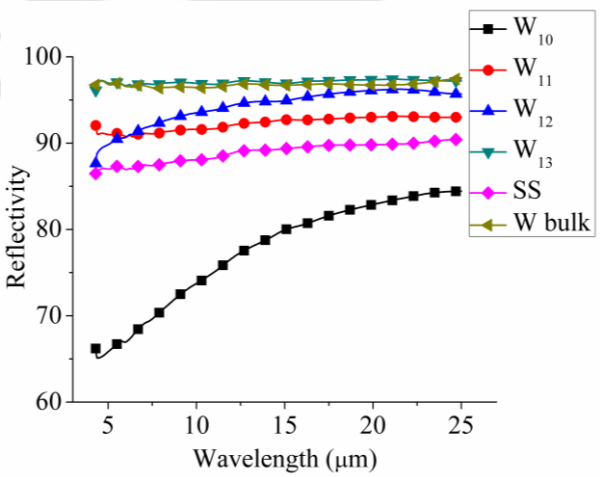

Figure 3.41. Specular FIR reflectivity with reference to aluminum standard mirror of W_{10}-W_{13} samples.

deposited under He pressure of ~ 0.50 mbar and 1.00 mbar. The samples W_{12} and W_{13} showed maximum reflectivity ~ 96 % at wavelength of 20 μm which was higher than that of the SS substrate, ~ 89 %.

3.3 Parametric characterization of pulsed laser deposited thin films of Rh

Rhodium (Rh) is another potential material among other heavy metals for FM fabrication point of view. Mirror-like thin film of Rh were deposited by systematic variation of deposition parameters in the spherical ablation chamber which was evacuated by turbo molecular pump, figure 2.4(a). In totality, eleven Rh thin film samples were prepared and the detail deposition parameters with sample codes are listed in table 3.7. All Rh samples were deposited after pre-conditioning by baking ablation chamber at ~ 70-80 °C during evacuation of ~ 14-15 hour. As observed in the case of Mo and W, subsections 3.1.2 and 3.2.2, the relatively low laser fluence results into the good quality surface of the film devoid of micro structures. Therefore, all the Rh films were prepared at a laser fluence ~ 2 J/cm^2 loosely focusing the laser beam onto the Rh rod as target. The films were deposited at elevated substrate

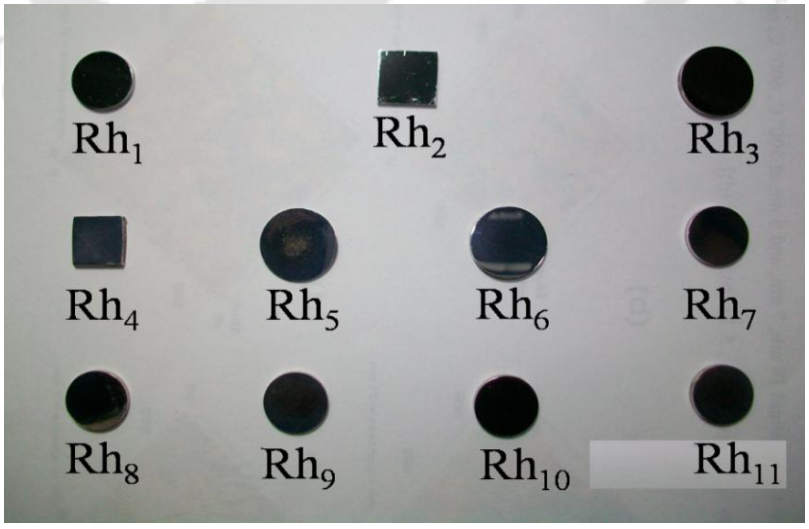

Figure 3.42. Photographs of Rh thin film samples.

Table 3.7. Sample codes and detail deposition parameters of Rh film samples.

SL No.	Sample code	D_{ts}	B_p (mbar)
1	Rh_1	3 cm	10^{-6}
2	Rh_2	4 cm	10^{-6}
3	Rh_3	5 cm	10^{-6}
4	Rh_4	3 cm	0.10
5	Rh_5	3 cm	0.50
6	Rh_6	3 cm	1.00
7	Rh_7	3 cm	2.00
8	Rh_8	4 cm	0.10
9	Rh_9	4 cm	0.50
10	Rh_{10}	4 cm	1.00
11	Rh_{11}	4 cm	2.00

temperature of 500 °C and 60 minute duration of deposition. The photographs of Rh film samples are shown in figure 3.42.

3.3.1 The effect of target-substrate distance on Rh thin films

In the previous sections 3.1 and 3.2, it has been observed that the minimum target-substrate distance should be ~ 3 cm, in order to obtain uniform deposition, free from microstructures. Beyond 5 cm target-substrate distance, the thickness of the film was too low and beyond the detection limit of EDX. Therefore, Rh_1, Rh_2 and Rh_3 samples were deposited under high vacuum (~10^{-6} mbar) at D_{ts}: 3 cm, 4 cm and 5 cm, respectively. The samples were covered partially with a mask during depositions so as to form the substrate-film step for thickness measurement.

The thickness of Rh_1-Rh_3 samples measured by surface profilometer was ~ 86

nm, 82 nm and 54 nm, listed in table 3.8. The corresponding deposition rate of the Rh_1, Rh_2 and Rh_3 samples was ~ 1.4, 1.3 and 0.9 nm/minute, respectively. The variation of thickness of Rh thin films with target-substrate distance is shown in figure 3.43. The film thickness was reduced with the increase of target-substrate distance. It was due to the increase of hemispherical expansion of the LIP plume. At large distance, the hemispherical expansion of LIP lowers the laser ablated particle flux approaching towards the SS substrate, which reduced the deposition rate and hence, thickness of the film.

Table 3.8. Thickness (t), RMS surface roughness (σ) and reflectivity (% R) with reference to aluminum standard mirror of Rh_1-Rh_3 samples.

Sample code	t (nm)	σ (nm)	% R	
			λ = 20 μm	λ = 800 nm
Rh_1	86	8	98	94
Rh_2	82	7	99	97
Rh_3	54	7	99	99

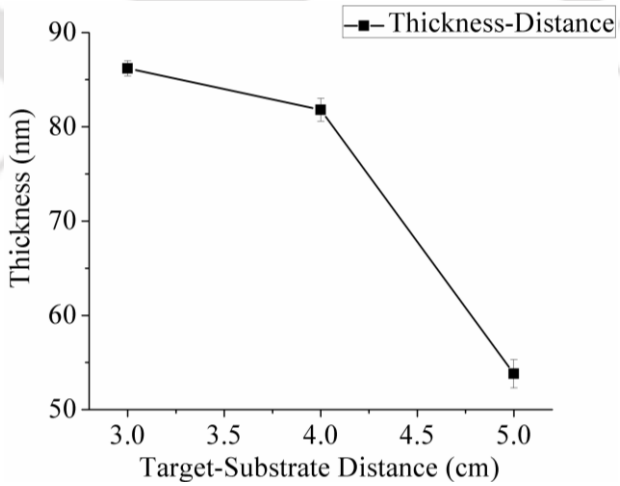

Figure 3.43. Thickness variation with target-substrate distance for Rh_1-Rh_3 thin films.

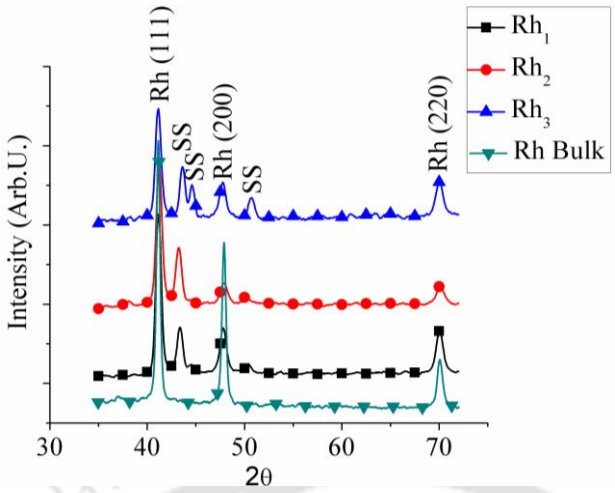

Figure 3.44. XRD pattern of Rh_1-Rh_3 thin films.

The XRD patterns of Rh_1-Rh_3 samples are shown in figures 3.44. The XRD peak of Rh(111), Rh(200) and Rh(220) plane were identified along with two other SS substrate XRD peaks. The Rh(111) peak was prominent compared to that of other observed peaks. The FWHM of Rh(111), Rh(200) and Rh(220) XRD peak were ~ 0.6°, 0.7° and 0.8°, respectively for Rh_1, Rh_2 and Rh_3 samples. Measured FWHM of Rh(111) XRD peak of bulk Rh target was ~ 0.3°. The broadening of FWHM of XRD peak compared to that of bulk material was due to the stress present in the film.[163,167]

The SEM and AFM images of the Rh_1-Rh_3 samples are shown in the figures 3.45(a)-(c) and 3.46(a)-(c), respectively. The SEM images confirmed that Rh films

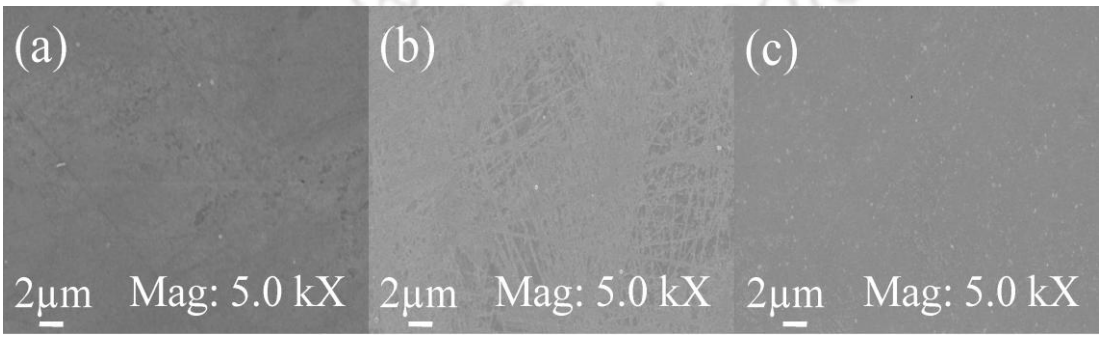

Figure 3.45. SEM image (a) Rh_1, (b) Rh_2 and (c) Rh_3 samples.

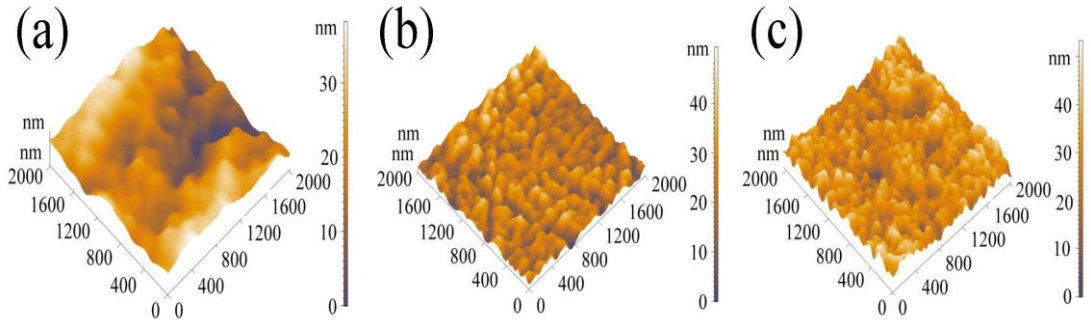

Figure 3.46. AFM image of (a) Rh_1, (b) Rh_2 and (c) Rh_3 samples.

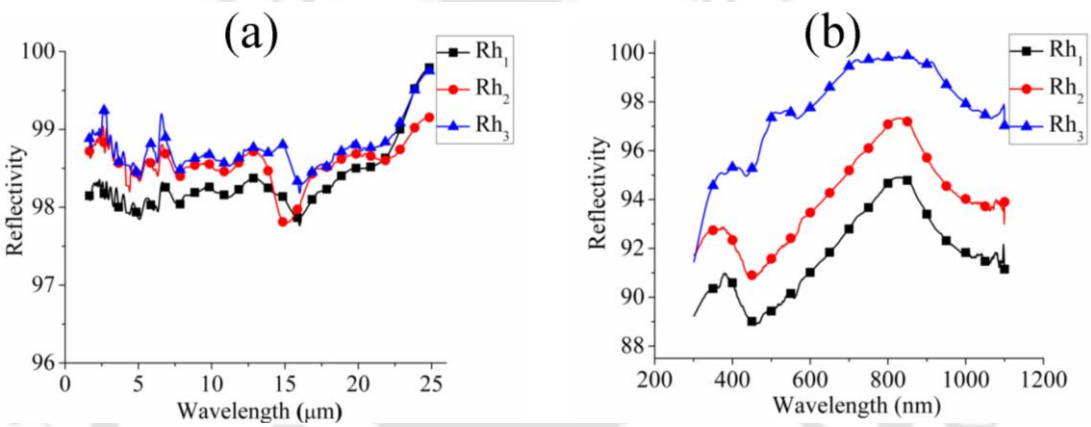

Figure 3.47. Specular reflectivity with reference to aluminum standard mirror of Rh_1-Rh_3 samples (a) FIR range and (b) UV-visible range.

were devoid of formation of any crater and liquid droplet deposition. No signature of eruption of the film from substrate was observed in any of the samples after preserving the films for several months. All the AFM images of the Rh_1-Rh_3 samples confirmed the columnar growth of Rh films. The RMS surface roughness was observed to be ~ 8 nm, 7 nm and 7 nm for Rh_1-Rh_3 samples, listed in table 3.8.

The specular FIR and UV-visible reflectivity with reference to aluminum standard mirror of Rh_1-Rh_3 samples are shown in figures 3.47(a) and 3.47(b). The specular reflectivity with reference to aluminum standard mirror at wavelength of 20 μm and 800 nm are listed in table 3.8. It was observed that the specular reflectivity of

the films was ~ 98-99 % in FIR range of 2-20 μm and ~ 89-99 % in the UV-visible range of 300-800 nm. The FIR and UV-visible reflectivity was slightly higher for Rh_3 sample which was deposited at 5 cm target-substrate distance.

3.3.2 Effect of He ambient pressure on Rh thin films

The thickness of Rh_1-Rh_3 samples was not sufficient for the long term durability for FM application. If the coating thickness of the film is less than that of the ion penetration depth, then the ions would penetrate into the substrate. This will damage the substrate materials which in turn spoil the film surface and hence, the reflectivity. Therefore, the deposition rate and hence, thickness of the film was increased by confining the expansion of plasma in presence of He ambient gas.

As the deposition rate and thickness of the film at D_{ts}: 5 cm was quite low, hence, further experiments were confined to 3 and 4 cm target-substrate distance only. To study the effect of ambient He gas pressure, two different set of samples Rh_4-Rh_7 and Rh_8-Rh_{11} were deposited at D_{ts}: 3 cm and 4 cm under different He ambient gas pressure ~ 0.10, 0.50, 1.00 and 2.00 mbar. The detail deposition parameters are listed in table 3.7. The observed thickness of Rh_4-Rh_7 samples was ~ 121 nm, 254 nm, 246

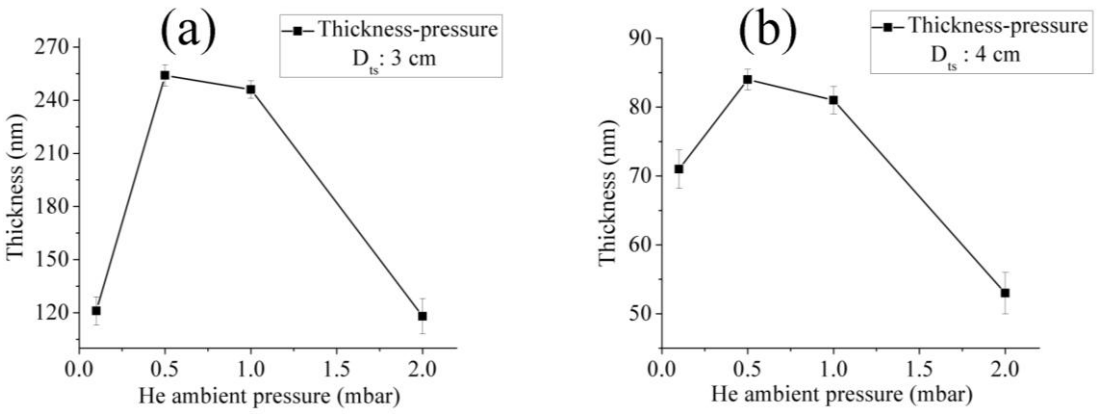

Figure 3.48. Variation of thickness with He ambient pressure (a) Rh_4-Rh_7 and (b) Rh_8-Rh_{11} samples.

Table 3.9. Thickness (t), RMS surface roughness (σ) and reflectivity (% R) with reference to aluminum standard mirror of Rh_4-Rh_7 samples.

Sample code	t (nm)	σ (nm)	% R	
			λ = 20 μm	λ = 800 nm
Rh_4	121	10	95	93
Rh_5	254	9	97	96
Rh_6	246	7	98	99
Rh_7	118	7	98	99

nm and 118 nm, respectively, listed in table 3.9. The deposition rate of these samples was ~ 2.0, 4.2, 4.1 and 1.9 nm/minute, respectively. The variation of thickness of the Rh_4-Rh_7 samples with He ambient gas pressure is shown in figure 3.48(a). It was observed that thickness of the films initially increased up to ~ 0.50 mbar and then decreased with further increase of He ambient gas pressure to ~ 2.00 mbar. It was due to the confinement of the LIP as discussed in previous subsections 3.1.5 and 3.2.5. The Rh_8-Rh_{11} samples were deposited at D_{ts}: 4 cm under same He ambient gas pressures as in the case of D_{ts}: 3 cm. The variation of thickness of Rh_8-Rh_{11} samples with He ambient gas pressure is shown in figure 3.48(b). It also showed the initial increase of thickness up to ~ 0.50 mbar ambient gas pressure and then decreased with the further increase of gas pressure to ~ 2.00 mbar. The measured thickness of Rh_8-Rh_{11} samples was ~ 50 nm to 80 nm, which was low for FM application. Therefore, these films were not subjected to any further characterizations.

The XRD patterns of Rh_4-Rh_7 samples shown in figure 3.49. The prominent plane of these samples was Rh(110) orientation. The relatively less intense weak XRD peak of Rh(220) plane along with two SS substrate XRD peaks were also

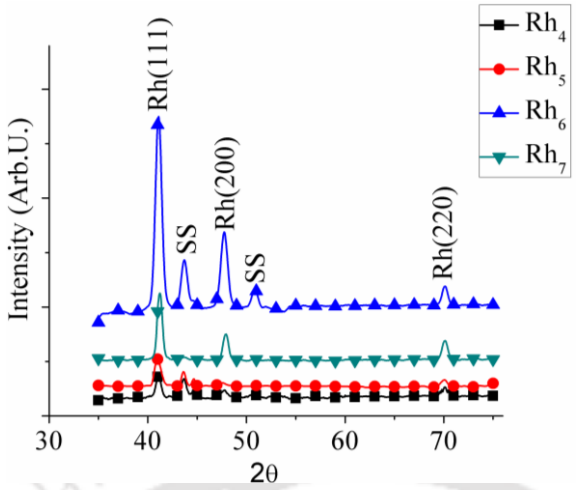

Figure 3.49. XRD pattern of Rh_4-Rh_7 samples.

observed in these samples. The FWHM of Rh(111), Rh(200) and Rh(220) XRD peaks was ~ 0.6°, 0.7° and 0.7°, respectively for all these set of samples, which is comparable to that of Rh film deposited by sputtering technique.[27]

The SEM and AFM image of the samples Rh_4-Rh_7 are shown in the figures

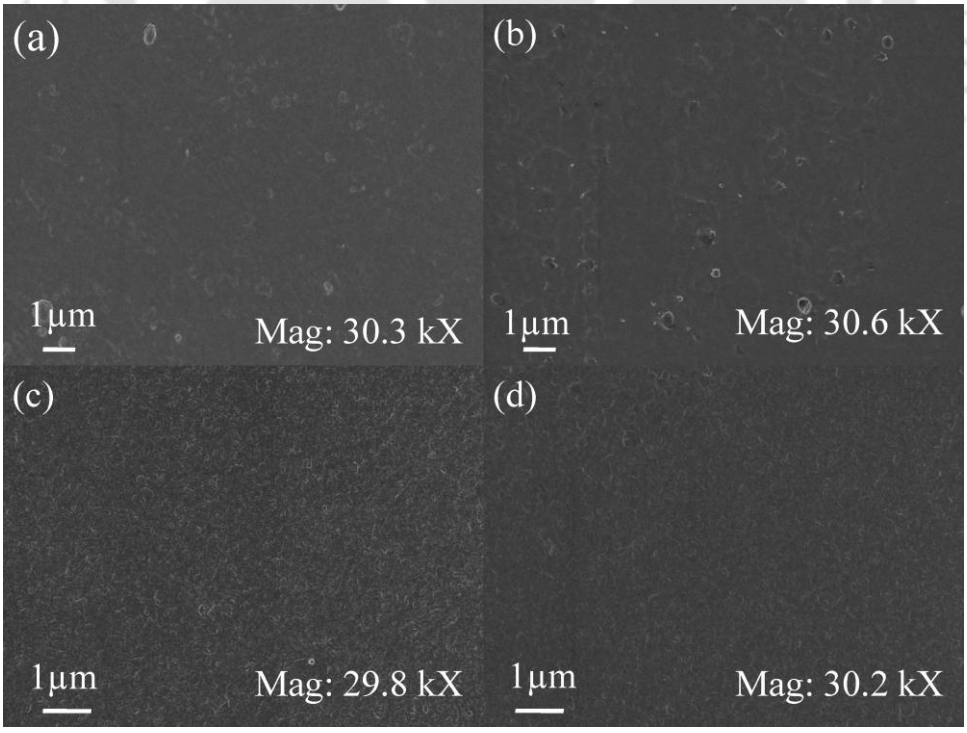

Figure 3.50. SEM image (a) Rh_4, (b) Rh_5, (c) Rh_6 and (d) Rh_7 films.

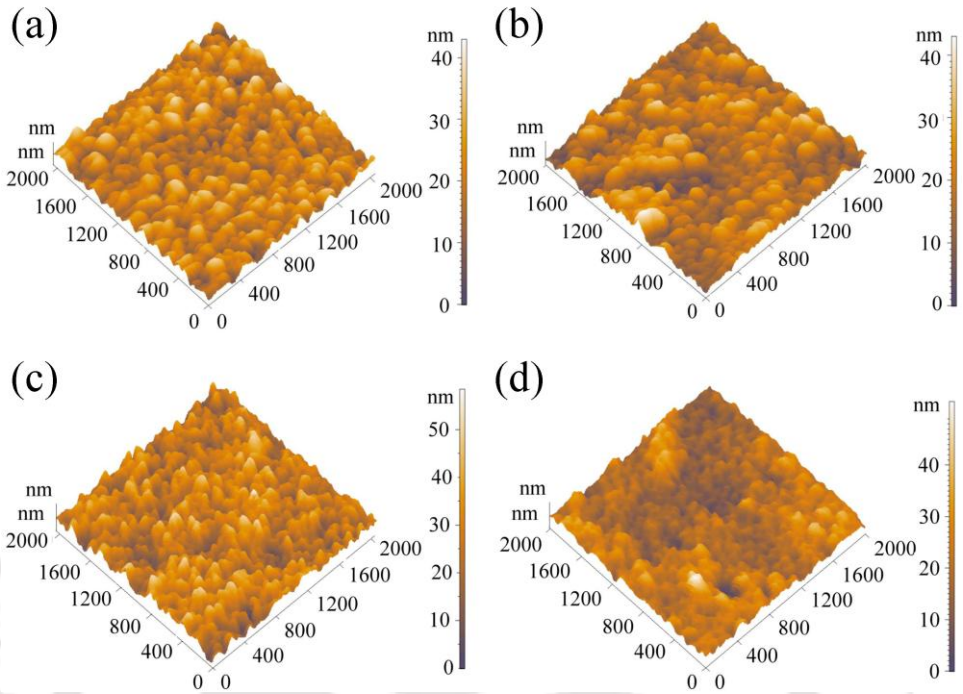

Figure 3.51. AFM image (a) Rh_4, (b) Rh_5, (c) Rh_6 and (d) Rh_7 films.

3.50(a)-(d) and 3.51(a)-(d), respectively. All the samples were nearly free from the formation of craters and liquid droplets. The SEM images further confirmed that the films were uniformly stuck onto the substrate surface and there was no signature of any smudging due to eruption. All the AFM images confirmed the columnar growth of Rh thin films. The RMS surface roughness was observed to be ~ 10 nm, 9 nm, 7 nm and 7 nm for Rh_4-Rh_7 samples, respectively. The surface roughness reduced with the increase of He ambient gas pressure.

The specular FIR and UV-visible reflectivity with reference to aluminum standard mirror of Rh_4-Rh_7 samples are shown in figures 3.52(a) and 3.52(b), respectively. The specular reflectivity with reference to aluminum standard mirror at wavelength of 20 µm and 800 nm are listed in table 3.9. The specular reflectivity of both the samples Rh_6 and Rh_7 samples was ~ 98 % at wavelength of 20 µm and 99 %

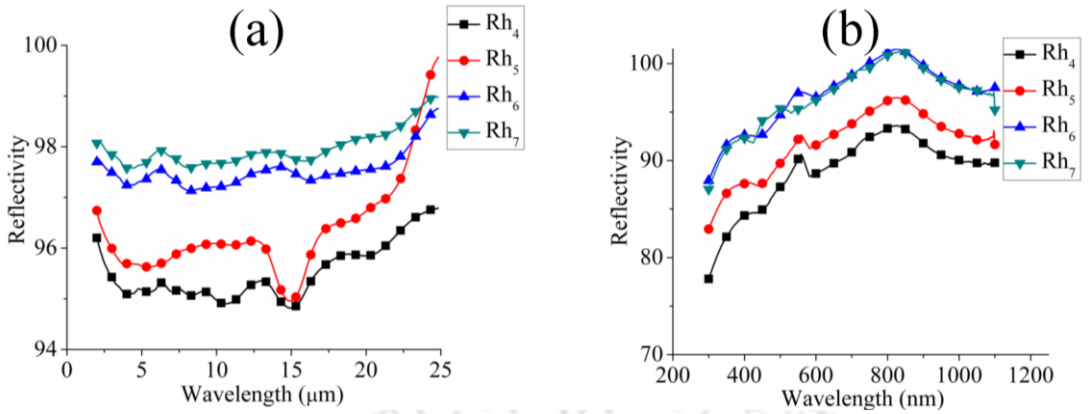

Figure 3.52. Specular reflectivity with reference to aluminum standard mirror of Rh_4-Rh_7 thin films (a) FIR range and (b) UV-visible range.

at wavelength of 800 nm. The poor reflectivity of Rh_4 sample deposited under ~ 0.10 mbar He ambient gas was due to the slightly higher RMS roughness. The reflectivity improved with the increase of He ambient pressure which could be attributed to the lower RMS surface roughness. The FIR and UV-visible reflectivity of Rh_3 which was deposited at D_{ts}: 5 cm under vacuum ~ 10^{-5} mbar, was close to Rh_6 and Rh_7 samples but, Rh_3 sample possesses low thickness of ~ 54 nm compared to that of the samples Rh_4-Rh_7 having thickness more than 120 nm.

3.4 Overall optimum deposition parameters

The overall optimized deposition parameters to deposit mirror-like thin films of Mo, W and Rh using PLD technique were obtained by studying the effects of different deposition parameters on the quality of thin films. To obtain the thin films of heavy metals of Mo, W and Rh via PLD technique free from oxygen contamination, the degassing of the ablation chamber by heating at temperature ~ 70-80 °C during ~ 14-15 hour evacuation prior to deposition were required. The optimized parameters for obtaining the good quality thin films are (a) laser fluence ~ 2 J/cm^2, (b) elevated

substrate temperature of 500 °C, (c) target-substrate distance ~ 3 cm and (d) He ambient gas pressure ~ 1.0 mbar. The thickness of Mo, W and Rh PLD thin films at these parameters for 60 minute deposition time was more than 245 nm.

3.5 Conclusions

In this chapter, parametric characterization of mirror-like thin films of Mo, W and Rh fabricated by PLD technique is presented. The overall optimized parameters are consolidated in section 3.4. Mo sample deposited under optimum deposition parameters, showed prominent XRD peak of Mo(110) plane with FWHM of 0.6°, reflectivity ~ 97-99 % in wavelength range, 2-20 μm and that of ~ 75-83 % in wavelength range, 300-800 nm with reference to aluminum standard mirror. The thickness of this film, deposited for 60 minute was ~ 386 nm. W sample deposited under optimum deposition parameters, possessed prominent XRD peak of W(110) plane with FWHM of 0.7°, RMS surface roughness ~ 8 nm, reflectivity ~ 97 % with reference to aluminum standard mirror in wavelength range, 2-20 μm. The fringe visibility and thickness of this W sample was ~ 0.7 and ~ 326 nm, respectively. The Rh sample deposited under optimum condition showed prominent XRD peak of Rh(111) plane with FWHM of 0.6°, reflectivity ~ 98 % in wavelength range, 2-20 μm and that of ~ 89-99 % in wavelength range, 300-800 nm with reference to aluminum standard mirror. Thickness of this Rh sample was ~ 246 nm. The Mo thin films was very unstable as it got contaminated with oxygen within few weeks after fabrication whereas it was observed that the W and Rh films did not show any signature of eruption of the film from the substrate even after couple of month. Therefore, W and Rh thin film mirror were subjected to ion beam irradiation, discussed in chapter 4.

Chapter 4

4. Effect of ion beam irradiation on W and Rh thin films

One of the potential application of mirror-like thin film of Rh and W is in the optical diagnostic system of fusion reactor as First Mirror (FM).[1-4,26,73] The components installed inside these high temperature plasma systems are exposed to high energetic ion flux of energy ranging from few eV to hundreds of keV.[24,25,38,51,168] Therefore, to ensure the sustainability of mirror-like thin films of Rh and W via PLD technique, reported in previous chapter, these were exposed to H and D ion beams. Mo thin films was excluded from this part of the work as being sensitive to atmosphere and easily got contaminated with oxygen within few weeks of fabrication resulting into the poor reflectivity.

4.1 Effect of H ion beam irradiation on W thin films

In order to study the effect of PLD W mirror on H ion beam irradiation, the samples W_{10}, W_{11}, W_{12} and W_{13}, table 3.4 chapter 3, were irradiated by 8 keV H ion beam for 30 minute duration having ion flux ~ 8.9×10^{14} ions/cm^2/s. The 30 minute exposure of this particle flux corresponded to an ion fluence of ~ 1.6×10^{18} ions/cm^2. The detail of ion beam irradiation setup is described in chapter 2, section 2.4. The thickness of the film, SEM images, crystal structure, reflectivity and interference

pattern of W_{10}-W_{13} samples prior to irradiation are detailed in Chapter 3, subsection 3.2.4.

4.1.1 Surface characterization of post irradiated W thin films

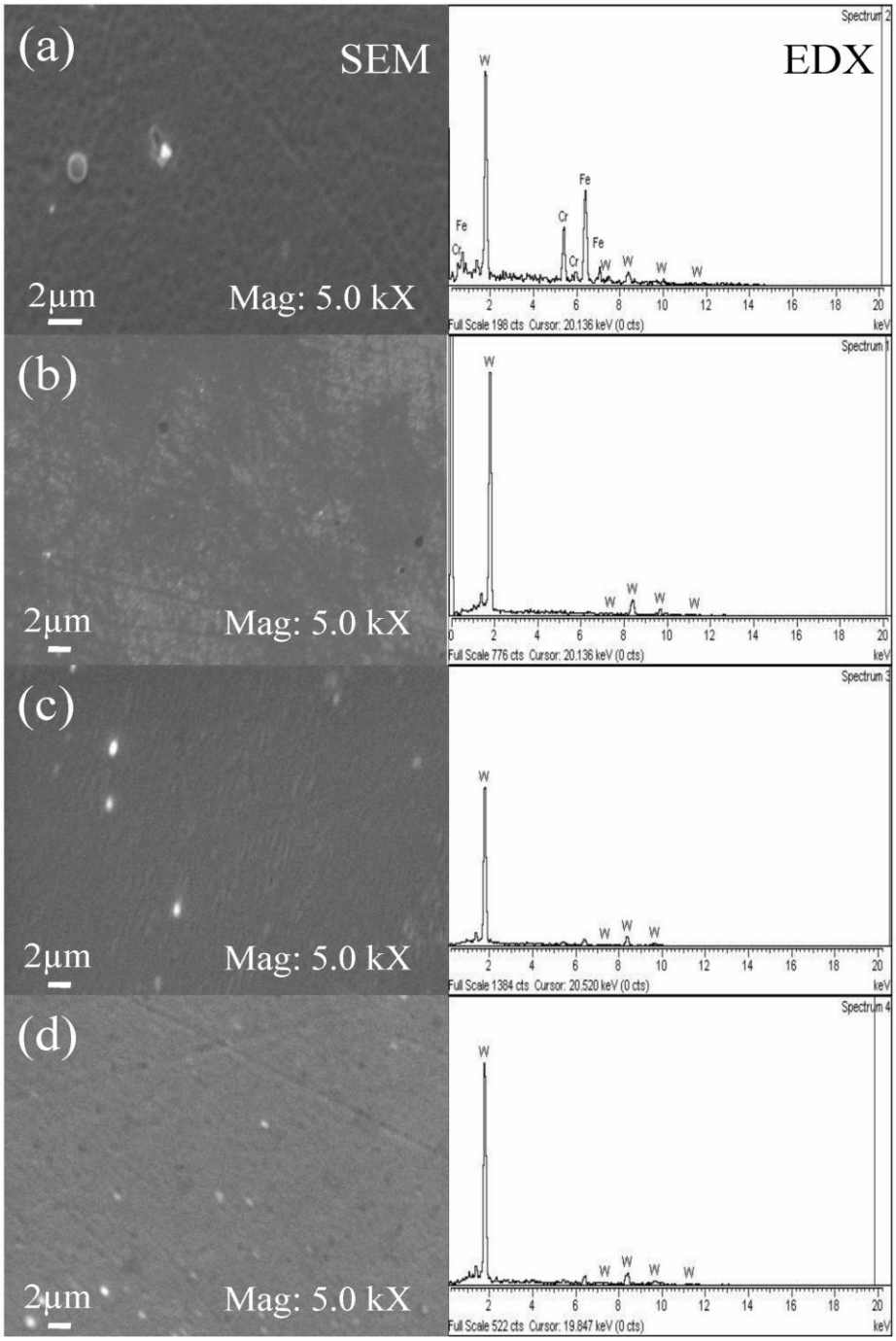

Figure 4.1. SEM image and EDX spectrum of (a) W_{10}, (b) W_{11}, (c) W_{12} and (d) W_{13} samples.

The SEM image and corresponding EDX spectrum for W_{10}-W_{13} samples after 8 keV H ion beam irradiation is shown in figure 4.1. The SEM images showed the surfaces of W mirrors remained unaffected after irradiation. Post irradiated mirror-like thin films were free from development of any cracks or eruption of the film from substrate. The corresponding EDX spectra are shown adjacent to the respective SEM images, figure 4.1. The EDX spectrum of W_{10} sample after ion beam irradiation, figure 4.1(a), showed the constituent elements Cr, Fe, etc. of SS substrate. Since, the thickness of W_{10} thin film sample was only ~ 32 nm which was less than that of 8 keV H ion penetration depths into the films, therefore, significant amount of H ions were able to penetrate to the W film and extended to the substrate. This resulted in the ejection of some atoms from SS substrate which may came out on the surface of the thin film sample and being detected in the post exposure EDX spectrum. The rest of the samples have thickness ~ 101, 216 and 326 nm, larger than the ion penetration depth of 8 keV H ion beam which prohibited the ion beam reaching to the substrate and hence, the EDX spectra of all these samples were free from Cr, Fe, etc.

4.1.2 Effect of H ion irradiation on FIR reflectivity of PLD W thin films

The FIR reflectivity with reference to aluminum standard mirror of W_{10}-W_{13} samples along with bare polished SS substrate before and after ion beam irradiation is shown in figure 4.2. The line and symbol in red color represents reflectivity spectra after ion beam exposure and that in black color represents unexposed spectra. The FIR reflectivity with reference to aluminum standard mirror of W_{10}-W_{13} samples at a wavelength of 20 μm before H ion beam irradiation is listed in table 3.6 (Chapter 3, subsection 3.2.5). The FIR reflectivity at wavelength of 20 μm after irradiation was 86 % (↑), 92 % (↓), 94 % (↓), 95 % (↓) and 96 % (↑) for W_{10}, W_{11}, W_{12}, W_{13} and SS

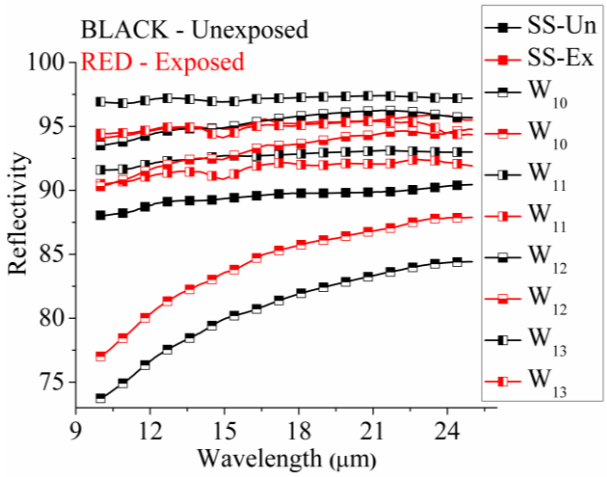

Figure 4.2. Specular FIR reflectivity with reference to aluminum standard mirror of W_{10}-W_{13} samples and SS substrate before and after H ion beam irradiation.

substrate, respectively. The changes in reflectivity, after ion beam irradiation, are indicated by upward (↑) arrows for increase and that of decrease by downward (↓) arrows. The reflectivity of W_{10} sample and SS substrate was increased after ion beam irradiation, whereas it decreased slightly for rest of the samples. The effect of ion beam irradiation on the changes in reflectivity can be explained on the basis of ion range and straggle length of 8 keV H ion beam as discussed in following subsection.

4.1.3 Ion range and ion straggle into W for 8 keV H ion beam

To explain the effect of irradiation of 8 keV H ion beam of flux ~ 8.9×10^{14} ions/cm^2/s for 30 minute on W thin films, the damage parameters: ion range, ion straggle and sputtering yield were calculated numerically using TRIM Monte Carlo simulation code. Figures 4.3(a) and 4.3(b) show the 8 keV H ion penetration depths into W and SS substrate, respectively. The ion range (R_P), ion straggle (S_P) and sputtering yield (Y) were found to be 44 nm, 23 nm, 0.0029 atoms/ion for W and 60 nm, 26 nm, 0.0043 atoms/ion for SS, respectively. For W_{10} sample having thickness ~

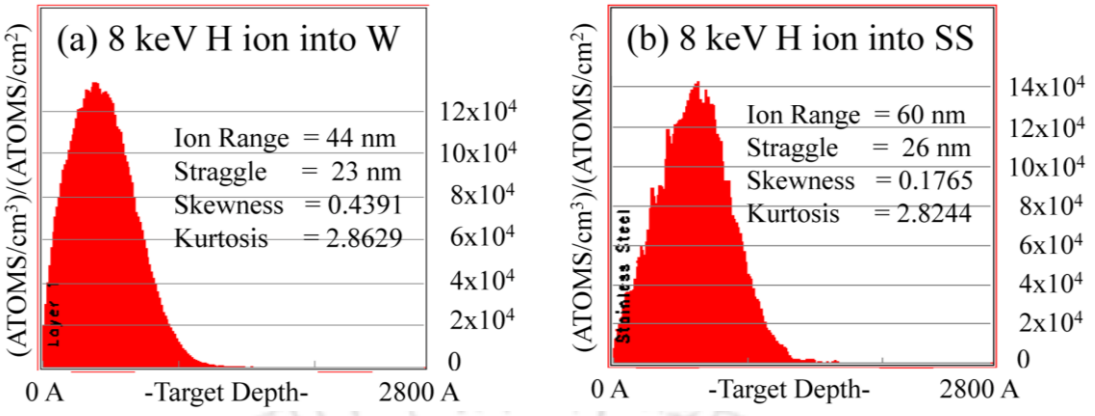

Figure 4.3. Ion range (R_P) and ion straggle (S_P) into (a) W and (b) SS substrate.

32 nm, less than that of ion penetration depth of 44 nm, H ion crossed the W layer and penetrated into the substrate. Therefore, sputtering of W layer and damage were low which made the surface more uniform and thereby, slightly improving the post irradiated FIR reflectivity, whereas for rest of the samples W_{11}-W_{13}, the thickness was larger than the ion penetration depth. Hence, H ion beam was completely absorbed within the W thin film causing sufficient lattice damage to the W layer. Due to this lattice damage within W thin film, the FIR reflectivity was reduced slightly. The reflectivity of samples W_{11}-W_{13} was reduced by ~ 2 % due to exposure of 8 keV H ion beam for 30 minute with particle flux ~ 8.9×10^{14} ions/cm^2/s. Normally in fusion reactor, the particle flux is of similar order[24] hence, all these W mirror-like thin films can be used in fusion reactor for comparable time of exposure.

4.2 Effect of D ion beam irradiation on W thin films

D ion is another choice of fuel material to the fusion reactor. Therefore, mirror-like PLD W thin films were also exposed to D ion beams. For this, samples of mirror-like thin films W_{14}, W_{15} and W_{16} were fabricated at optimum deposition parameters (as obtained in previous chapter 3). These films were prepared in spherical

ablation chamber evacuated by turbo molecular pump as described in chapter 2, section 2.2. After deposition, all the samples were annealed at a temperature of 500 °C, for 60 minute under He as ambient pressure of ~ 1.0 mbar, same as that of deposition pressure and then slowly cooled down without breaking the vacuum. The cooling rate was maintained at ~ 1.6 °C/minute from 500 to 100 °C. Afterwards, the heater was switched off and allowed to cool down from 100 °C to room temperature on its own. This ramp cooling was incorporated so as to reduce the stress developed during sudden cooling from 500 °C to room temperature. The thicknesses of these films were ~ 326 nm. The samples W_{14}, W_{15} and W_{16} were irradiated by 10, 20 and 30 keV D ion beam for 10 minute duration, respectively. The ion flux of D ion beam was ~ 1.2×10^{14} ions/cm^2/s of all the three energies. The 10 minute exposure of this particle flux corresponded to an ion fluence ~ 7.8×10^{16} ions/cm^2.

4.2.1 Surface characterization of W thin films before and after D ion beam exposure

The SEM images of the samples W_{14}-W_{16} before and after exposure to D ion beam are shown in figure 4.4. The SEM images showed thinly distributed granular structures on the W samples before as well as after irradiation. The size of granular structure was in the range of ~ 40 nm to 130 nm. The sample surface was observed to be free from cracks and there was no signature of erosion of the film from substrate before as well as after irradiation. The post irradiated W thin film samples were observed to be free from any blisters formation. This confirmed that the film adhesion to SS substrate was uniform. The post irradiated W thin films were also observed to be free from any blisters formation in contrary to other reports.[25,49,64,169] The D ion fluence in other reports was more than ~ 10^{20} ions/cm^2 compared to that of the ion

fluence of the present experiment, ~ 7.8×10^{16} ions/cm^2. Due to lower ion fluence of the present experiment, the lattice damage arising from the implanted species was insufficient to cause any observable blisters formation. The critical fluence of D ions required to form blisters on W surface is ~10^{19}-10^{20} particles/cm^2.[170,171] The AFM images of the samples W_{14}-W_{16} before and after exposure to D ion beam are shown in figure 4.5. The RMS surface roughness (σ) of the samples, measured from AFM images, before and after irradiation, is listed in table 4.1. The listed values are

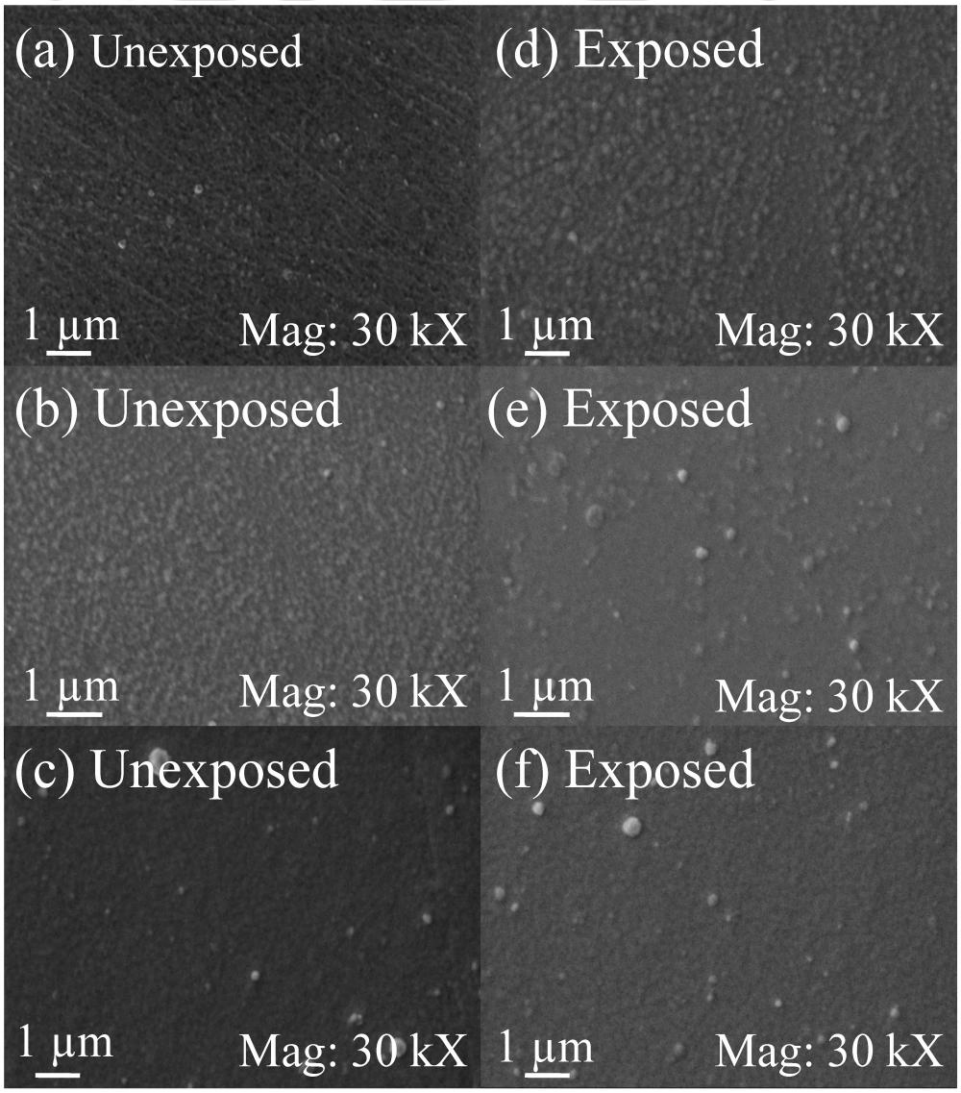

Figure 4.4. The SEM image before irradiation (a) W_{14}, (b) W_{15} and (c) W_{16} and that of after irradiation (d) W_{14}, (e) W_{15} and (f) W_{16}, respectively.

averaged over three distinct scan area (2 µm × 2 µm) of each W sample. Before irradiation, RMS surface roughness of the samples W_{14}, W_{15}, W_{16} was ~ 9 nm, 17 nm, 16 nm and that of after irradiation it was increased to ~ 17 nm, 24 nm and 24 nm, respectively. Thus, the change in RMS surface roughness after irradiation was ~ 8, 7 and 8 nm for W_{14}-W_{16} samples, respectively.

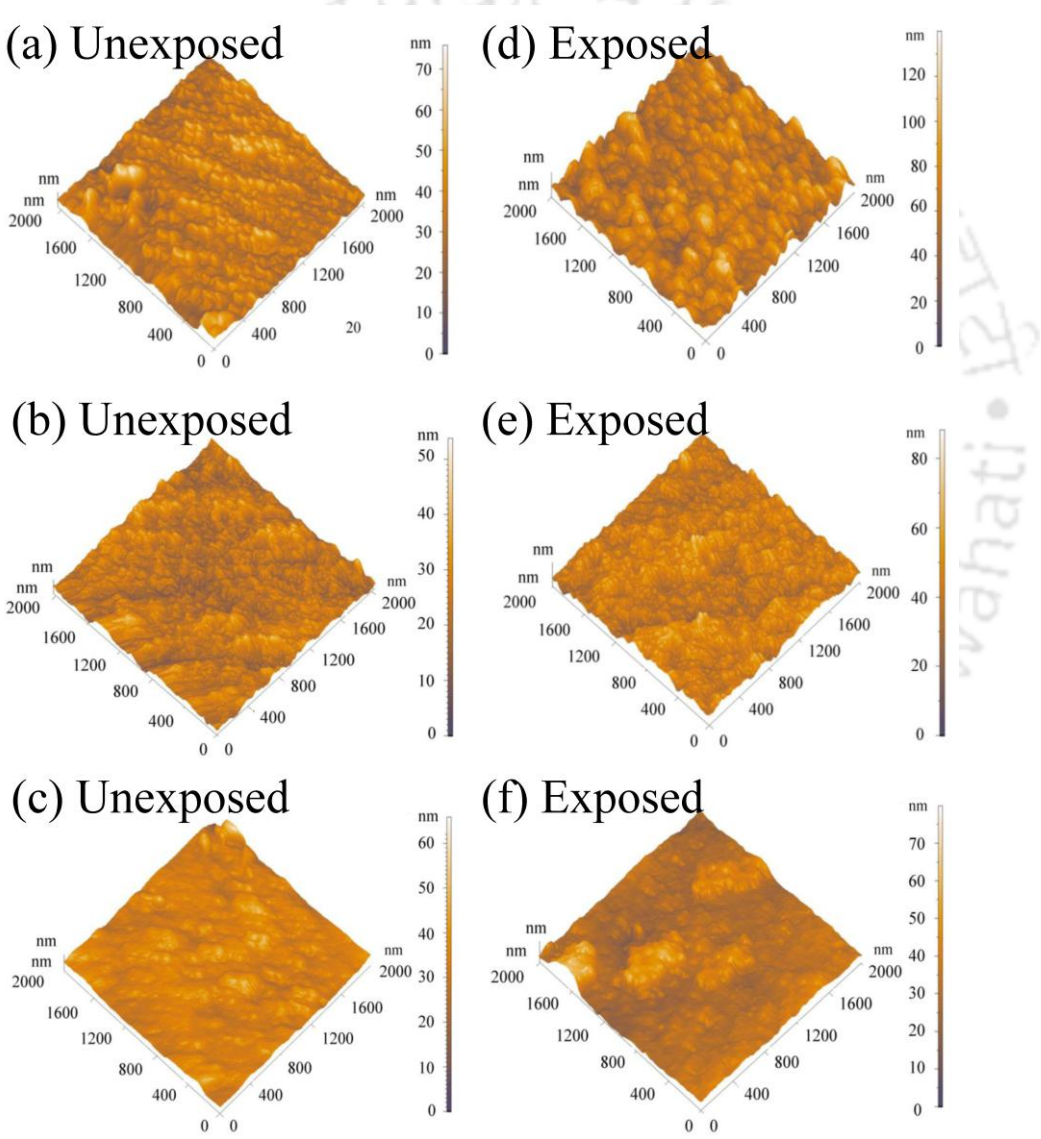

Figure 4.5. The AFM image before irradiation (a) W_{14}, (b) W_{15} and (c) W_{16} and that of after irradiation (d) W_{14}, (e) W_{15} and (f) W_{16}, respectively.

Table 4.1. Sample codes, D ion energy (E), ion penetration depth (R_p), ion straggle (S_p), sputtering yield (Y), RMS surface roughness (σ) and reflectivity (% R) with reference to aluminum standard mirror of W thin films.

Sample code	E (keV)	R_p (nm)	S_p (nm)	Y (atoms/ ion)	σ		% R			
					before	after	λ = 20 μm		λ = 800 nm	
							before	after	before	after
W_{14}	10	62	32	0.0054	9	17 ↑	97	91 ↓	81	51 ↓
W_{15}	20	111	53	0.0055	17	24 ↑	93	91 ↓	84	55 ↓
W_{16}	30	153	70	0.0031	16	24 ↑	95	93 ↓	82	54 ↓

4.2.2 Effect of energy of D ion beam irradiation on the reflectivity of W thin films

Specular FIR and UV-visible reflectivity with reference to aluminum standard mirror of W_{14}-W_{16} samples before and after ion beam irradiation is shown in figures 4.6(a) and 4.6(b), respectively. The percentage wise reduction in reflectivity of mirror-like W thin films in the FIR range of 2-20 μm, was ~ 6-9 % for 10 keV, 1-4 % for 20 keV and 1-3 % for 30 keV D ion beam irradiation. In the UV-visible range of 300-800 nm, the reduction in reflectivity was ~ 28-38 % for 10 keV, ~ 29 % for both

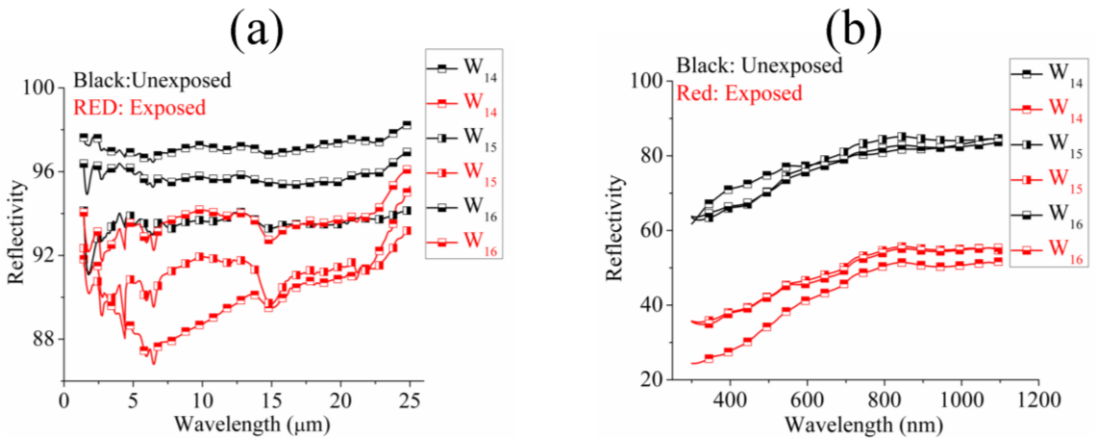

Figure 4.6. Specular reflectivity with reference to aluminum standard mirror (a) FIR range and (b) UV-visible range.

20 and 30 keV D ion beam irradiation. The increase in RMS surface roughness of the W thin films due to D ion beam irradiation could be one of the factors for the reduction of optical reflectivity. In order to show the comparison of reflectivity before and after irradiation, the FIR and UV-visible reflectivity with reference to aluminum standard mirror at arbitrarily chosen wavelengths of 20 μm and 800 nm are listed in the table 4.1. The reflectivity before and after ion beam irradiation at 20 μm was ~ 97 % and 91 % for W_1, 93 % and 91 % for W_2, 95 % and 93 % for W_3, respectively. At 800 nm, the reflectivity before and after irradiation was ~ 81 % and 51 % for W_1, 84 % and 55 % for W_2, 82 % and 54 % for W_3, respectively. The post exposure changes in reflectivity at 20 μm were ~ 6 %, 2 % and 2 % for W_{14}, W_{15} and W_{16} samples, respectively. The corresponding changes at 800 nm were ~ 30 %, 29 % and 28 %, respectively. The post exposure RMS surface roughness as listed in table 4.1, was increased and its effect on reflectivity can be analyzed from Bennett's formula.[164,165] According to Bennett's formula, the reflectivity at normal incidence is given by $R=R_o exp[-(4\pi\sigma/\lambda)^2]$, where "*R*" is the observed reflectivity, "R_o" is the reflectivity of a perfectly smooth surface of the same material, "λ" is wavelength and "σ" is the RMS surface roughness of the same sample.[164,165] At wavelength of 20 μm, a change in RMS surface roughness ~ 8 nm causes degradation of optical reflectivity by a factor less than 0.2 % and that of at 800 nm ~ 4 %. Moreover, if σ/λ increases, the amount of coherently reflected light from mirror surface within acceptance angle of the detector decreases which leads to poor specular reflectivity. At 20 μm, σ/λ is ~10^{-4} whereas that of at wavelength of 800 nm, is 0.02. Therefore, due to low σ/λ ratio in FIR range, amount of coherently reflected light into the detector dominates where as in UV-visible range, amount of incoherently reflected light is more compared to that

of coherent light. Therefore, in the FIR range, the post exposure reflectivity was more compared to that of UV-visible range. The second factor contributing towards the lowering of reflectivity could be the lattice irregularities, precipitation and trapping of foreign particles in the host lattice due to ion irradiation within the detecting depth limit of optical photon. The possibility of the formation of deuterium bonding with host lattice atoms[172], could also be responsible for the changes in post exposure reflectivity.

4.2.3 Ion range and ion straggle into W for 10, 20 and 30 keV D ion beam

The post irradiation changes in reflectivity of W_{14}-W_{16} samples showed dependence on the energy of D ion beam. This can be explained on the basis of ion range, straggle length, sputtering yield for 10, 20 and 30 keV D ion beam. The ion range and straggle of 10, 20 and 30 keV D ion into W thin film, calculated using TRIM Monte Carlo simulation code, are shown in figure 4.7(a)-(c), respectively. Numerical calculations showed that the ion range (R_P), ion straggle (S_P) and sputtering yield (Y) for 10, 20 and 30 keV D ion irradiation onto W thin films were 62 nm, 32 nm, 0.0054 atoms/ion; 111 nm, 53 nm, 0.0054 atoms/ion and 153 nm, 70 nm, 0.0031 atoms/ion, respectively, as listed in table 4.1. The thickness of all the W thin films, ~ 326 nm, was larger than that of the D ion penetration depth for all these three energies. Therefore, the D ion beam was completely absorbed within the W thin films causing sufficient lattice damage to this layer. Due to this lattice damage into W, the reflectivity of PLD W thin film mirrors particularly in UV-visible range undergoes drastic reduction. The penetration depth of optical photon into the W mirror was ~ 45 nm at wavelength of 20 µm. The implantation density of D ions within ~ 45 nm, the penetration depth of FIR photons, were ~ 8×10^4, 4×10^4 and 2×10^4

(atoms/cm^3)/(atoms/cm^2) for 10, 20 and 30 keV, respectively. Thus, lattice damage in the sample W_{14} was more than that of the samples W_{15} and W_{16} within the optical penetration depth of FIR photons. Therefore, post exposure FIR reflectivity of the

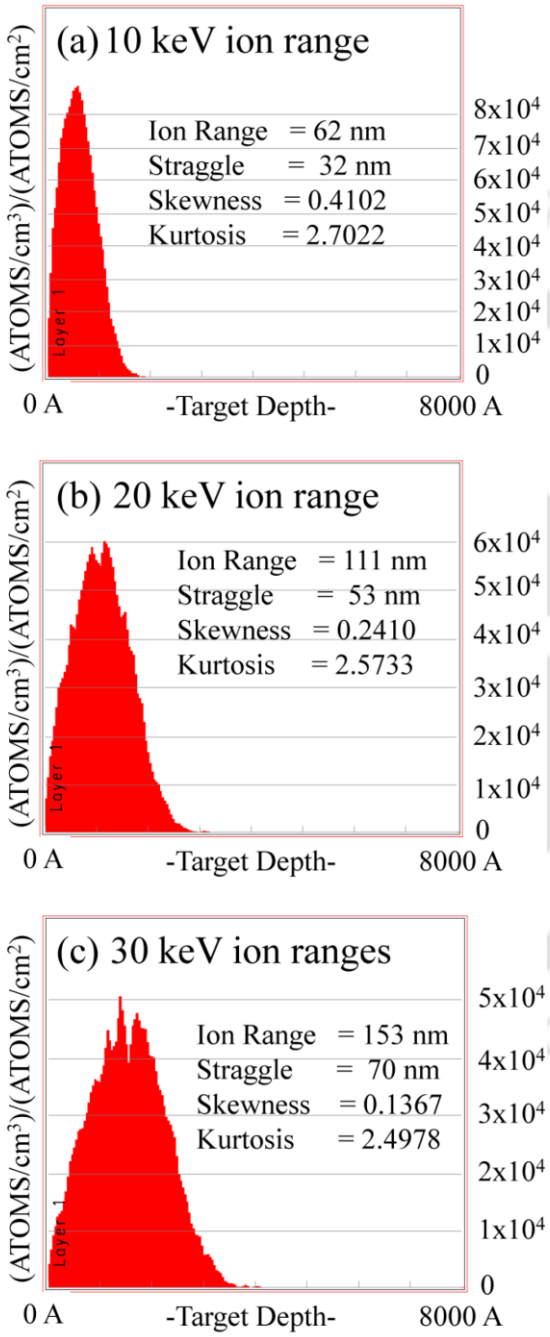

Figure 4.7. Ion penetration depth and ion straggle into W for (a) 10, (b) 20 and (c) 30 keV D ions.

sample W_{14} suffered slightly larger degradation compared to that of the samples W_{15} and W_{16}. The implantation density of D ion within ~ 10 nm, the visible photon penetration depth, was ~ 1×10^{4} (atoms/cm^{3})/(atoms/cm^{2}) for all the energies in W hence, lattice damage was same. Therefore, the reduction in the post exposure reflectivity in visible range for all the samples was nearly same.

4.3 Effect of D ion beam irradiation on Rh thin films

In order to study the effect of D ion beam irradiation on Rh thin films, the samples Rh_{12}, Rh_{13} and Rh_{14} were deposited under optimum parameters. The optimum deposition parameters were ~ 3 cm target-substrate distance, ~ 1.0 mbar He ambient gas pressure and ~ 2 J/cm^{2} laser fluence. These films were prepared in spherical ablation chamber evacuated by turbo molecular pump as described in chapter 2, section 2.2. These samples were deposited for 60 minute at ~ 500 °C of the substrate. After deposition, the Rh_{12}-Rh_{14} samples were allowed to cool down under same deposition pressure at a cooling rate ~ 1.6 °C/minute from 500 to 100 °C. Afterwards, the heater was switched off and allowed to cool down from 100 °C to room temperature naturally. The thickness of these samples was ~ 246 nm. All the thin film samples, Rh_{12}-Rh_{14} were exposed to 10, 20 and 30 keV of D ion beam with ion flux ~ 1.2×10^{14} ions/cm^{2}/s for 10 minute, respectively. The 10 minute exposure of this particle flux corresponded to an ion fluence ~ 7.8×10^{16} ions/cm^{2}. The samples were subjected to SEM, AFM, FIR and UV-visible spectrometers before and after D ion beam exposure and the results were compared.

4.3.1 Surface characterization of Rh thin films before and after D ion beam exposure

The SEM images for Rh_{12}-Rh_{14} samples before and after D ion beam

irradiation is shown in figures 4.8(a)-(c) and 4.8(d)-(f), respectively. The SEM images hardly reflect any modification of the surface after ion beam irradiation. The AFM images of Rh_{12}-Rh_{14} samples before ion beam irradiation are shown in figures 4.9(a)-(c) and that of after irradiation are shown in figures 4.9(e)-(f). The columnar structure of all the films remained intact even after irradiation. The RMS surface roughness of the samples Rh_{12}-Rh_{14} before ion beam irradiation was ~ 10 nm and that of after ion

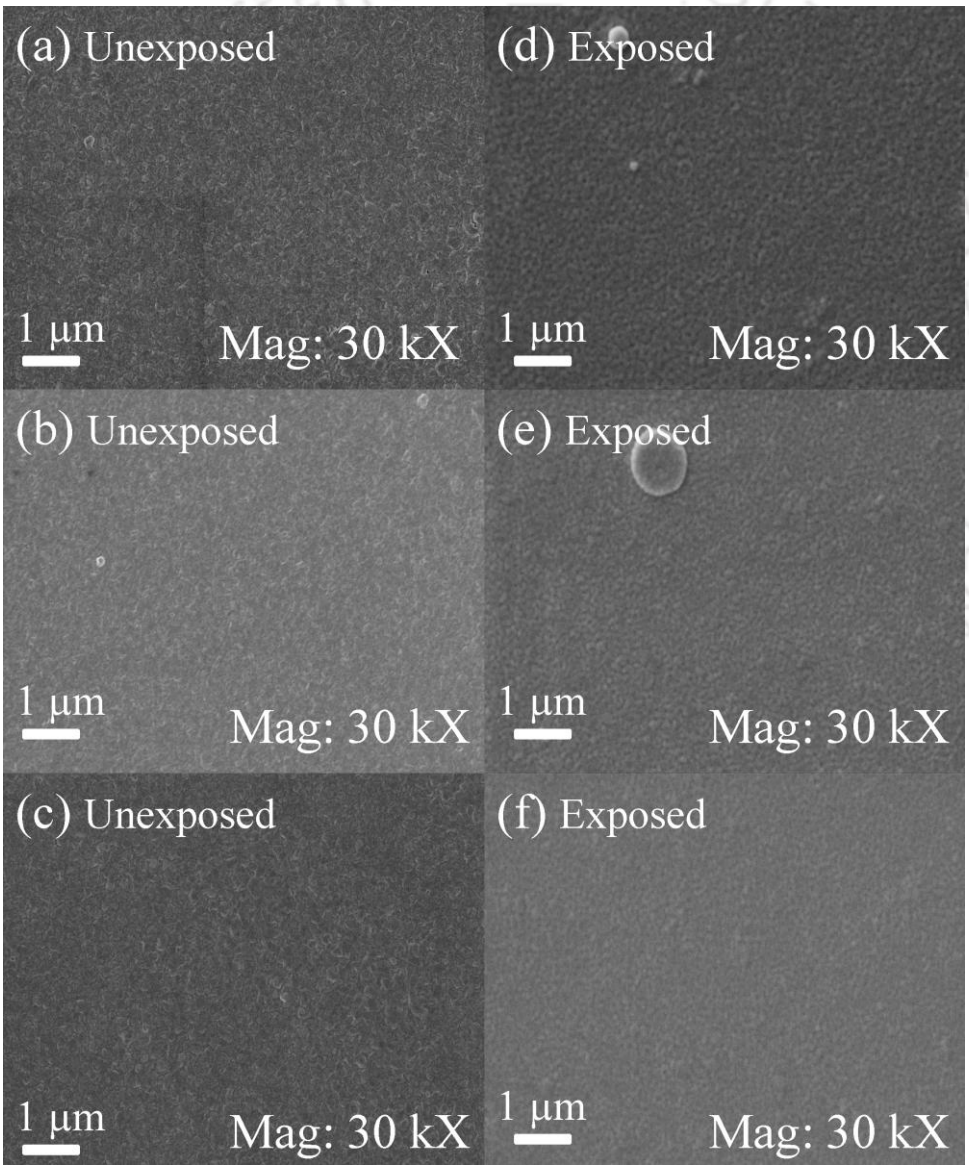

Figure 4.8. SEM image before D ion irradiation (a) Rh_{12}, (b) Rh_{13} and (c) Rh_{14} and that of after irradiation (d) Rh_{12}, (e) Rh_{13} and (f) Rh_{14} samples.

beam irradiation it was increased to ~ 17 nm, 15 nm and 13 nm for Rh_{12}, Rh_{13} and Rh_{14} samples, respectively, listed in table 4.2. The maximum changes in RMS surface roughness was observed for Rh_{12} sample which was irradiated by 10 keV D ion beam whereas the minimum change in RMS surface roughness was observed for Rh_{14} sample which was irradiated by 30 keV D ion beam.

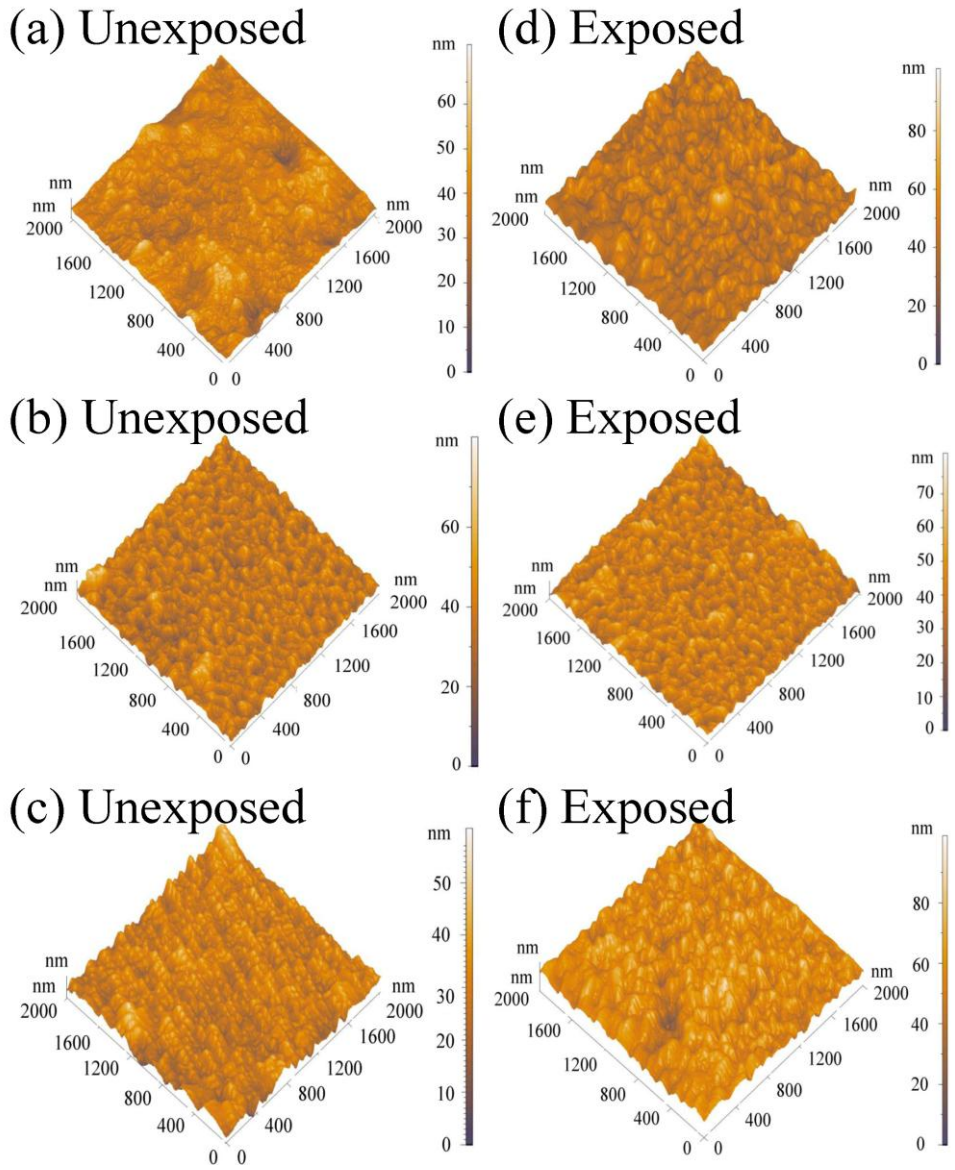

Figure 4.9. AFM image before D ion irradiation (a) Rh_{12}, (b) Rh_{13} and (c) Rh_{14} and that of after irradiation (d) Rh_{12}, (e) Rh_{13} and (f) Rh_{14} samples.

Table 4.2. Sample codes, ion energy (E), ion range (R_p), ion straggle (S_P), sputtering yield (Y), RMS surface roughness (σ), reflectivity (% R) with reference to aluminum standard mirror before and after irradiation of Rh thin film samples.

Sample Code	E (keV)	R_p (nm)	S_P (nm)	Y (atoms/ion)	σ		% R			
					before (nm)	after (nm)	λ = 20 μm		λ = 800 nm	
							before	after	before	after
Rh_{12}	10	70	34	0.0152	10	17 ↑	97	92 ↓	96	89 ↓
Rh_{13}	20	127	56	0.0082	10	15 ↑	98	93 ↓	96	90 ↓
Rh_{14}	30	180	72	0.0015	10	13 ↑	98	97 ↓	97	93 ↓

4.3.2 Effect of energy of D ion beam irradiation on the reflectivity of Rh thin films

The FIR and UV-visible reflectivity with reference to aluminum standard mirror of Rh_{12}-Rh_{14} samples before and after D ion beam irradiation is shown in figures 4.10(a) and 4.10(b), respectively. The percentage wise reduction in reflectivity of mirror-like Rh thin films in the FIR range, 2-20 μm, was ~ 5-7 % for 10 keV, 3-6 % for 20 keV and 1-2 % for 30 keV D ion beam irradiation. In the UV-visible range, 300-800 nm, the reduction in reflectivity was ~ 7-32 % for 10 keV, 5-26 % for 20 keV and 5-23 % for 30 keV D ion beam irradiation. In order to show the comparison of reflectivity before and after irradiation, the FIR and UV-visible reflectivity with reference to aluminum standard mirror at arbitrarily chosen wavelengths of 20 μm and 800 nm are listed in the table 4.2. The maximum change in reflectivity before and after irradiation at 20 μm was ~ 5 % and that of at 800 nm was ~ 7 % for Rh_{12} sample. The changes in reflectivity after irradiation were due to the cumulative effect of increase in RMS surface roughness and lattice damage into the film within the

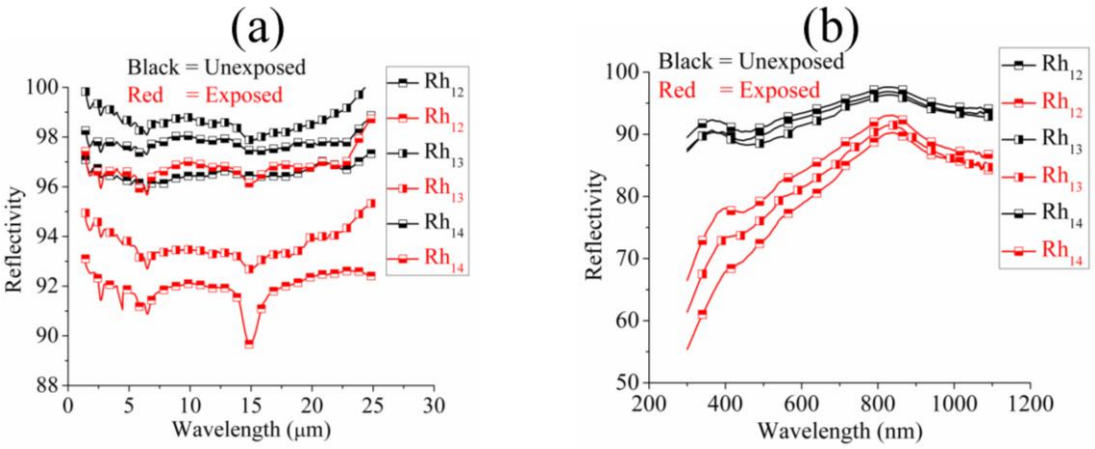

Figure 4.10. Specular reflectivity with reference to aluminum standard mirror of Rh_{12}-Rh_{14} samples (a) FIR range and (b) UV-visible range.

detection limit of optical photon. The observed changes in reflectivity due to 30 keV D ion beam irradiation were lower than that of the earlier report.[26] It was due to the higher particle flux with lower energy (~ 300 eV) in earlier report where post irradiation changes in surface morphology and lattice damage into the material close to its top surface are more significant. The change in reflectivity at a wavelength of 20 μm was less than that of at 800 nm. It was because, at higher wavelengths, in FIR range the reflectivity is less sensitive to 17 nm RMS surface roughness compared to that of at lower wavelengths in visible range.[165,173-175] The possibility of the formation of deuterium bonding with host lattice atoms[172], could also be responsible for the changes in post exposure reflectivity.

The reflectivity data before and after irradiation, listed in table 4.2, also confirmed that the change in reflectivity decreased with the increase of ion kinetic energy. Its probable mechanism is being discussed in the following subsection.

4.3.3 Ion range and ion straggle into Rh for 10, 20 and 30 keV D ion beam

To explain the effect of irradiation of 10, 20 and 30 keV D ion on the

properties of Rh mirror-like thin film samples, the damage parameters into Rh film due to D ion irradiation were also calculated numerically using TRIM Monte Carlo simulation code. Figure 4.11(a)-(c) shows the ion penetration depths into the Rh host lattice for 10, 20 and 30 keV D ions, respectively. The ion range (R_P), ion straggle

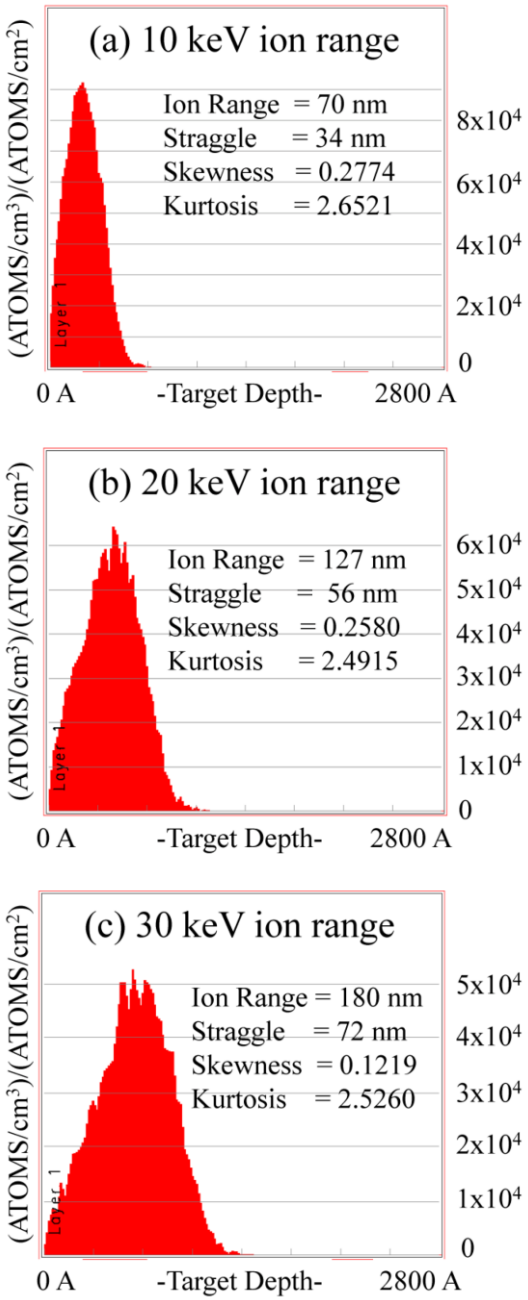

Figure 4.11. Ion penetration depth and ion straggle into Rh for (a) 10, (b) 20 and (c) 30 keV D ions.

(S_P) and sputtering yield (Y) were found to be 70 nm, 34 nm and 0.0152 atoms/ion for Rh_{12}; 127 nm, 56 nm and 0.0082 atoms/ion for Rh_{13} and 180 nm, 72 nm and 0.0015 atoms/ion for Rh_{14}, respectively, listed in table 4.2. The ion range and straggle increased with the increase of ion kinetic energy. The maximum ion penetration depth of ~ 180 nm was numerically obtained for 30 keV D ions. The thicknesses of Rh_{12}-Rh_{14} thin film samples were ~ 246 nm. Hence, most of the D ions were being stopped within the Rh thin film, causing lattice damage within Rh layer only. As the ion penetration depth was ~ 70 nm for 10 keV D ions, therefore, sample Rh_{12} suffered more lattice damage within photon penetration depth than that of Rh_{13} and Rh_{14} samples. Apart from lattice damage, surface sputtering was also playing an important role in affecting the optical reflectivity of the ion irradiated sample. At 10 keV D ion irradiation, the surface sputtering of the samples was more significant than that of 20 and 30 keV ion irradiation, listed in table 4.2. Therefore, RMS surface roughness of post exposure Rh_{12} samples was slightly more compared to that of other Rh_{13} and Rh_{14} samples, accordingly affecting the optical reflectivity.

4.4 Conclusions

The mirror-like W thin films of thicknesses ~ 32, 101, 216 and 326 nm were exposed with 8 keV D ion beam having particle flux ~ 8.9×10^{14} ions/cm^2/s for 30 minute. The post exposure FIR reflectivity of these W thin films was reduced by ~ 2 %, except 32 nm thick W thin film. Another set of W thin films of thickness ~ 326 nm were exposed with 10, 20 and 30 keV D ion beam having particle flux ~ 1.2×10^{14} ions/cm^2/s for 10 minute. The samples exposed with 10 keV D ions suffered maximum degradation in reflectivity, ~ 6 % at wavelength of 20 μm. The post exposed reflectivity of these samples, at 800 nm, was reduced by ~ 29 % for all

energies 10-30 keV. Overall post exposed FIR reflectivity of W thin films was above ~ 87 % with reference to aluminum standard mirror hence, it may be used as FM in FIR range for comparable time of exposure and energy of the ion beams.

Mirror-like Rh thin film of thickness ~ 246 nm were exposed with 10, 20 and 30 keV D ion beam having particle flux ~ 1.2×10^{14} ions/cm^2/s for 10 minute. The post exposure reflectivity for these Rh thin film samples was reduced by ~ 1-7 % in FIR range. The overall post exposure reflectivity with reference to aluminum standard mirror of these Rh thin films was above 90 % in FIR range. Therefore, it can be used as FM in FIR range for comparable time of exposure and energy of the ion beams.

Chapter 5

5. Design, fabrication and D ion beam irradiation on Rh/W/Cu multilayer thin film

The quality and sustainability of W and Rh thin film FMs, in the long term exposure of fusion plasma can be enhanced by making multilayer thin film of more than one element. The Rh/W/Cu multilayer thin film was designed and fabricated for FM application. Based on the damage parameters of D ions and the properties of Rh, W, Cu and SS, the thickness and coating sequence of individual layer was decided. The consecutive layers of multilayer thin films were fabricated at optimum deposition parameters, discussed in section 3.4 of chapter 3. The quality of Rh/W/Cu multilayer thin films was compared with single element W and Rh thin films. For this, the multilayer thin films were also irradiated with 20 and 30 keV D ions. The post irradiation effects on the quality of Rh/W/Cu multilayer thin film were investigated by subjecting them to XRD, SEM, AFM, FIR and UV-visible spectrometers.

5.1 Designing of Rh/W/Cu multilayer thin films

For multilayer thin films, thickness and sequence of the coating material play an important role. The thickness, coating sequence and the objectives of each layer in the proposed multilayer thin film of Rh/W/Cu are discussed below.

In designing multilayer thin film, the objective of bottom buffer layer is to

suppress lattice mismatch with SS substrate and to enhance thermal conductivity. For lattice mismatch, the atomic radii of Rh, W, Cu and the dominant constitutional elements of SS substrate, Fe are to be compared. The atomic radii of Rh, W, Cu and Fe are ~ 134, 139, 128 and 126 pm, respectively. The lattice mismatch in terms of atomic radius between Fe and Cu is minimum. Thermal conductivity of Rh, W, Cu and SS are ~ 150, 173, 401 and 80.4 $Wm^{-1}K^{-1}$, respectively. Therefore, Cu was suitable as bottom most buffer layer to suppress lattice mismatch as well as to dissipate heat developed due to ion irradiation on top and middle layer. A 40-80 nm thick Cu layer[176] should be sufficient for this bottom most buffer layer on SS substrate.

The objective of middle layer is to provide a cushion layer for energetic ions. The lattice damage of this cushion layer due to ion implantation is required to be minimal so as to provide better mechanical strength to its adjacent layers. The appropriate material and its coating thickness for middle layer was selected by investigating the damage parameters due to D ion beam irradiation at three different energies on Rh and W using TRIM simulation code. Ion range (R_p), ion straggle (S_p), sputtering yield (Y) and vacancies/ion (V_i) due to 10, 20 and 30 keV D ion irradiation on Rh and W are listed in table 5.1. Stopping distribution of 30 keV D ion in Rh and W as function of host lattice depth is shown in figures 4.7(c) and 4.11(c), respectively. The D ion penetration depth increased with the increase of ion kinetic energy. The penetration depth of 10 keV D ions was 70 nm in Rh and 62 nm in W, whereas that of at 30 keV, it was 180 nm in Rh and 153 nm in W. The maximum implantation of D ions and hence, lattice damage takes place around this range. Therefore, minimum thickness of the middle layer should be greater than ion penetration depth so as to stop

Table 5.1. Sample code, ion range (R_p), ion straggle (S_P), sputtering yield (Y) and vacancies/ion (V_i) due to 10, 20 and 30 keV D ion irradiation on Rh, W and Rh/W/Cu film.

D Ion energy (keV)	Material											
	Rh				W				Rh/W/Cu			
	R_p	S_p	Y	V_i	R_p	S_p	Y	V_i	R_p	S_p	Y	V_i
10	70	34	0.015	7.9	62	32	0.005	1.6	65	33	0.015	4.7
20	127	56	0.008	12.7	111	53	0.005	3.2	114	54	0.013	5.2
30	180	72	0.006	15.7	153	70	0.003	4.3	159	70	0.010	5.8

30 keV ions penetrating the bottom most layer and striking the substrate which may displace the substrate atoms and hence, spoil the film. It also acts as a cushion layer to reduce the lattice damage, supporting the top layer stable and maintaining the reflectivity. Numerically estimated sputtering yield data listed in table 5.1, shows the surface sputtering yield is less for W than that of Rh. It also showed surface sputtering yield decreased with the increase of ion kinetic energy. It was due to the fact that with the increase of kinetic energy, D ions penetrate deeper into the host lattice. Therefore, lattice damage was extended to inner layers of the host lattice. The vacancies/ion in

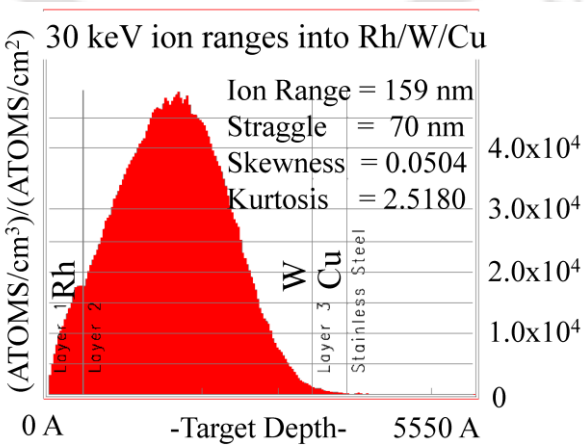

Figure 5.1. 30 keV D ion penetration depth into Rh/W/Cu multilayer thin film.

Rh and W were ~ 7.9 and 1.6 at 10 keV, ~ 12.7 and 3.2 at 20 keV and ~ 15.7 and 4.3at 30 keV, respectively, listed in table 5.1. The vacancies/ion in host lattice increased with the increase of ion kinetic energy. The vacancies/ion hence, lattice damage within stopping range of D ion in W was lower than that of Rh. Apart from these, W has better mechanical strength and higher melting temperature than that of Rh and Cu. Moreover, the W/Cu composite system has high thermal management.[177,178] Therefore, W was an appropriate choice for middle cushion layer.

The objective of top layer is to deal with the optical photons. Rh thin film mirror showed better overall reflectivity in FIR and UV-visible range than that of W thin film mirror and hence, it was selected as top layer. The thickness of this layer was proposed to be limited within the optical penetration depth of photon. The optical penetration depth of photons in visible-FIR range is ~ 20-40 nm. Hence, the thickness of top layer was limited to 20-40 nm. The minor lattice damage, ion trap within this range is unavoidable. This layer is almost transparent for majority of 10-30 keV D ions as the D ion penetration depths ~ 70 to 180 nm was larger than the thickness of Rh layer.

The stopping distribution of 30 keV D ions in Rh/W/Cu as a function of host lattice depth is shown in figure 5.1. The ion penetration depth, ion straggle, sputtering yield and vacancies/ion of 10, 20 and 30 keV D ions in Rh/W/Cu multilayer is listed in table 5.1. At 30 keV, vacancies/ion was ~ 5.8 for Rh/W/Cu multilayer which was close to that of W and ~ 3 order magnitudes lower than that of Rh. The calculation showed that the durability of Rh/W/Cu composition is comparable to W and it is better than that of Rh.

5.2 Fabrication and characterization of Rh/W/Cu multilayer thin films

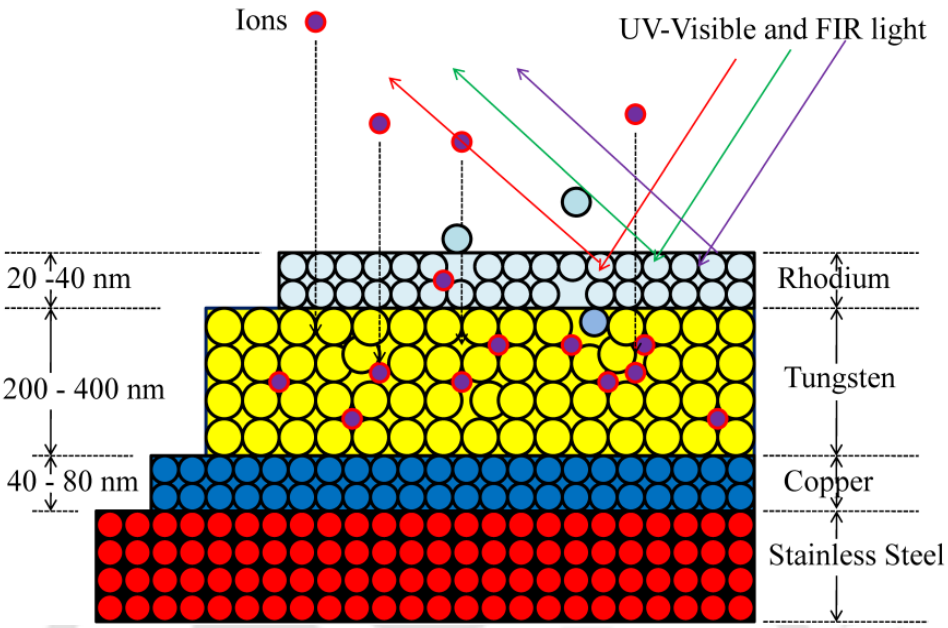

Figure 5.2. Schematic diagram of multilayer FM.

Based on the above discussions, two samples M_1 and M_2 of Rh/W/Cu multilayer thin films were fabricated as listed in table 5.2. The schematic diagram of Rh/W/Cu multilayer thin film on SS substrate is shown in figure 5.2. Each layer of these multilayer thin films was deposited under respective optimum deposition parameters in the spherical ablation chamber which was evacuated with turbo molecular pump. Two samples, M_1 and M_2 were prepared. The duration of depositions of each layer in M_1 and M_2 samples are listed in table 5.2. These samples were annealed at 500 °C under same deposition He pressure ~ 1.0 mbar for 60 minute and ramp cooled at 1.6 °C/minute from 500 to 100 °C. Afterwards, the heater was switched off and allowed to cool down from 100 °C to room temperature on its own.

The cross-sectional SEM image of the samples M_1 and M_2 are shown in figures 5.3(a) and 5.3(b). Both the images clearly showed all the three different layers

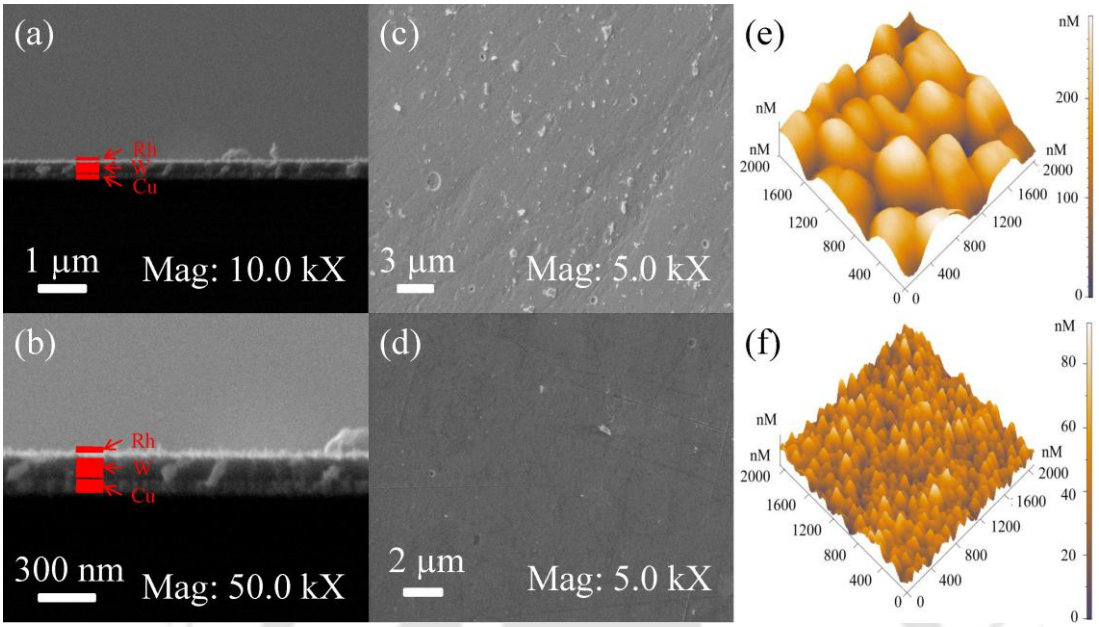

Figure 5.3. Cross-sectional image of (a) M_1, (b) M_2; top surface SEM image of (c) M_1, (d) M_2; AFM image of (e) M_1 and (f) M_2, respectively.

Table 5.2. Sample codes, coating material, duration of deposition (T_d), thickness (t), RMS surface roughness (σ), FWHM of Rh(111), W(110) XRD peaks and reflectivity (% R) with reference to aluminum standard mirror.

Sample code	Material	T_d (minute)	t (nm)	σ (nm)	FWHM	% R	
						λ= 20 μm	λ= 800 nm
M_1	Rh/W/Cu	20/60/30	80/400/200	57	0.6° - Rh(111) 0.5° - W(110)	94	74
M_2	Rh/W/Cu	06/30/10	25/191/83	14	0.6° - Rh(111) 0.4° - W(110)	96	99

of multilayer thin film. Measured thickness of the individual Rh, W and Cu layer was ~ 80, 400, 200 nm for sample M_1 and ~ 25, 191 and 83 nm for that of sample M_2, respectively. The cumulative thickness of samples M_1 and M_2 was sufficiently larger than ion penetration depth, figure 5.1. Hence, the penetration of 10-30 keV D ions to the substrate was expected to be negligible.

The top surface SEM image of M_1 sample, figure 5.3(c), was relatively rough compared to that of M_2 sample, figure 5.3(d). The AFM image of samples M_1 and M_2 as shown in figures 5.3(e) and 5.3(f), also confirmed the same. The top layer RMS surface roughness of samples M_1 and M_2 was ~ 57 and 14 nm, respectively. At higher thickness, the grain size of the film is larger compared to that of thinner film[179] and hence, RMS surface roughness of sample M_1 was larger than that of sample M_2.

The XRD pattern of samples M_1 and M_2 is shown in figures 5.4(a) and 5.4(b), respectively. The XRD peaks of Rh(111) and Rh(200) plane from top Rh layer, W(110) and W(200) plane from middle W layer could be identified along with weak SS substrate XRD peaks. The inset of figures 5.4(a) and 5.4(b) shows the enlarged view of Gaussian fitted Rh (111) and W(110) XRD peak. Measured FWHM from Gaussian fitted prominent XRD peak of Rh(111) and W(110) plane are listed in table 5.2. The FWHM of Rh(111) XRD peak for both the samples M_1 and M_2 was ~ 0.6° and for that of W(110) XRD peak were ~ 0.5° and 0.4°, respectively. The FWHM of W(110) XRD peak was less than that of W_{13} thin film sample, ~ 0.7° listed in table 3.6. It was due to the presence of bottom Cu buffer layer which reduced the lattice mismatch and stress into the film. The clear signature of Cu XRD peak for the samples M_1 and M_2 could not be resolved in figures 5.4(a) and 5.4(b). It was due to superimposition of SS substrate XRD peak which is close to that of the weak Cu(111) XRD peak. To ensure this, a Cu thin film of thickness ~ 200 nm was deposited under same deposition parameters to that of bottom Cu layer of M_1 multilayer thin film on SS substrate. To resolve Cu peak distinctly, a slow scan was recorded around this peak position at a step of 0.02°, shown in figure 5.5, instead of 0.05° for that of figures 5.4(a) and 5.4(b). It clearly showed a well resolved Cu(111) XRD peak at

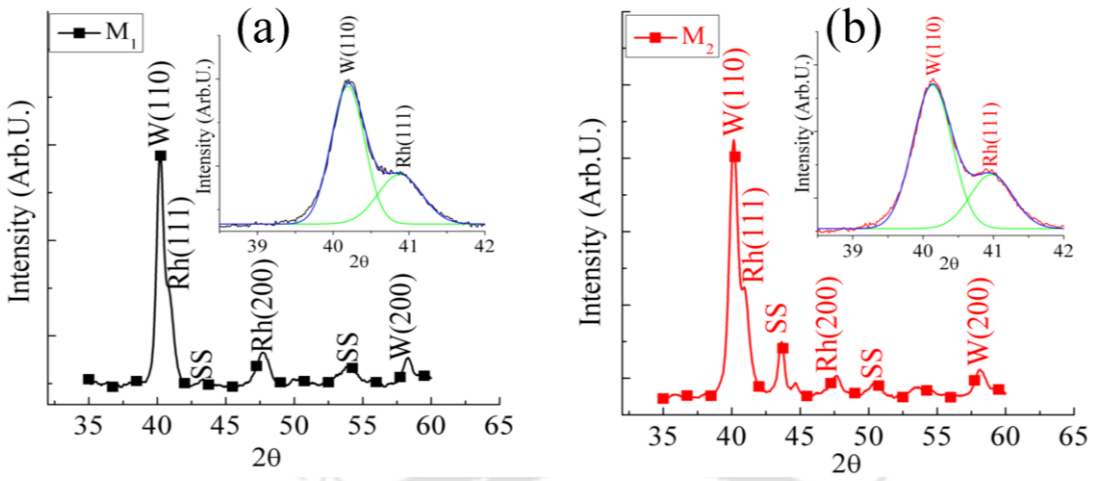

Figure 5.4. XRD pattern of (a) M_1 and (b) M_2 samples.

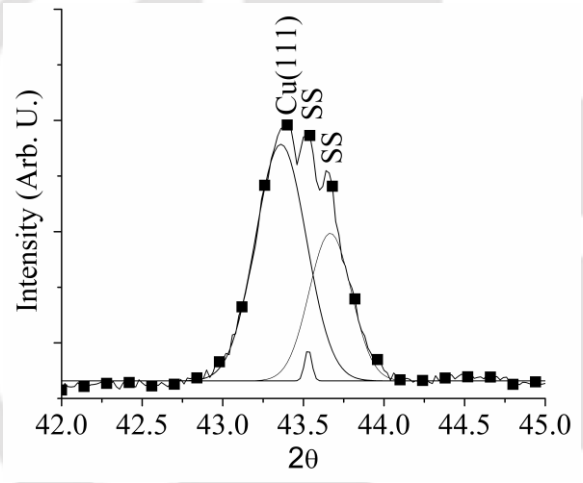

Figure 5.5. XRD pattern of Cu thin film on SS substrate.

~ 43.4° along with the SS substrate XRD peaks. The FWHM of Gaussian fitted XRD peak of Cu(111) was ~ 0.3°, which is comparable to that of the Cu thin film deposited by sputtering technique.[180]

Specular FIR and UV-visible reflectivity with reference to aluminum standard mirror of the samples M_1 and M_2 are shown in figures 5.6(a) and 5.6(b), respectively. The reflectivity of both the samples with reference to aluminum standard mirror at wavelength of 20 µm and 800 nm are listed in table 5.2. At 20 µm, the samples M_1

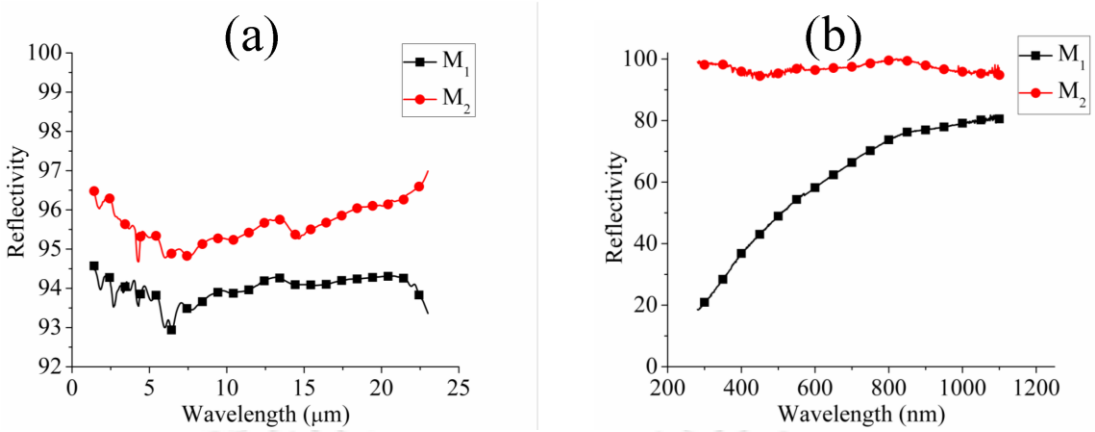

Figure 5.6. Specular reflectivity with reference to aluminum standard mirror of the sample M_1 and M_2 (a) FIR range and (b) UV-visible range.

and M_2 showed ~ 94 % and 96 %, whereas at 800 nm showed ~ 74 % and 99 % reflectivity, respectively. The reflectivity of the sample M_1 in the FIR range of 2-20 μm was ~ 94 %, whereas in UV-visible range it varied from ~ 20-70 %. The FIR reflectivity of the sample M_2 in the range, 2-20 μm was varying from ~ 95-96 % and that of in UV-visible range, 300-800 nm, it varied from ~ 94-99 %. The overall reflectivity of the sample M_2 was higher than that of M_1 and it approached to the single element Rh_6 sample. Low reflectivity of the sample M_1 was due to its poor surface quality.

Nano hardness of M_1 sample was measured by nano indentation. The loading displacement curve is shown in figure 5.7. Maximum indentation load was set to 0.5 mN and the corresponding indentation depth was ~ 69 nm, confirmed in figure 5.7. The indentation was not extended to the middle W layer as the thickness of the top Rh layer was higher than that of the indentation depth. The nano hardness of M_1 sample was found to be ~ 5.0 GPa. In literature, the reported bulk Rh hardness is ~ 1.3 GPa.[181] The presence of middle W layer could be responsible for increase in hardness.

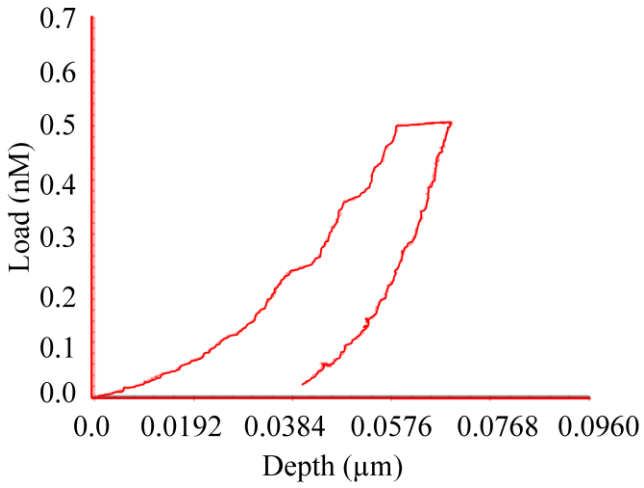

Figure 5.7. Loading displacement curve of M_1 sample for measuring nano hardness.

5.3 Effect of D ion beam irradiation on Rh/W/Cu multilayer thin film

In order to study the D ion irradiation effect on Rh/W/Cu multilayer thin film, two samples, M_3 and M_4 were fabricated by PLD technique for D ion beam irradiation using the same parameters as that of M_2. The Rh/W/Cu multilayer thin film samples M_3 and M_4 were exposed by 20 and 30 keV D ion beam for ~ 10 minute having particle flux ~ 1.2×10^{14} ions/cm^2/s. The 10 minute exposure of this particle flux corresponded to an ion fluence ~ 7.8×10^{16} ions/cm^2.

5.3.1 Surface characterization of W thin films before and after D ion beam exposure

The SEM images of the samples M_3 and M_4 before and after irradiation are shown in figures 5.8(a)-(b) and 5.8(c)-(d), respectively. The surface of both the samples was uniform. The post exposure SEM images were devoid of formation of any craters or blisters. The AFM images of samples M_3 and M_4 before and after irradiation are shown in figures 5.9(a)-(b) and 5.9(c)-(d), respectively. AFM images confirmed that the columnar structures were intact on the surface even after

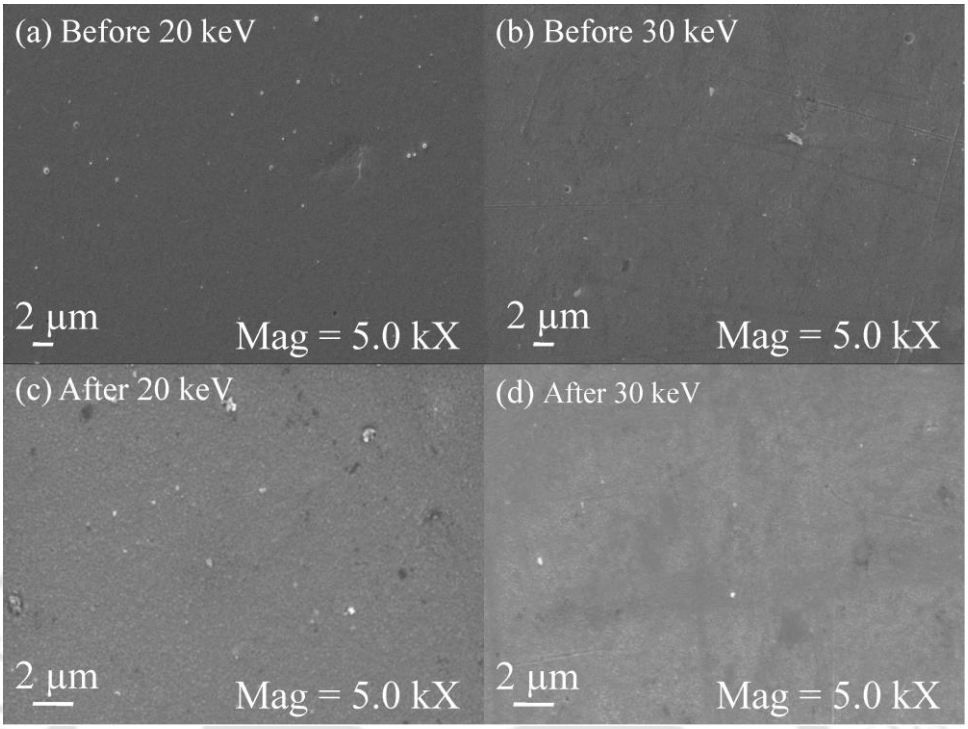

Figure 5.8. SEM image before irradiation (a) M_3, (b) M_4 and that of after irradiation (c) M_3 and (d) M_4, respectively.

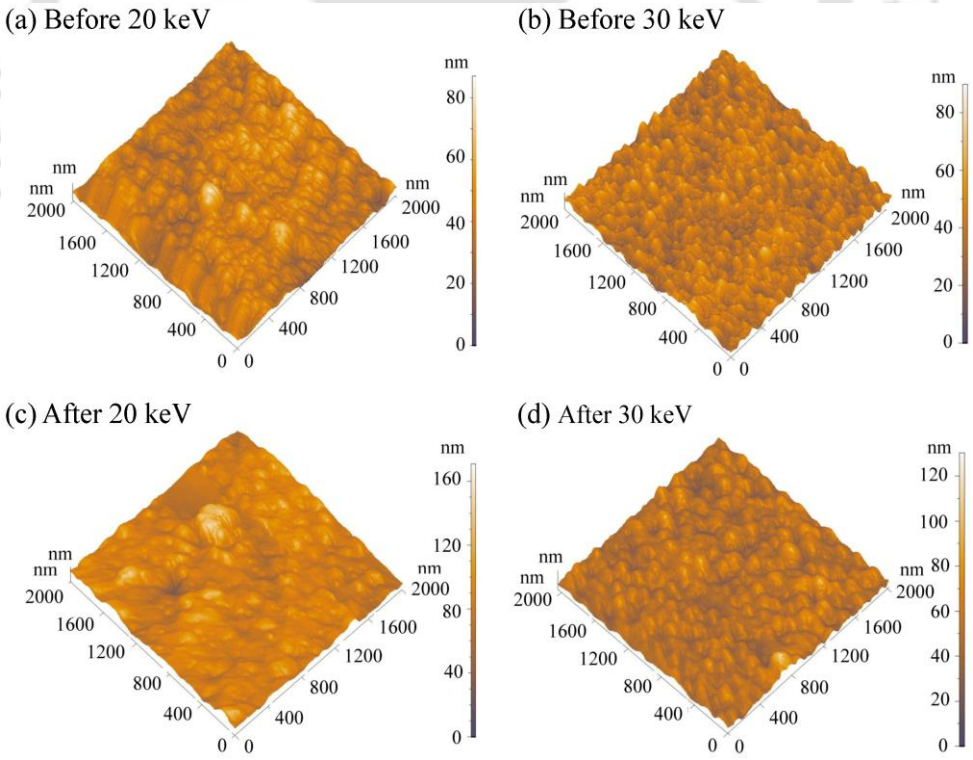

Figure 5.9. AFM image before irradiation (a) M_3, (b) M_4 and that of after irradiation (c) M_3 and (d) M_4, respectively.

Table 5.3. Sample codes, ion energy (E), RMS surface roughness (σ), FWHM of Rh(111), W(110) XRD peak and reflectivity (% R) with reference to aluminum standard mirror.

Sample code	E (keV)	σ (nm)		% R			
		before	after	λ = 20 μm		λ = 800 nm	
				before	after	before	after
M_3	20	14	18↑	95	93↓	95	90↓
M_4	30	12	15↑	96	95↓	99	96↓

irradiation. The RMS surface roughness measured from AFM images of the samples M_3 and M_4 before and after irradiation is listed in table 5.3. The RMS surface roughness of the samples M_3 and M_4 were ~ 14 nm and 12 nm before irradiation and that of after irradiation it was increased to ~ 18 nm and 15 nm, respectively. The change in RMS surface roughness was ~ 4 nm and 3 nm due to 20 keV and 30 keV D ion beam irradiation, respectively.

5.3.2 Effect of energy of D ion beam irradiation on the reflectivity of Rh/W/Cu multilayer thin films

Specular FIR and UV-visible reflectivity with reference to aluminum standard mirror of the samples M_3 and M_4 before and after irradiation are shown in figures 5.10(a) and 5.10(b), respectively. The reflectivity at wavelength of 20 μm and 800 nm with reference to aluminum standard mirror before and after irradiation are listed in table 5.3. Before irradiation of 20 keV D ion beam, the sample M_3, showed ~ 95 % reflectivity both at wavelength of 20 μm and 800 nm and that of after irradiation it was reduced to ~ 93 % at 20 μm and ~ 90 % at 800 nm. The sample M_4 showed ~ 96 % and 99 % at 20 μm and 800 nm, before 30 keV D ion beam irradiation and that of

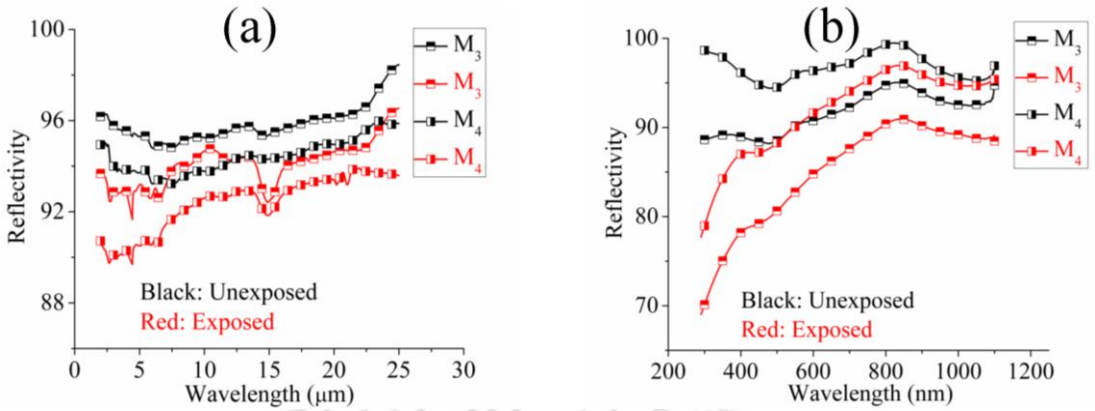

Figure 5.10. Specular reflectivity with reference to aluminum standard mirror of the samples M_3 and M_4 before and after irradiation (a) FIR range and (b) UV-visible range.

after irradiation, it was reduced to ~ 95 % at 20 μm and ~ 96 % at 800 nm. The reflectivity of the sample M_3 and M_4 degraded by ~ 1-4 % in FIR range, 2-20 μm and ~ 3-20 % for that UV-visible range, 300-800 nm due to 20 and 30 keV D ion beam irradiation. The reduction of optical reflectivity was due to cumulative effect of increase in RMS surface roughness, trapping of D ions into the host lattice and lattice damage within the penetration depth of optical photons. The change in reflectivity, in FIR range was lower than that of in UV-visible range. Theoretically, at wavelength of 800 nm Bennett's formula shows a reduction of reflectivity ~ 2 % and 1 % due to increase of surface roughness from 14 nm to 18 nm and 12 nm to 15 nm, respectively. At wavelength of 20 μm, the same formula shows a negligible change in reflectivity. The changes in reflectivity after D ion beam irradiation can be explained in terms of damage parameters, discussed in the following subsection.

5.3.3 Ion range and ion straggle into Rh/W/Cu for 20 and 30 keV D ion beam

The ion range and straggle into the multilayer thin film due to 20 keV and 30 keV are shown in figures 5.11(a) and 5.11(b). The ion range (R_p), straggle (S_p),

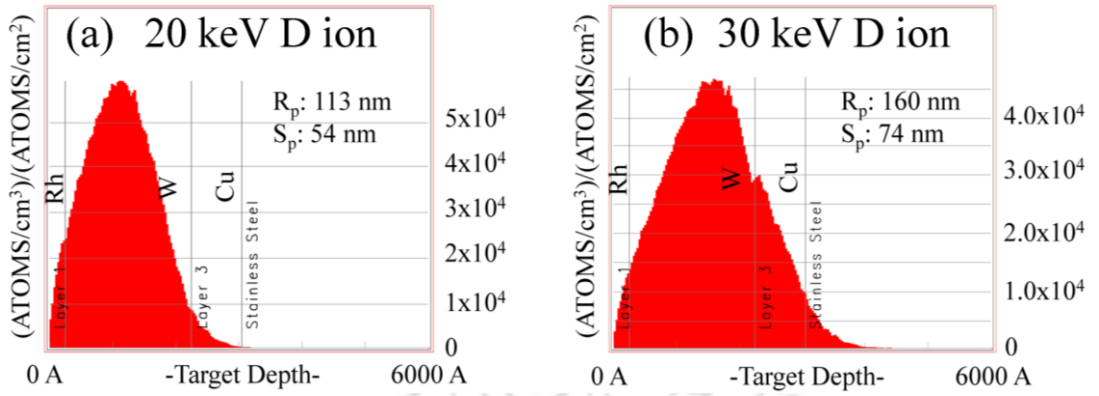

Figure 5.11. D ion penetration depth into Rh/W/Cu multilayer for (a) 20 keV and (b) 30 keV.

Table 5.4. Ion range (R_p), straggle (S_p), sputtering yield (Y) and vacancies/ion (V_i) due to 20 and 30 keV D ion irradiation on Rh/W/Cu film.

Ion energy (keV)	R_p (nm)	S_p (nm)	Y (atoms/ion)	V_i
20	113	54	0.013	5.2
30	160	74	0.010	5.8

sputtering yield (Y) and vacancies/ion (V_i) due to 20 and 30 keV D ion irradiation on multilayer Rh/W/Cu thin films are listed in table 5.4. It showed that the ion penetration in multilayer thin film increased with the increase of D ion kinetic energy. At 20 keV, the penetration of D ions into the substrate was negligible, as shown in figure 5.11(a), whereas at 30 keV, some of the D ions were extended into the substrate as shown in figure 5.11(b). Numerically calculated ion ranges were ~ 113 nm and 160 nm for 20 keV and 30 keV D ions, respectively. The numerical calculation also showed, the sputtering yield (Y) and vacancies/ion (V_i) were almost same for 20 and 30 keV D ion beam irradiation. The density of implanted D ions as well as lattice damage, as function of target depth within 10-20 nm was higher for 20 keV than that of 30 keV D ions irradiation. The optical photon penetration depth is ~ 10 nm to 20

nm for typical metal. Due to this, the optical reflectivity degradation by 20 keV D ion beam irradiation was slightly higher than that of 30 keV.

5.4 Conclusions

Rh/W/Cu multilayer thin film was designed and fabricated for FM application. Based on the damage parameters and the properties of Rh, W, Cu and SS, two Rh/W/Cu multilayer samples M_1 and M_2 of thicknesses ~ 80/400/200 nm and 25/191/83 nm were designed and fabricated. Prominent XRD peaks of Rh(111), W(110) and Cu(111) plane could be identified in the XRD pattern of M_1 and M_2 samples. The FWHM of W(110) XRD peak of M_1 and M_2 samples was reduced to ~ 0.5° and 0.4° from 0.7° of single element W thin film sample. It was due to the presence of bottom Cu buffer layer which reduced the lattice mismatch and stress into the successive layers in the multilayer films. The RMS surface roughness of the samples M_1 was ~ 57 nm which was quite larger than that of the sample M_2. This results in the higher overall reflectivity of M_2 sample than that of M_1 sample. The reflectivity with reference to aluminum standard mirror of M_2 sample was ~ 96 % at wavelength of 20 μm and 99 % at 800 nm. The reflectivity of M_2 sample was better than W thin film sample and approached to that of the Rh thin film sample.

To ensure the sustainability of Rh/W/Cu multilayer thin film in fusion reactor like harsh environment, another two samples M_3 and M_4 of same thickness ~ 25/191/83 nm were fabricated and exposed to 20 and 30 keV D ion beams for 10 minute having particle flux ~ 1.2×10^{14} ions/cm^2/s. The SEM images of the exposed samples confirmed the surface of exposed samples were free from blisters formation and eruption of the film from the substrate. The RMS surface roughness of the films increased from ~ 14 nm to ~ 18 nm for 20 keV and ~ 12 nm to ~ 15 nm for 30 keV of

D ion beam irradiation. Due to the increase in RMS surface roughness, these multilayer samples showed ~ 1-4 % reduction of reflectivity in FIR range and ~ 3-20 % in that of UV-visible range. The degradation of optical reflectivity due to 20 keV D ion beam irradiation was slightly higher than that of 30 keV. It was due to the fact that the lattice damage within optical penetration depth of photon was higher for 20 keV than that of 30 keV. The degradation in UV-visible reflectivity of multilayer thin film was less compared to that of single element W thin films. Based on the damage parameters and reflectivity degradation after D ion beam irradiation, it can be concluded that multilayer thin film may offer a better alternative to the single element thin film FM in FIR range where the ion energy and fluence are comparable to that of the present case.

Chapter 6

6. Rh and Rh/W/Cu thin films on 50 mm diameter SS substrate

In fusion reactor, large amount of radiation from the fusion plasma is required to be collected for better reliability of optical signals. The FMs are accordingly required of large sizes having diameter ~ 25 mm to 100 mm to collect large amount of radiation.[1,28,30] The pulsed laser deposited samples discussed in the previous chapters were of size 10 mm × 10 mm or 10 mm diameter. Therefore, PLD setup was modified to increase the surface area of single layer Rh and multilayer Rh/W/Cu thin film to 50 mm diameter. The process optimization to achieve uniformity of deposition as estimated from fringe visibility is presented in this chapter.

6.1 Experimental setup

The large area coating using conventional PLD technique is difficult due to non homogenous distribution of laser ablated particle flux.[131,141] Therefore, the conventional PLD technique was modified by incorporating a substrate rastering stage in place of a fixed substrate holder to obtain the uniform deposition on 50 mm diameter of SS substrate. The substrate rastering stage was enabled to translate the substrate along X-axis as well as to rotate it along the direction of LIP expansion simultaneously. Photograph of the substrate rastering stage is shown in figure 6.1.

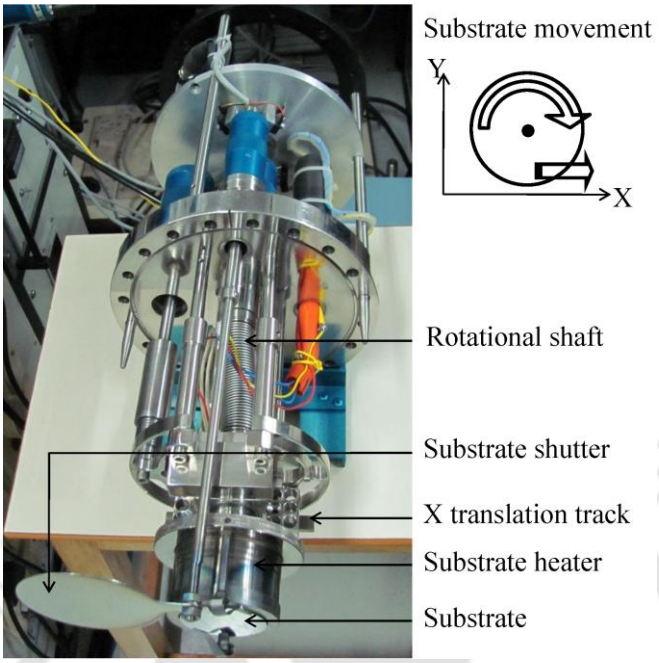

Figure 6.1. Photograph of substrate rastering stage.

In this, the maximum possible linear translation of the substrate was 25 mm with 360° rotation at each point on the X-axis. During deposition, the 50 mm diameter SS substrate was translated horizontally to 20 mm at a speed of ~ 8 mm/s and was simultaneously rotated 360° at speed of ~ 52° /s, figure 6.1.

The single layer Rh and multilayer Rh/W/Cu thin film were deposited on highly polished 50 mm diameter SS substrate under optimum deposition parameters, section 3.4 of chapter 3, in the spherical ablation chamber which was evacuated with turbo molecular pump as described in section 2.2 of chapter 2. After deposition, the samples were annealed at 500 °C for ~ 1 hour and thereafter slowly cooled at cooling rate ~ 1.6 ^{o}C/minute to 100 °C under He environment so as to suppress any stress that may develop in the film due to sudden cooling. Afterwards, the heater was switched off and allowed to cool down from 100 °C to room temperature on its own, in He ambient.

6.2 Optimization of substrate rastering stage

The initial optimization of the substrate rastering stage has been carried out by a few trial depositions of W thin films on 6 mm thick, 50 mm diameter glass substrate and thereafter observing background object through it. When the coating was uniform and sufficiently thick, the deposited film was completely opaque and no background object could be seen through it. When the coating was not uniform and/or of low thickness, a semitransparent or transparent film was formed allowing background object to be seen through it.

Three conditions were explored to optimize the lateral position of the substrate in a plane parallel to and ~ 3 cm apart from target in the substrate rastering stage. In the first case, W thin films were deposited by keeping the central axis of LIP plume close to the center of glass substrate. Photograph of this film, figure 6.2(a), shows a non uniform deposition around the circumference of glass substrate. In the

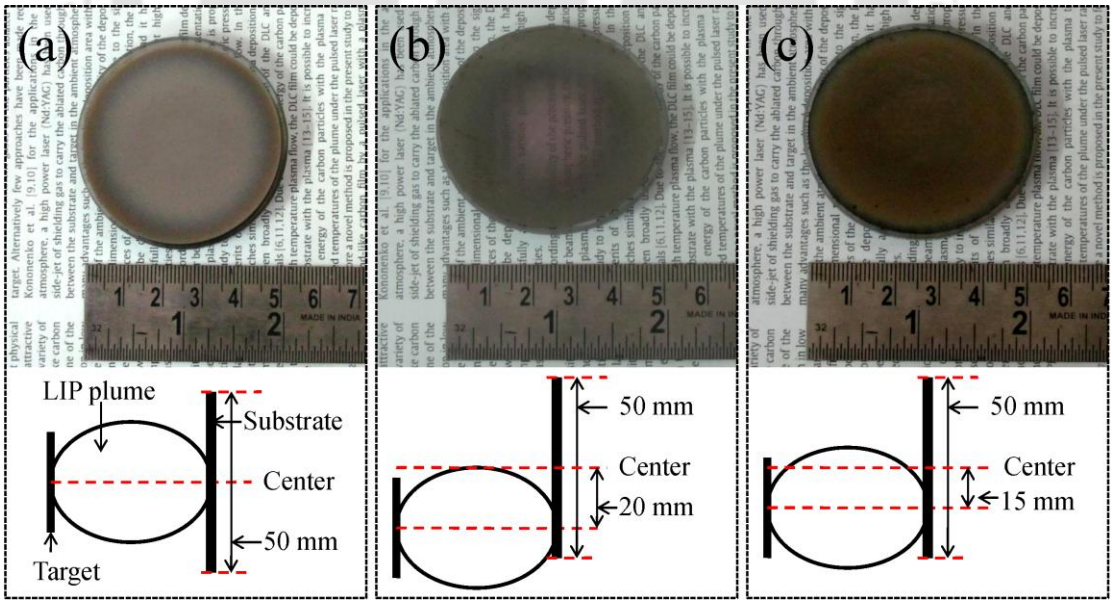

Figure 6.2. Photographs of W thin films, central axis of plasma plume align (a) close to the center of the substrate, (b) ~ 20 mm below the center of the substrate and (c) ~ 15 mm below the substrate.

second case, W thin films were deposited by keeping the central axis of plasma plume at ~ 20 mm below, from the centre of glass substrate. A non uniform deposition around center was observed in this case, figure 6.2(b). In the third case, W thin films were deposited by keeping the central axis of plasma plume at ~ 15 mm below from the center of glass substrate. The photograph of this film, figure 6.2(c), confirmed uniform deposition throughout the substrate. The dark ring on the circumference of this film was due to the circular substrate holding clip. Accordingly, the parameters obtained in third case were considered as optimum for substrate rastering stage for depositing Rh single layer and Rh/W/Cu multilayer thin films on 50 mm diameter SS substrate.

6.3 Characterization of Rh and Rh/W/Cu thin films

Figure 6 shows the photographs of Rh single layer thin film (figure 6.3(a)) and Rh/W/Cu multilayer thin film (figure 6.3(b)) on 50 mm diameter SS substrate. The thickness of Rh single layer thin film was ~ 120 nm and that of individual layers of Rh/W/Cu multilayer thin films were ~ 25 nm, 180 nm and ~ 30 nm, respectively when deposited on 50 mm diameter SS substrate under optimized conditions. The

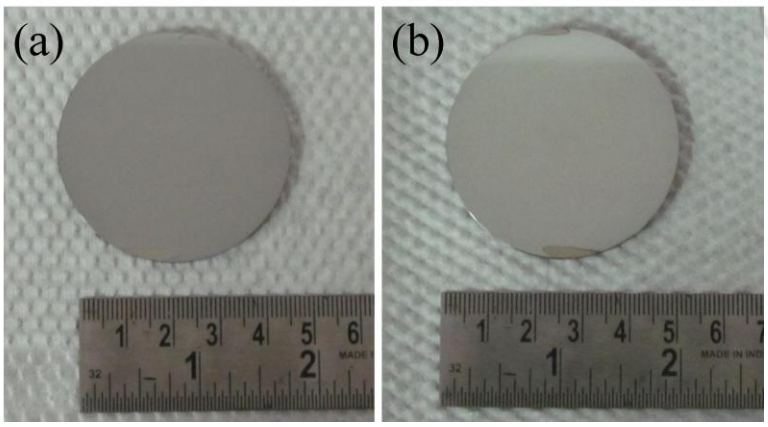

Figure 6.3. Photographs of (a) single layer Rh mirror and (b) multilayer mirror Rh/W/Cu thin film on 50 mm SS substrates.

deposition rates were ~ 1 nm/minute, 2 nm/minute and 3 nm/minute for Rh, W and Cu, respectively. The present deposition rates of the corresponding film of Rh, W, Cu deposited by using substrate rastering stage were lower than that of the films deposited on a fixed substrate holder, chapter 3, due to the large area deposition of former.

6.3.1 Fringe visibility of 50 mm Rh and Rh/W/Cu thin film mirrors

The interference pattern before and after deposition of single layer Rh and multilayer Rh/W/Cu thin films on the corresponding SS substrates are shown in figures 6.4(a)-(b) and figure 6.4(c)-(d), respectively. The interference patterns of uncoated SS substrates (before deposition of thin films), shown in figures 6.4(a) and 6.4(c), confirmed that the substrate surface were optically flat. After deposition of thin films, no significant change in the interference pattern was observed. The interference

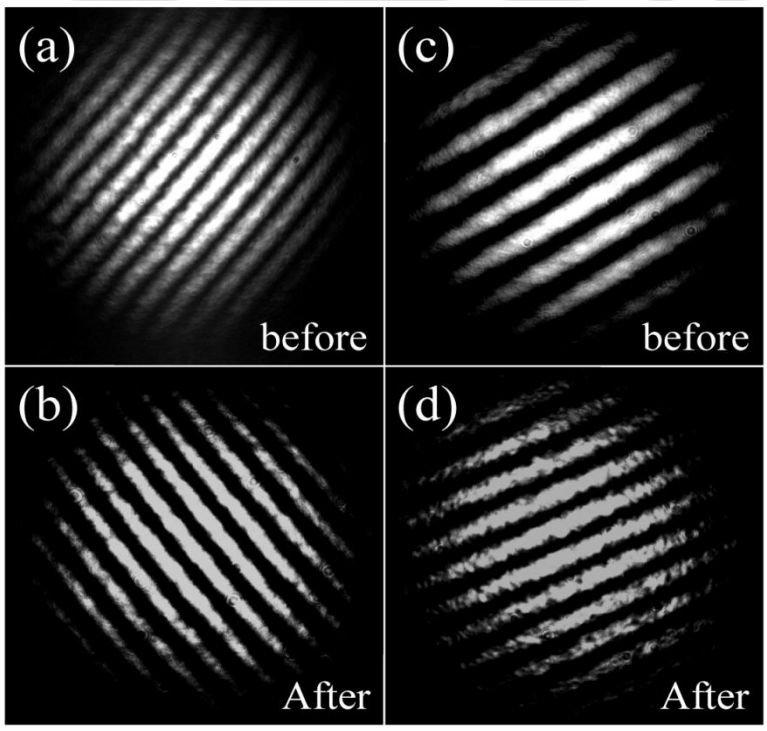

Figure 6.4. Interference pattern (a) 50 mm SS substrate, (b) Rh single layer thin film, (c) 50 mm SS substrate and (d) Rh/W/Cu multilayer thin film, respectively.

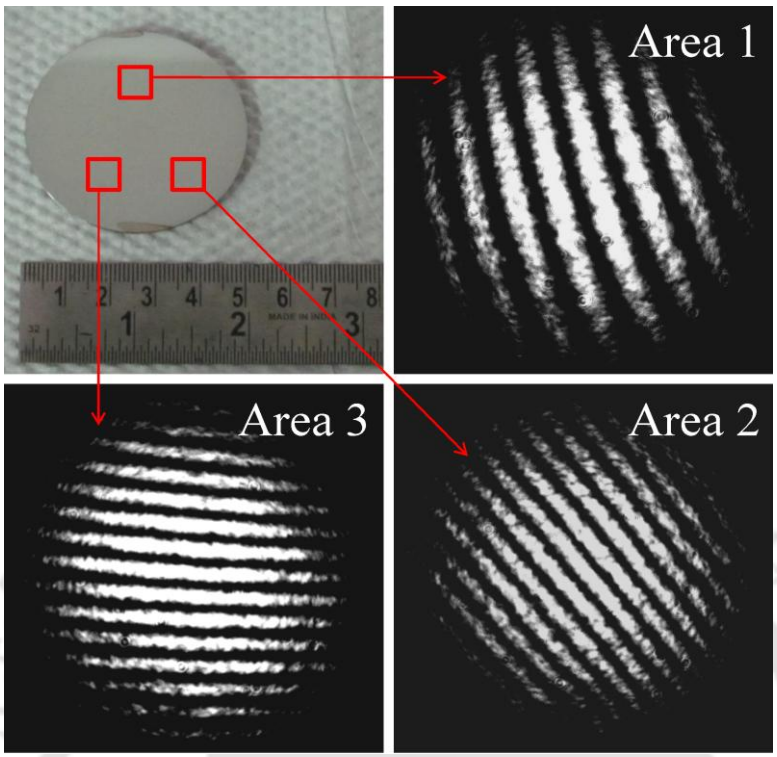

Figure 6.5. Interference patterns from three different areas of Rh/W/Cu multilayer thin film.

fringe continued to be distinct and straight in the interference pattern of both single layer Rh and multilayer Rh/W/Cu thin films. The fringe visibility of both, single layer Rh and multilayer Rh/W/Cu thin films, was ~ 0.8 whereas the fringe visibility of the standard mirror in Michelson interferometer used for measurement was ~ 0.9. The observed straight interference pattern confirmed the uniform deposition of single and multilayer thin films on 50 mm diameter SS substrate and absence of any curvature on the film surface.

The interference patterns from three different areas of multilayer thin film of Rh/W/Cu shown in figure 6.5 which are again seen to be consisting of distinct, straight and parallel interference fringes, confirming the uniform deposition over a diameter of 50 mm substrate.

6.4 Conclusions

Rh single and Rh/W/Cu multilayer thin films were uniformly deposited on highly polished 50 mm diameter SS substrate by modifying conventional PLD technique by replacing fixed substrate holder with a substrate rastering stage. After optimization of the movement of the substrate stage, both single and multilayer thin films were deposited by translating the substrate linearly 20 mm at speed of ~ 8 mm/s and rotating 360° at speed of 52° /s with central axis of plasma plume at ~ 15 mm below the center of the substrate. The thickness of Rh single layer and Rh/W/Cu multilayer thin films was observed to be of the order of ~ 120 nm and ~ 25/180/30 nm, respectively. The deposition rates were ~ 1 nm/minute, 2 nm/minute and 3 nm/minute for Rh, W and Cu, respectively. The uniformity of deposition was confirmed by distinct, straight and parallel interference fringes both for Rh single layer and Rh/W/Cu multilayer thin films.

Chapter 7

7. Conclusions

Mirror-like highly reflecting Mo, W and Rh thin films were fabricated by Pulsed Laser Deposition (PLD) technique for First Mirror (FM) application in fusion reactor. An experimental PLD setup was assembled to fabricate these thin films. The deposition parameters were optimized to obtain the mirror-like quality of the thin films on Stainless Steel (SS) substrate via PLD technique. A Michelson interferometer setup was assembled to measure the thickness, fringe visibility and curvature present in the thin films. The PLD thin films were subjected to X-ray Diffractometer (XRD) for identification of crystal-structure, Scanning Electron Microscope (SEM) and Atomic Force Microscope (AFM) for surface quality analysis, Stylus surface profilometer for thickness measurement, nano indentation for hardness measurement and Far-Infrared (FIR) and Ultraviolet (UV)-visible spectrometers for reflectivity measurement.

It was observed that the optical quality of oxygen contaminated thin films was very poor. The film adhesion to the substrate was poor for oxygen contaminated films. Such films got detached from the substrate within a couple of weeks after deposition. To reduce oxygen contamination, the ablation chamber was conditioned by baking at 70-80 °C for ~ 14-15 hour while evacuation, prior to deposition. PLD thin films of Mo, W and Rh were deposited as a function of laser fluence, substrate

temperature, target-substrate distance and Helium (He) ambient gas pressure. The overall optimized parameters for mirror-like Mo, W and Rh thin films were ~ 2 J/cm^2 laser fluence, ~ 500 °C substrate temperature, ~ 3 cm target-substrate distance and ~ 1.0 mbar He ambient pressure. The thickness of Mo, W and Rh thin film deposited for 60 minute under these optimum parameters was more than 245 nm.

Mo thin film sample deposited under optimum parameters showed prominent XRD peak of Mo(110) plane with Full Width at Half Maximum (FWHM) of 0.6°, reflectivity ~ 97-99 % in wavelength range of 2-20 μm and that of ~ 75-83 % in wavelength range of 300-800 nm with reference to aluminum standard mirror. W thin film sample deposited under optimum parameters showed prominent XRD peak of W(110) plane with FWHM of 0.7°, Root Mean Square (RMS) surface roughness ~ 8 nm, fringe visibility ~ 0.7 and reflectivity ~ 97 % in wavelength range of 2-20 μm with reference to aluminum standard mirror. Rh thin films deposited under optimum parameters showed prominent XRD peak of Rh(111) plane with FWHM of 0.6°, reflectivity ~ 98 % in wavelength range of 2-20 μm and that of ~ 89-99 % in wavelength range of 300-800 nm with reference to aluminum standard mirror. Mo thin films was very unstable as it got contaminated with oxygen within few weeks after fabrication whereas it was observed that the W and Rh thin film did not show any signature of eruption of the film from the substrate even after couple of months. Therefore, mirror-like thin films of W and Rh were subjected ion beam irradiation in order to test their sustainability for fusion device.

The PLD mirror-like W thin films exposed to 8 keV H ion beam having ion flux ~ 8.9×10^{14} ions/cm^2/s for 30 minute duration, showed only ~ 2 % degradation in FIR reflectivity. W thin films were also exposed to 10-30 keV D ion beam having ion

flux ~ 1.2×10^{14} ions/cm^2/s for 10 minute duration. The percentage wise reduction in reflectivity of mirror-like W thin films in the FIR range of 2-20 μm, was ~ 6-9 % for 10 keV, 1-4 % for 20 keV and 1-3 % for 30 keV D ion beam irradiation. In the UV-visible range of 300-800 nm, the reduction in reflectivity was ~ 28-38 % for 10 keV, ~ 29 % for both 20 and 30 keV D ion beam irradiation. The reduction in optical reflectivity due to D ion beam irradiation on W thin films was more compared to that of H ion beam irradiation. In case of Rh thin films, the percentage wise reduction in reflectivity in the FIR range of 2-20 μm, was ~ 5-7 % for 10 keV, 3-6 % for 20 keV and 1-2 % for 30 keV D ion beam irradiation. In the UV-visible range of 300-800 nm, the reduction in reflectivity was ~ 7-32 % for 10 keV, 5-26 % for 20 keV and 5-23 % for 30 keV D ion beam irradiation. The increase in RMS surface roughness of the W and Rh thin films due to ion beam irradiation could be one of the factors for the reduction of optical reflectivity. The second factor contributing towards the lowering of reflectivity could be the lattice irregularities, precipitation and trapping of foreign particles in the host lattice due to ion irradiation within the detecting depth limit of optical photon. The possibility of the formation of deuterium bonding with host lattice atoms, could also be responsible for the changes in post exposure reflectivity. The overall specular reflectivity of W and Rh thin films was above 88 % in FIR range before and after ion beam irradiation. Therefore, W and Rh thin films could be used as FM in FIR range where the ion fluence and energy are comparable to the present case.

The quality and sustainability of W and Rh thin films, in the long term exposure of fusion plasma can be enhanced by making multilayer thin film of more than one element. Based on the damage parameters of D ions and the properties of

Rh, W, Cu and SS, the Rh/W/Cu multilayer thin film was designed and fabricated for FM application. The Rh/W/Cu multilayer thin films were also exposed to 20 keV and 30 keV D ion beams having ion flux ~ 1.2×10^{14} ions/cm^2/s for 10 minute duration. The reflectivity of Rh/W/Cu thin films was reduced by ~ 1-4 % in FIR range of 2-20 μm and that of ~ 3-20 % in UV-visible range of 300-800 nm, respectively. The overall specular reflectivity of Rh/W/Cu thin films was above 90 % in FIR range before and after ion beam irradiation. Therefore, Rh/W/Cu multilayer thin film are better than single layer Rh thin film for FM in FIR range where the ion fluence and energy are comparable to the present case.

In fusion reactor, large amount of radiation from the fusion plasma is required to be collected for better reliability of optical signals. The large area coating using conventional PLD technique is difficult. Therefore, the conventional PLD technique was modified by incorporating a substrate rastering stage in place of a fixed substrate holder. Rh single and Rh/W/Cu multilayer thin films were deposited on highly polished 50 mm diameter SS substrate by modified PLD technique. The thickness of Rh single and Rh/W/Cu multilayer thin films was observed to be ~ 120 nm and ~ 25/180/30 nm, respectively. The deposition rates were ~ 1 nm/minute, 2 nm/minute and 3 nm/minute for Rh, W and Cu, respectively. The uniformity of deposition was confirmed by distinct, straight and parallel interference fringes both for Rh single layer and Rh/W/Cu multilayer thin films.

Future scope of the work

The FMs placed at different locations inside the fusion reactor are exposed to energetic particles having a wide range of energy, from ~ few tens of eV to several

hundreds of keV and particle flux ranging from ~ 10^{14} ions/cm^2/s to 10^{20} ions/cm^2/s. In the present thesis work, mirror-like thin films of W, Rh and Rh/W/Cu fabricated by PLD technique, were exposed to high energy, 8 keV H ions as well as 10-30 keV D ions under lower ion flux ~ 10^{14} ions/cm^2/s. The effect of lower ion energy (few hundreds of eV) and higher ion flux (~ 10^{20} ions/cm^2/s), exposure on the PLD thin films is expected to be different from the present studies. A detailed study on the effect of low energy, H and D ions on the optical reflectivity, can be undertaken as future extension of the preset work.

The quality of the thin film FM via PLD technique depends on the laser induced plasma parameters. In order to understand the thin film growth by PLD, a systematic spectroscopy study on the laser induced plasma of Mo, W and Rh, can be taken as the extension of the present thesis work.

Bibliography

[1] V. Voitsenya, A. E. Costley, V. Bandourko et al., "Diagnostic first mirrors for burning plasma experiments," *Review of Scientific Instruments* **72**, 475-482 (2001).

[2] V. S. Voitsenya, A. F. Bardamid, V. N. Bondarenko et al., "Some problems arising due to plasma-surface interaction for operation of the in-vessel mirrors in a fusion reactor," *Journal of Nuclear Materials* **290-293**, 336-340 (2001).

[3] V. S. Voitsenya, V. G. Konovalov, A. F. Shtan et al., "Some problems of the material choice for the first mirrors of plasma diagnostics in a fusion reactor," *Review of Scientific Instruments* **70**, 790-793 (1999).

[4] D. Orlinski, A. F. Bardamid, V. Konovalov et al., "Rhodium as the promising material for the first mirror of laser and spectroscopy methods of plasma diagnostic in a fusion reactor," *Problems of Atomic Science and Technology* **N 3. Series Plasma Physics**, 67-69 (2000).

[5] A. I. Belyaeva, A. F. Bardamid, J. W. Davis et al., "Hydrogen ion bombardment damage in stainless steel mirrors," *Journal of Nuclear Materials* **345**, 101-108 (2005).

[6] G. De. Temmerman, R. A. Pitts, V. S. Voitsenya et al., "First mirror tests for ITER: Influence of material choice on the erosion/deposition mechanisms affecting optical reflectivity," *Journal of Nuclear Materials* **363-365**, 259-263 (2007).

[7] T. Hernandez, P. Martin, P. Fernandez et al., "Effects of irradiation conditions and environment on the reflectivity of different steel mirrors for ITER diagnostics systems," *Fusion Engineering and Design* **84**, 935-938 (2009).

[8] V. S. Udintsev, "Measurements of temperature and density in magnetic confinement fusion devices," *Nuclear Instruments and Methods in Physics Research A* **623**, 649-652 (2010).

[9] H. Urabe, M. Miyamoto, K. Ono et al., "Degradation of reflectivity in stainless steel mirrors under irradiation with low-energy helium ions," *Journal of Nuclear Materials* **386-388**, 1038-1040 (2009).

[10] M. Rubel, G. D. Temmerman, P. Sundelin et al., "An overview of comprehensive First Mirror Test for ITER at JET," *Journal of Nuclear Materials* **390-391**, 1066-1069 (2009).

[11] E. Franconi, M. Rubel, and B. Emmoth, "Deuterium and impurity distributions on plasma eroded carbon materials for the NET first wall," *Nuclear Fusion* **29**, 787-793 (1989).

[12] J. P. Graves, I. T. Chapman, S. Coda et al., "Control of magnetohydrodynamic stability by phase space engineering of energetic ions in tokamak plasmas," *Nature Communications* **3**, 624 1-8 (2012).

[13] R. Cesario, L. Amicucci, A. Cardinali et al., "Current drive at plasma densities required for thermonuclear reactors," *Nature Communications* **1**, 55 1-8 (2010).

[14] N. Y. Orlov, O. B. Denisov, O. N. Rosmej et al., "Theoretical and experimental studies of material radiative properties and their applications to laser and heavy ion inertial fusion," *Laser and Particle Beams* **29**, 69-80 (2011).

[15] A. A. Ovsyannikov and M. F. Zhukov, "Plasma Diagnostics," *Cambridge International Science Publishing* **ISBN 1 898326231** (2000).

[16] I. H. Hutchinson, "Principles of Plasma Diagnostics " *Cambridge University Press* **Second ISBN-13 978-0-521-80389-2** (2005).

[17] P. S. Jagdish and N. T. Surya, "Laser Induced Breakdown Spectroscopy," *Elsevier* **First** (2007).

[18] D. Wolfgang, "Laser Spectroscopy," *Springer,* Berlin Heidelberg **Fourth** (2008).

[19] R. W. P. McWhirter, "Spectral intensities in Plasma Diagnostic Techniques," (Eds. R. H. Huddlestone and S. L. Leonard) *Academic Press* (1965).

[20] H. R. Griem, "Plasma Spectroscopy," *McGraw-Hill* New York (1964).

[21] H. R. Griem, "Spectral Lines Broadening by Plasmas," *Academic Press* New York (1974).

[22] C. Aragon and J. A. Aguilera, "Characterization of laser induced plasmas by optical emission spectroscopy: A review of experiments and methods," *Spectrochimica Acta Part B* **63**, 893-916 (2008).

[23] Y. F. Lu, Z. B. Tao, and M. H. Hong, "Characteristics of Excimer Laser Induced Plasma from Aluminum Target by Spectroscopic Study," *Japanese Journal of Applied Physics* **38**, 2958-2963 (1999).

[24] A. E. Costley, D. J. Campbell, S. Kasai et al., "ITER R&D: Auxiliary Systems: Plasma Diagnostics," *Fusion Engineering and Design* **55**, 331-346 (2001).

[25] S. Lindig, M. Balden, V. K. Alimov et al., "Sub-surface structures of ITER-grade W (Japan) and re-crystallized W after ITER-similar low-energy and high-flux D plasma loadings " *Physica Scripta* **T145**, 014039 1-7 (2011).

[26] L. Marot, G. De. Temmerman, P. Oelhafen et al., "Rhodium coated mirrors deposited by magnetron sputtering for fusion applications," *Review of Scientific Instruments* **78**, 103507 1-7 (2007).

[27] L. Marot, G. De Temmerman, V. Thommen et al., "Characterization of magnetron sputtered rhodium films for reflective coatings," *Surface and Coatings Technology* **202**, 2837-2843 (2008).

[28] A. Litnovsky, V. Voitsenya, T. Sugie et al., "Progress in research and development of mirrors for ITER diagnostics," *Nuclear Fusion* **49**, 075014 1-8 (2009).

[29] A. Ebihara, M. Tokitani, K. Tokunaga et al., "Irradiation effects of low energy helium ions on optical reflectivity of metallic mirror," *Journal of Nuclear Materials* **363-365**, 1195-1200 (2007).

[30] B. Eren, L. Marot, M. Langer et al., "The effect of low temperature deuterium plasma on molybdenum reflectivity," *Nuclear Fusion* **51**, 103025 1-10 (2011).

[31] M. Lipa, B. Schunke, Ch. Gil et al., "Analyses of metallic first mirror samples after long term plasma exposure in Tore Supra," *Fusion Engineering and Design* **81**, 221-225 (2006).

[32] Y. Zhou, B. Y. Gao, Y. M. Jiao et al., "Study of first mirror exposure and protection in HL-2A tokamak," *Fusion Engineering and Design* **81**, 2823-2826 (2006).

[33] Y. Zhou, L. Zheng, H. Gao et al., "Cleaning of the first mirror and diagnostic windows by laser on HL-2A," *Physica Scripta* **T138**, 014066 1-4 (2009).

[34] S. Brezinsek, P. T. Greenland, Ph Mertens et al., "On the measurement of molecular particle fluxes in fusion boundary plasmas," *Journal of Nuclear Materials* **313-316**, 967-971 (2003).

[35] G. De. Temmerman, J. J. Zielinski, H. van der. Meiden et al., "Production of high transient heat and particle fluxes in a linear plasma device," *Applied Physics Letters* **97**, 081502 1-3 (2010).

[36] B. I. Khripunov, O. K. Chugunov, V. M. Gureev et al., "Effect of radiation damage on material erosion in plasma," *34th EPS Conference on Plasma Phys. Warsaw* **31F**, O-2.003 (2007).

[37] M. Baelmans, P. Borner, W. Dekeyser et al., "Tokamak plasma edge modelling including the main chamber wall," *Nuclear Fusion* **51**, 083023 1-13 (2011).

[38] K. Tobita, S. Nishio, S. Konishi et al., "First wall issues related with energetic particle deposition in a tokamak fusion power reactor," *Fusion Engineering and Design* **65**, 561-568 (2003).

[39] E. Gaio, V. Toigo, A. D. Lorenzi et al., "The alternative design concept for the ion source power supply of the ITER neutral beam injector," *Fusion Engineering and Design* **83**, 21-29 (2008).

[40] Y. Ikeda, N. Umeda, N. Akino et al., "Present status of the negative ion based NBI system for long pulse operation on JT-60U," *Nuclear Fusion* **46**, S211-S219 (2006).

[41] Y. Takeiri, O. Kaneko, K. Tsumori et al., "High-power and long-pulse injection with negative-ion-based neutral beam injectors in the Large Helical Device," *Nuclear Fusion* **46**, S199-S210 (2006).

[42] R. S. Hemsworth, A. Tanga, and V. Antoni, "Status of the ITER neutral beam injection system (invited)," *Review of Scientific Instruments* **79**, 02C109 101-105 (2008).

[43] P. Helander and R. J. Akers, "On neutral-beam injection counter to the plasma current," *Physics of Plasmas* **12**, 112503 1-7 (2005).

[44] H. H. Duong, W. W. Heidbrink, E. J. Strait et al., "Loss of energetic beam ions during TAE instabilities," *Nuclear Fusion* **33**, 749-765 (1993).

[45] N. Oyama, Y. Sakamoto, A. Isayama et al., "Energy loss for grassy ELMs and effects of plasma rotation on the ELM characteristics in JT-60U," *Nuclear Fusion* **45**, 871-881 (2005).

[46] M. Fukumoto, H. Kashiwagi, Y. Ohtsuka et al., "Hydrogen behavior in damaged tungsten by high-energy ion irradiation," *Journal of Nuclear Materials* **386-388**, 768-771 (2009).

[47] D. F. Johnson and E. A. Carter, "Hydrogen in tungsten: Absorption, diffusion, vacancy trapping, and decohesion," *Journal of Materials Research* **25**, 315-327 (2010).

[48] H. Maier, T. Hirai, M. Rubel et al., "Tungsten and beryllium armour development for the JET ITER-like wall project," *Nuclear Fusion* **47**, 222-227 (2007).

[49] W. R. Wampler and R. P. Doerner, "The influence of displacement damage on deuterium retention in tungsten exposed to plasma," *Nuclear Fusion* **49**, 1-9 (2009).

[50] S. Brezinsek, T. Loarer, K. Krieger et al., "Fuel retention in impurity seeded discharges in JET after Be evaporation," *Nuclear Fusion* **51**, 073007 1-9 (2011).

[51] R. S. Averback, R. Benedek, and K. L. Merkle, "Defect production in copper and silver by light energetic ions," *Applied Physics Letters* **30**, 455-457 (1977).

[52] J. N. Brooks and J. P. Allain, "Particle deposition and optical response of ITER motional Stark effect diagnostic first mirrors," *Nuclear Fusion* **48**, 045003 1-9 (2008).

[53] O. V. Ogorodnikova, J. Roth, and M. Mayer, "Ion-driven deuterium retention in tungsten," *Journal of Applied Physics* **103**, 034902 1-10 (2008).

[54] O. V. Ogorodnikova, T. Schwarz-Selinger, K. Sugiyama et al., "Deuterium retention in tungsten exposed to low-energy pure and helium-seeded deuterium plasmas," *Journal of Applied Physics* **109**, 013309 1-10 (2011).

[55] S. Masuzaki, N. Ohno, and S. Takamura, "Experimental study on plasma heat flow to plasma facing materials," *Journal of Nuclear Materials* **223**, 286-293 (1995).

[56] Y. G. Shen, Y. W. Mai, Q. C. Zhang et al., "Residual stress, microstructure, and structure of tungsten thin films deposited by magnetron sputtering," *Journal of Applied Physics* **87**, 177-187 (2000).

[57] R. S. Bhaskar, A. K. Bhalchandra, S. M. Imtiaz et al., "Enhanced field emission from hexagonal rhodium nanostructures," *Applied Physics Letters* **92**, 253106 1-3 (2008).

[58] I. Djerdj, A. M. Tonejc, A. Tonejc et al., "XRD line profile analysis of tungsten thin films," *Vacuum* **80**, 151-158 (2005).

[59] H. Duanwei and S. D. Thomas, "X-ray diffraction study of the static strength of tungsten to 69 GPa," *Physical Review B* **73**, 134106 1-8 (2006).

[60] V. K. Alimov, K. Ertl, J. Roth et al., "Deuterium Retention and Lattice Damage in Tungsten Irradiated with D ions," *Phycia Scripta* **T 94**, 34-42 (2001).

[61] E. Strumberger, "Deposition patterns of fast ions on plasma facing components in W7-X," *Nuclear Fusion* **40**, 1697-1713 (2000).

[62] M. B. Lewis, "A method for simulating fusion reactor radiation damage using triple ion beams," *IEEE Transactions on Nuclear Science* **26**, 1320-1322 (1979).

[63] V. Slugen, J. Kuriplach, P. Ballo et al., "Hydrogen implantation effect in copper alloys selected for ITER investigated by positron annihilation spectroscopy," *Nuclear Fusion* **44**, 93-97 (2004).

[64] A. Manhard, K. Schmid, M. Balden et al., "Influence of the microstructure on the deuterium retention in tungsten," *Journal of Nuclear Materials* **415**, S632-S635 (2011).

[65] A. Manhard, U. V. Toussaint, T. Durbeck et al., "Statistical analysis of blister bursts during temperature-programmed desorption of deuterium-implanted polycrystalline tungsten " *Physica Scripta* **T145**, 014038 1-4. (2011).

[66] V. K. Alimov and J. Roth, "Hydrogen isotope retention in plasma-facing materials: review of recent experimental results," *Physica Scripta* **T128**, 6-13 (2007).

[67] D. Kato, H. Iwakiri, and K. Morishita, "First principle study on binding energy of vacancy hydrogen cluster in tungsten," *Journal of Plasma and Fusion Research Series* **8**, 404-407 (2009).

[68] N. Baluc, K. Abe, J. L. Boutard et al., "Status of R&D activities on materials for fusion power reactors," *Nuclear Fusion* **47**, S696–S717 (2007).

[69] T. Hino, A. Sagara, Y. Nobuta et al., "Material probe analysis for plasma facing surface in the Large Helical Device," *Nuclear Fusion* **44**, 496–502 (2004).

[70] A. T. T. Mostako and A. Khare, "Molybdenum thin films via pulsed laser deposition technique for first mirror application," *Laser and Particle Beams* **30**, 559-567 (2012).

[71] A. T. T. Mostako, A. Khare, C. V. S. Rao et al., "Effect of Hydrogen ion beam irradiation onto the FIR reflectivity of pulsed laser deposited mirror like Tungsten films," *Journal of Nuclear Materials* **423**, 53-60 (2012).

[72] L. Marot, R. Steiner, M. Gantenbein et al., "Co-Deposition of Rhodium and Tungsten Films for the First-Mirror on ITER," *Journal of Nuclear Materials* **415**, S1203-1206 (2011).

[73] M. Passoni, D. Dellasega, G. Grosso et al., "Nanostructured rhodium films produced by pulsed laser deposition for nuclear fusion applications," *Journal of Nuclear Materials* **404**, 1-5 (2010).

[74] E. D. Palik, "Handbook of optical constants of solids," *Academic Press*, San Diego (1985).

[75] K. Kalyanasundaram, "Dye-sensitized solar cells," *EPFL press, Taylor and Francis grou*, France **First** (2010).

[76] H. Sugihara, H. Arakawa, K. Sayama et al., "Metal complex useful as sensitizer, dye-sensitized oxide semiconductor electrode and solar cell using same," *United States Patent* **US 6,278,056 B1** (2001).

[77] L. A. Kosyachenko, "Solar cells Dye-sensitized devices," *InTech press*, Croatia **First** (2011).

[78] B. Munkhbayar, M. J. Nine, J. Jeoun et al., "Synthesis of a graphene-tungsten composite with improved dispersibility of graphene in an ethanol solution and its use as a counter electrode for dye-sensitised solar cells," *Journal of Power Sources* **230**, 207-217 (2013).

[79] H. Y. Kyung, K. K. Seok, R. B. V. Chalapathy et al., "Characterization of a Molybdenum Electrode Deposited by Sputtering and Its Effect on Cu(In,Ga)Se_2 Solar Cells," *Journal of The Korean Physical Society* **45**, 1114-1118 (2004).

[80] S. Kyoseung, S. J. Sung, H. J. Jo et al., "Electrochemical Investigation of High-Performance Dye-Sensitized Solar Cells Based on Molybdenum for Preparation of Counter Electrode," *International Journal of Electrochemical Science* **8**, 8272-8281 (2013).

[81] M. Jubault, L. Ribeaucourt, E. Chassaing et al., "Optimization of molybdenum thin films for electrodeposited CIGS solar cells," *Solar Energy Materials and Solar Cells* **95**, 26-31 (2011).

[82] K. M. Wong, Y. G. Shen, and P. L. Wong, "Tribological properties of

sputtered tungsten and tungsten nitride thin films," *Science in China A* **44**, 242 (2001).

[83] C. W. Lee, Y. T. Kim, and J. Y. Lee, "New method to improve thermal stability in the interface of silicon and tungsten by the interposition of plasma deposited tungsten nitride thin film," *Applied Physics Letters* **64**, 619-621 (1994).

[84] F. D. Fonzo, A. Bailini, V. Russo et al., "Synthesis and characterization of tungsten and tungsten oxide nanostructured films," *Catalysis Today* **116**, 69-73 (2006).

[85] R. A. Ganeev, U. Chakravarty, P. A. Naik et al., "Pulsed laser deposition of metal films and nanoparticles in vacuum using subnanosecond laser pulses," *Applied Optics* **46**, 1205-1210 (2007).

[86] Y. H. Lee, C. H. Choi, Y. T. Jang et al., "Tungsten nanowires and their field electron emission properties," *Applied Physics Letters* **81**, 745-747 (2002).

[87] Y. H. Lee, D. H. Kim, C. H. Choi et al., "Growth and electrical properties of multidimensional tungsten nano-buliding blocks," *Applied Physics Letters* **85**, 5977-5979 (2004).

[88] S. Herd, K. N. Tu, and K. Y. Ahn, "Formation of an amorphous Rh-Si alloy by interfacial reaction between amorphous Si and crystalline Rh thin films," *Applied Physics Letters* **42**, 597-599 (1983).

[89] H. Khatri and S. Marsillac, "The effect of deposition parameters on radiofrequency sputtered molybdenum thin films," *Journal of Physics: Condensed Matter* **20**, 055206 1-5 (2008).

[90] C. R. Tomachuk, L. D. Rosa, J. Springer et al., "The Wet film-Part II: Behavior at 85 ^{0}C thin corrosion of molybdenum," *Materials and corrosion* **55**, 665-670 (2004).

[91] Koichi Okamoto, Zhaoyu Zhang, David T. Wei et al., "Photothermal molecular sensing by using metal thin-film nanograting for chemical and biomedical applications," *Thin Solid Films* **469-470**, 420-424 (2004).

[92] P. Kuban, J. M. Berg, and P. K. Dasgupta, "Durable Microfabricated High-Speed Humidity Sensors," *Analytical Chemistry* **76**, 2561-2567 (2004).

[93] G. U. Kulkarni and B. Radha, "Metal nanowire grating patterns," *Nanoscale* **2**, 2035-2044 (2004).

[94] M. S. Aouadi, R. R. Parsons, P. C. Wong et al., "Characterization of sputter deposited tungsten films for x-ray multilayers," *Journal of Vacuum Science Technology* **10**, 273-280 (1992).

[95] I. A. Weerasekera, S. Ismat Shah, David V. Baxter et al., "Structure and stability of sputter deposited beta-tungsten thin films," *Applied Physics Letters* **64**, 3231-3233 (1994).

[96] J. Ligot, S. Benayoun, J. J. Hantzpergue et al., "Sputtered tungsten films on polyimide, an application for X-ray masks," *Solid-State Electronics* **43**, 1075-1078 (1999).

[97] G. K. Celler, L. E. Trimble, J. Frackoviak et al., "Formation of monolithic masks for 0.25 μm x-ray lithography," *Applied Physics Letters* **59**, 3105-3107 (1991).

[98] R. E. Felix-Medina, M. A. Leyva-Lucero, and S. Meza-Aguilar, "Magnetism of Ru and Rh thin films on Ag(001) substrate: ab initio calculations," *European Physical Journal B* **69**, 195-201 (2009).

[99] K. Tomoya, K. Hideaki, N. Hiroshi et al., "Transport properties via surface localized states of Ru, Rh and Pd thin films on Ag(111)," *Solid State Communications* **135**, 698-702 (2005).

[100] A. B. Hayden, T. Valla, and D. P. Woodruff, "Inverse photoemission and Auger electron spectroscopy of Rh thin films on Cu(100)," *Journal of Physics: Condensed Matter* **7**, 9475-9484 (1995).

[101] A. Stolovits, A. Sherman, and T. Avarmaa, "Magnetoresistance study of a thin α-tungsten film," *Physical Review B* **58**, 11 111 -114 (1998).

[102] F. Saidani, D. Rochefort, and M. Mohamedi, "Synthesis, Characterization of Nanostructured Rhodium Films and their Electrochemical Behavior towards Carbon Monoxide Oxidation," *Electrocatal* **2**, 114-122 (2011).

[103] P. Jung-Chul, "Purification and Recovery of Rhodium Metal by the Formation of Intermetallic Compounds," *Bulletin of Korean Chemical Society* **29**, 1787-1789 (2008).

[104] K. Masek, V. Matolin, and M. Gillet, "Study of the growth of rhodium particles on different substrates," *Thin Solid Films* **260**, 252-258 (1995).

[105] R. Dus, E. Nowicka, and R. Nowakowski, "Hydrogen adsorption on rhodium: Hydride formed on the surface of thin rhodium films," *Applied Surface*

Science **254**, 4286-4291 (2008).

[106] S. Stempel, M. Baumer, and H. J. Freund, "STM studies of rhodium deposits on an ordered alumina film-resolution and tip effects," *Surface Science* **402-404**, 424-427 (1998).

[107] L. Stefan, T. Edmund, and K. Helmut, "Metal-support interactions on rhodium model catalysts," *Topics in Catalysis* **14**, 153-161 (2001).

[108] S. K. Samanta, W. Jong Yoo, G. Samudra et al., "Tungsten nanocrystals embedded in high-k materials for memory application," *Applied Physics Letters* **87**, 113110 1-3 (2005).

[109] S. Basavaiah and S. R. Pollack, "Superconductivity in evaporated tungsten films," *Applied Physics Letters* **12**, 259-260 (1968).

[110] J. H. Souk, J. F. Ohanlon, and J. Angillelo, "Characterization of electron-beam deposited tungsten films on sapphire and silicon," *Journal of Vacuum Science and Technology* **A 3**, 2289-2292 (1985).

[111] S. Krishna, "Handbook of thin-film deposition processes and techniques," *William Andrew Publishing* Norwich, New York (2002).

[112] J. E. Mahan, "Physical vapour deposition of thin films," *Wiley VCH* USA (2000).

[113] P. Collot, B. Agius, P. Estrache et al., "Physicochemical properties in tungsten films deposied by radio-frequency magnetron sputtering," *Journal of Vacuum Science Technology* **A 6**, 2319-2325 (1988).

[114] V. G. Glebovsky and E. A. Markaryans, "Thin film metallization by magnetron sputtering from highly pure molybdenum targets," *Journal of Alloys and Compounds* **190**, 157-160 (1993).

[115] M. Itoh, M. Hori, and S. Nadahara, "The origin of stress in sputter-deposited tungsten films for x-ray masks," *Journal of Vacuum Science Technology* **B 9**, 149-153 (1991).

[116] L. Zhu, L. Guo-lu, H. Wang et al., "Microstructures and nano mechanical properties of the metal tungsten film," *Current Applied Physics* **9**, 510-514 (2009).

[117] A. Bensaoula, J. C. Wolfe, A. Ignatiev et al., "Direct-current-magnetron deposition of molybdenum and tungsten with rf-substrate bias," *Journal of Vacuum Science Technology* **A 2**, 389-392 (1984).

[118] T. Hirata and K. Saito, "The reflectance of sputtered molybdenum thin films implanted with nitrogen ions," *Journal of Materials Science Letters* **9**, 827-828 (1990).

[119] J. L. Vossen and W. Kern, "Thin film processes," *Academic Press*, New York **2** (1991).

[120] J. R. V. Garcia and T. Goto, "Chemical Vapor Deposition of Iridium, Platinum, Rhodium and Palladium," *Materials Transactions* **44** (9), 1717-1728 (2003).

[121] K. A. Gesheva, T. A. Krisov, U. I. Simkov et al., "Deposition and study of CVD-tungsten and molybdenum thin films and their impact on microelectronics technology," *Applied Surface Science* **73**, 86-89 (1993).

[122] A. Rozenblat, S. Haimson, Y. Shacham-Diamand et al., "The relationship between structural evolution and electrical percolation of the initial stages of tungsten chemical vapor deposition on polycrystalline TiN," *Applied Physics Letters* **100**, 031907 1-4 (2012).

[123] T. F. Deutsch and D. D. Rathman, "Comparison of laser-initiated and thermal chemical vapor deposition of tungsten films," *Applied Physics Letters* **45**, 623-625 (1984).

[124] Y. T. Kim, S. K. Min, J. S. Hong et al., "Plasma-enhanced chemical vapor deposition of low-resistive tungsten thin films," *Applied Physics Letters* **58**, 837-839 (1991).

[125] S. L. Booyong, A. Rahtu, and R. G. Gordon, "Atomic layer deposition of transition metals," *Nature Materials* **2**, 749-754 (2003).

[126] E. Snoeks, K. S. Boutros, and J. Barone, "Stress relaxation in tungsten films by ion irradiation," *Applied Physics Letters* **71**, 267-269 (1997).

[127] M. Juppo, M. Vehkamaki, M. Ritala et al., "Deposition of molybdenum thin films by an alternate supply of $MoCl_5$ and Zn," *Journal of Vacuum Science and Technology* **A 16**, 2845-2850 (1998).

[128] N. Bidin, R. Qindeel, M. Y. Daud et al., "Plasma Splashing from Al and Cu Materials Induced by an Nd:YAG Pulsed Laser," *Laser Physics* **17**, 1222-1228 (2007).

[129] A. M. Dhote and S. B. Ogale, "Deposition of tungsten films by pulsed excimer laser ablation technique," *Applied Physics Letters* **64**, 2809-2811 (1994).

[130] B. L. Drogoff, M. A. E. Khakani, P. R. M. Silva et al., "Surface properties of pulsed laser deposited Ir, Rh, and $Ir_{0.9}Rh_{0.1}$ thin films for use as microelectrode arrays in electroanalytical heavy metal trace sensors," *Applied Surface Science* **152**, 77-84 (1999).

[131] R. K. Singh and J. Narayan, "Pulsed-laser evaporation technique for deposition of thin films: Physics and theoretical model," *Physical Review B* **41**, 8843-8859 (1990).

[132] O. Fruchart, S. Jaren, and J. Rothman, "Growth modes of W and Mo thin epitaxial (110) films on (1120) sapphire," *Applied Surface Science* **135**, 218-232 (1998).

[133] F. C. F. Robin, "Molecular beam epitaxy application to key materials," *Noyes Publications* USA (1995).

[134] E. H. C. Parker, "The Technology and physics of molecular beam epitaxy," *Plenum Press* New York (1985).

[135] W. Kiyotaka, "Handbook of sputter deposition technique: Fundamentals and applications," *William Andrew Waltham*, USA **Second** (2012).

[136] M. Ohring, "Materials science of thin films: Deposition and structure," *Academic Press*, San Diego USA **Second** (2006).

[137] R. Eason, "Pulsed laser deposition of thin films applications-led growth of functional materials," *Wiley-Interscience John Wiley and sons*, New Jersey (2007).

[138] D. B. Chrisey and G. K. Hubler, "Pulsed Laser Deposition of Thin Films," *John Wiley and Sons*, New York (1994).

[139] M. N. R. Ashfold, F. Claeyssens, G. M. Fuge et al., "Pulsed laser ablation and deposition of thin films," *Chemical Society Review* **33**, 23-31 (2004).

[140] J. G. Lunney, "Pulsed laser deposition of metal and metal multilayer films," *Applied Surface Science* **86**, 79-85 (1995).

[141] P. R. Willmott and J. R. Huber, "Pulsed laser vaporization and deposition," *Reviews of Modern Physics* **72**, 315-328 (2000).

[142] D. H. Lowndes, D. B. Geohegan, A. A. Puretzky et al., "Synthesis of Novel Thin-Film Materials by Pulsed Laser Deposition," *Science* **273**, 898-903 (1996).

[143] P. Mukherjee, S. Chen, and S. Witanachchi, "Effect of initial plasma geometry and temperature on dynamic plume expansion in dual-laser ablation," *Applied Physics Letters* **74**, 1546-1548 (1999).

[144] A. T. T. Mostako and A. Khare, "Effect of target-substrate distance onto the nanostructured rhodium thin films via PLD technique," *Applied Nanoscience* **2** 189-193 (2012).

[145] A. T. T. Mostako, C. V. S. Rao, and A. Khare, "Mirrorlike pulsed laser deposited tungsten thin film," *Review of Scientific Instruments* **82**, 013101 1-6 (2011).

[146] H. M. Smith and A. F. Turner, "Vacuum Deposited Thin Films Using a Ruby Laser," *Applied Optics* **4**, 147-148 (1965).

[147] R. W. Dreyfus, "Cu^0, Cu^+, and Cu_2 from excimer-ablated copper," *Journal of Applied Physics* **69**, 1721-1729 (1991).

[148] J. J. Yoh, H. Lee, J. Choi et al., "Ablation-induced explosion of metal using a high power Nd:YAG laser," *Journal of Applied Physics* **103**, 043511 1-6 (2008).

[149] Y. Kawakami and E. Ozawa, "Tungsten microcone growth by laser irradiation," *Applied Surface Science* **218**, 175-187 (2003).

[150] J. Cheung and J. Horwitz, "Pulsed laser deposition history and laser-target interactions," *MRS Bulletin* **17**, 30-36 (1992).

[151] J. Narayan, N. Biunno, R. Singh et al., "Formation of thin superconducting films by the laser processing method," *Applied Physics Letters* **51**, 1845-1847 (1987).

[152] R. E. Russo, "Laser ablation," *Applied Spectroscopy* **49**, 14A-28A (1995).

[153] B. N. Chichkov, C. Momma, S. Nolte et al., "Femtosecond, picosecond and nanosecond laser ablation of solids," *Applied Physics A* **63**, 109-115 (1996).

[154] Y. F. Lu, M. H. Hong, and T. S. Low, "Laser plasma interaction at an early stage of laser ablation," *Journal of Applied Physics* **85**, 2899-2903 (1999).

[155] S. S. Mao, X. Mao, R. Greif et al., "Initiation of early-stage plasma during picosecond laser ablation of solids," *Applied Physics Letters* **77**, 2464-2466 (2000).

[156] W. Demtroder and W. Jantz, "Investigation of laser-produced plasmas from

metal-surfaces," *Plasma Physics* **12**, 691-703 (1970).

157 A. B. Brailovsky, S. V. Gaponov, and V. I. Luchin, "Mechanisms of melt droplets and solid-particle ejection from a target surface by pulsed laser action," *Applied Physics A* **61**, 81-86 (1995).

158 E. G. Gamaly, A. V. Rode, and B. Luther-Davies, "Laser ablation of carbon at the threshold of plasma formation," *Applied Physics A* **69**, S121-S127 (1999).

159 L. Wiedeman and H. Helvajian, "Laser photodecomposition of sintered $YBa_2Cu_3O_{6+x}$: Ejected species population distributions and initial kinetic energies for the laser ablation wavelengths 351, 248, and 193 nm," *Journal of Applied Physics* **70**, 4513-4523 (1991).

160 S. Metev and K. Meteva, "Nucleation and growth of laser-plasma deposited thin films," *Applied Surface Science* **43**, 402-408 (1989).

161 J. A. Venables, G. D. T. Spiller, and M. Hanbucken, "Nucleation and growth of thin films," *Reports on Progress in Physics* **47**, 399-459 (1984).

162 M. Hernandez, A. Juarez, and R. Hernández, "Interferometric thickness determination of thin metallic films," *Superfiecies y Vacio* **9**, 283-285 (1999).

163 B. D. Culity, "Elements of X-Ray Diffraction (Morris Cohen) " *Massachusetts: Addison-Wesley Metallurgy series* USA (1956).

164 H. E. Bennett and J. O. Porteus, "Relation Between Surface Roughness and Specular Reflectance at Normal Incidence," *Journal of The Optical Society of America* **51**, 123-129 (1961).

165 H. E. Bennett, "Specular Reflectance of Aluminized Ground Glass and the Height Distribution of Surface Irregularities," *Journal of The Optical Society of America* **53**, 1389-1394 (1963).

166 A. M. Hofer, J. Schlacher, J. Keckes et al., "Sputtered molybdenum films: Structure and property evolution with film thickness," *Vacuum* **99**, 149-152 (2013).

167 D. Errandonea, D. Santamaria-Perez, V. Grover et al., "High-pressure x-ray diffraction study of bulk and nanocrystalline $PbMoO_4$," *Journal of Applied Physics* **108**, 073518 1-5 (2010).

168 E. Delabie, R. J. E. Jaspers, M. G. V. Hellermann et al., "Charge exchange spectroscopy as a fast ion diagnostic on TEXTOR," *Review of Scientific Instruments* **79**, 10E522 1-4 (2008).

[169] G. N. Luo, K. Umstadter, W. M. Shu et al., "Behavior of tungsten with exposure to deuterium plasmas," *Nuclear Instruments and Methods in Physics Research B* **267**, 3041-3045 (2009).

[170] A. A. Haasz, M. Poon, and J. W. Davis, "The effect of ion damage on deuterium trapping in tungsten," *Journal of Nuclear Materials* **266-269**, 520-525 (1999).

[171] W. Wang, J. Roth, S. Lindig et al., "Blister formation of tungsten due to ion bombardment," *Journal of Nuclear Materials* **299**, 124-131 (2001).

[172] B. Eren, M. Wisse, L. Marot et al., "Deuterium plasma exposure on rhodium: Reflectivity monitoring and evidence of subsurface deuteride formation," *Applied Surface Science* **273**, 94-100 (2013).

[173] K. E. Peiponen and T. Tsuboi, "Metal surface roughness and optical reflectance," *Optics and Laser Technology* **22**, 127-130 (1990).

[174] G. Lerondel and R. Romestain, "Fresnel coefficients of a rough interface," *Applied Physics Letters* **74**, 2740-2742 (1999).

[175] G. Hass, "Reflectance and preparation of front-surface mirrors for use at various angles of incidence from the ultraviolet to the far infrared," *Journal of optical socity of America* **72**, 27-39 (1982).

[176] M. Mizuguchi, S. Sekiya, and K. Takanashi, "Characterization of Cu buffer layers for growth of $L1_0$-FeNi thin films," *Journal of Applied Physics* **107**, 09A716 1-3 (2010).

[177] L. Xiang, "Thermal conductivity modeling of copper and tungsten damascene structures," *Journal of Applied Physics* **105**, 094301 1-12 (2009).

[178] B. Girault, D. Eyidi, T. Chauveau et al., "Copper coverage effect on tungsten crystallites texture development in W/Cu nonocomposite thin films," *Journal of Applied Physics* **109**, 014305 1-12 (2011).

[179] P. Quintana, A. I. Oliva, O. Ceh et al., "Thickness effects on aluminum thin films," *Superfiecies y Vacio* **9**, 280-282 (1999).

[180] V. V. Jain, "Microstructure and properties of copper thin films on silicon substrates," *A Thesis in partial fulfillment of the requirements for the degree of master of science, Graduate Studies of Texas A and M University*, 48 (2007).

[181] G. V. Samsonov, "Handbook of the physicochemical properties of the elements," *IFI-Plenum*, New York, USA (1968).

LIST OF PUBLICATIONS

(a) Journals

1. 'Molybdenum thin films via pulsed laser deposition technique for first mirror application', **A T T Mostako** and Alika Khare, Laser Part. Beams **30** (2012) 559-567.

2. 'Effect of target-substrate distance onto the nanostructured rhodium thin films via PLD technique', **A T T Mostako** and Alika Khare, Appl. Nanos. **2** (2012) 189-193.

3. 'Effect of Hydrogen ion beam irradiation onto the FIR reflectivity of pulsed laser deposited mirror like Tungsten films', **A T T Mostako**, Alika Khare, C V S Rao, Prakash M Raole, SudhirsinhVala, Shrichand Jakhar, T K Basu, Mitul Abhangi, Rajinikant J Makwana, J. Nucl. Mat. **423** (2012) 53-60.

4. 'Mirrorlike pulsed laser deposited tungsten thin film', **A T T Mostako**, C V S Rao and Alika Khare, Rev. Sci. Instrum. **82** (2011), 013101 1-6.

5. 'Pulsed laser deposition of thin film of molybdenum', **A T T Mostako**, C V S Rao and Alika Khare, Journal of Physics: Conference Series **208** (2010), 012114 1-6.

6. 'Deuterium ion beam irradiation onto the Pulsed Laser deposited Tungsten thin films', **A T T Mostako**, Alika Khare, C V S Rao, Sudhirsinh Vala, R J Makwana and T K Basu, J. Vac. Sci. Technol. A **31** (2013) 0615120 1-7.

7. 'Post irradiation effect of Deuterium ion beam onto Rh/W/Cu multilayer first mirror' **A T T Mostako**, Alika Khare, C V S Rao, Sudhirsinh Vala, R J Makwana and T K Basu, (Accepted in J. Nucl. Mat. (2013)).

8. 'Effect of deuterium ion beam irradiation onto mirror-like Rhodium thin films via pulsed laser deposition', **A T T Mostako**, Alika Khare, C V S Rao, Sudhirsinh Vala, R J Makwana and T K Basu, (manuscript under review).

9. 'Design and fabrication of Rh/W/Cu multilayer thin films for first mirror application' **A T T Mostako** and Alika Khare, (submitted).

10. 'Large area deposition of Rh single and Rh/W/Cu multilayer thin films on stainless steel substrate by pulsed laser deposition technique', **A T T Mostako** and Alika Khare, (submitted).

(b) Conference presentations

1. 'Effect of 30 keV Deuterium Ion Beam onto Pulsed Laser Deposited Rh/W/Cu Multilayer', **A T T Mostako**, Alika Khare, C V S Rao, Sudhirsinh Vala, R J Makwana and T K Basu, poster, 10^{th}-13^{rd} December 2012, Plasma 2012, organized by Pondicherry University and PSSI, India.

2. 'Architecture of Rh/W/Cu Multilayered First Mirror via PLD', **A T T Mostako**, and Alika Khare, poster, 20^{th}-23^{rd} December 2011, Plasma 2011, organized by BIT Patna and PSSI, India.

3. 'Effect of target substrate distance onto the nano scale thickness of rhodium thin films via PLD', **A T T Mostako**, Alika Khare and C V S Rao, poster, 8^{th}-10^{th} December 2011, ICANN-2011, organized by Department of Physics and Center for Nanotechnolgy, IIT Guwahati, Inadia.

4. 'Rh/W/Cu multilayer thin films via PLD', **A T T Mostako**, and Alika Khare, poster, 9^{th}-11^{th} November 2011, PLD-11, organized by Raja Ramanna Center for Advanced Technology, Indore and Indian Institute of Science, Bangaluru, India.

5. 'Pulsed Laser Deposition of Molybdenum thin films', **A T T Mostako**, and Alika Khare, poster, 9^{th}-11^{th} November 2011, PLD-11, organized by Raja Ramanna Center for Advanced Technology, Indore and Indian Institute of Science, Bangaluru, India.

6. 'Effect of Helium gas pressure during deposition on the Specular reflectivity of Rhodium thin films via PLD', **A T T Mostako**, Alika Khare and C V S Rao, poster, 24^{th}-26^{th} 2011, CMAYDS-11, organized by Gauhati University, India.

7. 'Molybdenum Oxides thin films via PLD', **A T T Mostako,** Partha Dey, Himanshu S Jha, Mukesh Singh, Pratima Agarwal and A Khare, poster, 8^{th}-11^{th} December 2010, Plasma 2010, organized by IASST Guwahati and PSSI, India.

8. 'Effect of ion beam irradiation on PLD deposited tungsten films', **A T T Mostako**, Mitul Abhangi, Rajinikant Parmar, Sudhirsinh Vala, Shrichand Jakhar, C V S Rao, T K Basu, and A Khare, poster, 8^{th}-11^{th} December 2010, Plasma 2010, organized by IASST Guwahati and PSSI, India.

9. Pulsed Laser Deposition of Mirror-like Tungsten Thin Films' **A T T Mostako**, C V S Rao and Alika Khare, poster, 8^{th}-11^{th} December 2009, Plasma 2009, organized by NIT Hamirpur (HP) and PSSI, India.

10. **'**Effect of pressure on PLD thin films of Tungsten' **A T T Mostako**, Hitesh Rahandhale and Alika Khare, poster, 23rd-24th May 2009, RACMP 09, organized by NIT Hamirpur, India.

11. 'Pulsed Laser Deposition of thin films of Molybdenum' **A T T Mostako**, C V S Rao and Alika Khare, poster, 10th-13th December 2008, Plasma 2008, organized by BARC and PSSI, India.

(c) Workshops/School attended

1. Participated in IEEE Workshop on Compressed Sensing & Technical Writing during 6th to 7th April 2013, organized by Department of Electronics and Electrical Engineering, IIT Guwahati, India.

2. SERC School on Laser and technology, 12th to 30th March 2012, organized by RRCAT Indore.

3. Participated in Quality Improvement Programme (QIP) short term course during 1st to 6th August 2011, organized by Department of Physics, IIT Guwahati, India.